

# A ROTATING OPTICAL LATTICE FOR ULTRACOLD ATOMS

---

**Ben Fletcher**

A thesis submitted in partial fulfilment of  
the requirements for the degree of  
Doctor of Philosophy at the University of Oxford



St. John's College  
University of Oxford  
Trinity Term 2008

# ABSTRACT

---

## A rotating optical lattice for ultracold atoms

**Ben Fletcher, St. John's College, Oxford University**  
DPhil Thesis, Trinity Term 2008

The central part of this thesis describes the key components, implementation, initial testing and calibration of a two-dimensional, rotating lattice for experiments involving Bose-Einstein condensates of  $^{87}\text{Rb}$ . Additionally, this thesis provides a brief overview of the theory and achievement of Bose-Einstein condensation in our particular set of apparatus and a brief review of the physics underlying optical lattice potentials.

In the work described in this thesis a two-dimensional acousto-optical deflector (AOD) and a series of optics is used to generate a set of 4 beams marking the vertices of a square in the plane perpendicular to the direction of propagation of the beams. The beams are directed through a high numerical aperture lens: the four beams intersect and form a lattice potential in the focal plane of the lens.

This thesis further describes the development of a direct digital synthesis (DDS) based system for generating and ramping radio-frequency (RF) signals which attains noise suppression of greater than 50 dB. The software which allows the frequency and amplitude of a signal generated by the DDS system to be updated at rates up to 1.5 MHz is also described. These low-noise, rapidly-updated RF signals are used as the input to the AOD and are a crucial component of achieving a rotating lattice.

For some of the data discussed in this thesis, it was necessary to image through the aperture of the pyramid MOT to assist with alignment and image atoms held in the optical lattice. Atoms in optical lattices with periodicities ranging from 10 to 30 microns are imaged and this data is used to calibrate the lattice period against the input RF frequency.

Finally we have demonstrated a rapid expansion in the radial size of the condensate when exposed to a rotating lattice which depends on the frequency of the lattice rotation. We hope that this will provide the foundation for work on direct simulation of condensed matter systems using cold atoms.

# ACKNOWLEDGEMENTS

---

Over four years of research, there have been many occasions when I've been stuck on a technical problem, short of ideas or just discouraged. Before digging into the thesis itself, I'd just like to take this opportunity to say 'thank you' to everyone who's helped me out throughout: I've mentioned some of you specifically below, but by no means all!

My thanks first of all to my supervisor, Chris Foot, for giving me the opportunity to work in this field and for all of his help over the years – not least for his comments on drafts of this thesis! I'd also like to thank Ross Williams for his comments on the thesis and for the ideas, rigour and dynamism he's brought to the experiment in the last two years. Similarly I owe a huge debt to the remainder of my coworkers in -111: Andrian, Sarah, Jean-Damien, Martin and Peter; and to the rest of the group: Rachel, Eileen, Will, Amita, Herbert, Giuseppe, Marcin, the other Bens and Markus. Through discussions, cooperation and friendship you've each added something unique to my time in Oxford - thank you!

Graduate students can be famously deaf to the appeals of common sense, and I am no exception at times! It's lucky for us that the Clarendon employs such fantastic staff to keep our feet on the ground. I'll never forget Graham single-handedly moving an optical table, nor the calm with which Rob manages the Research Workshop nor the patience with which Terry and John have dealt with my computer problems and requests over the years. Thank you all!

During my research there were definitely times when I just needed to get away from physics – in those times, it was fantastic to take refuge in the company of friends from St. John's: games night at Andy's or over tea with the MCR. Aaron, Christophe, Dave, Jenny, Josh, Liam, Mark, Mike, Neli, Piers, Refqa, Tim, Tom and Victoria - I owe you all a drink and more!

Last on this list but first in my thoughts, I'd like to thank my parents and my wife for their love, help and support. I owe you more than I can ever say: please take this 'thank you' as a small advance towards my huge debt of gratitude.

# CONTENTS

---

<b>1</b>	<b>Introduction</b>	<b>1</b>
1.1	Motivation . . . . .	1
1.1.1	Quantum Computation . . . . .	2
1.1.2	Accordion Lattices . . . . .	3
1.1.3	Simulating Condensed Matter Systems . . . . .	4
1.2	Experimental Concept . . . . .	6
1.2.1	Original Concept . . . . .	6
1.2.2	Revised Concept . . . . .	10
<b>2</b>	<b>Bose-Einstein Condensation: Theoretical Overview</b>	<b>11</b>
2.1	The Basics . . . . .	11
2.1.1	The Bose distribution for material particles . . . . .	12
2.1.2	Bose-Einstein Condensation . . . . .	13
2.2	The Statistical Mechanics of BEC . . . . .	13
2.2.1	Density of States in a Harmonic Potential . . . . .	14
2.2.2	The transition to BEC . . . . .	15
2.3	Quantum Mechanics of BEC . . . . .	17
2.3.1	The Gross-Pitaevskii Equation . . . . .	17
<b>3</b>	<b>Bose-Einstein Condensation in Practice</b>	<b>21</b>
3.1	Alkali Gases . . . . .	22
3.1.1	Rubidium-87 . . . . .	23
3.2	Lasers . . . . .	24
3.3	Magneto-Optical Traps . . . . .	26
3.4	Compressed MOT, Molasses and Optical Pumping . . . . .	28
3.5	Magnetic Trapping . . . . .	29
3.6	Evaporative Cooling . . . . .	34
3.7	Imaging . . . . .	36
3.7.1	Absorption imaging . . . . .	36
3.7.2	Fluorescence imaging . . . . .	39
3.8	Bose-Einstein Condensation . . . . .	39
3.9	Seeing things in a new light: Axial Absorption Imaging . . . . .	43
3.9.1	Mechanical implementation . . . . .	43

3.9.2	Axial beam profile . . . . .	45
3.9.3	Axial Absorption Magnification . . . . .	47
3.9.4	Remaining Issues . . . . .	49
<b>4</b>	<b>Dipole Trapping and Optical Lattices</b>	<b>51</b>
4.1	The Dipole Potential . . . . .	52
4.1.1	Classical Picture . . . . .	53
4.1.2	Quantum Derivation . . . . .	54
4.1.3	Choosing trap detuning . . . . .	57
4.1.4	Focussed Beam as a Dipole Trap . . . . .	58
4.2	Optical Lattices . . . . .	60
4.3	BEC in an optical lattice . . . . .	60
<b>5</b>	<b>Direct Digital Synthesis for High Precision Frequency Synthesis</b>	<b>64</b>
5.1	Experimental Requirements . . . . .	64
5.2	High Precision Frequency Synthesis . . . . .	66
5.3	Direct Digital Synthesis: an overview . . . . .	68
5.4	DDS Implementation . . . . .	71
5.4.1	Amplification . . . . .	73
5.5	DDS Input/Output and PC Control . . . . .	75
5.5.1	Software Control . . . . .	77
<b>6</b>	<b>A dynamically flexible lattice via acousto-optical deflection</b>	<b>81</b>
6.1	Lasers and Intensity Servo . . . . .	81
6.1.1	Lasers . . . . .	82
6.1.2	Intensity Servo . . . . .	84
6.2	Acousto-Optics . . . . .	86
6.2.1	Acousto-Optical Deflection . . . . .	87
6.2.2	Beam steering . . . . .	88
6.2.3	Details of Implementation . . . . .	91
6.2.4	Amplitude Normalization . . . . .	91
6.3	Optical Setup . . . . .	93
6.3.1	Initial Optics . . . . .	94
6.3.2	Scheme in Principle . . . . .	94
6.3.3	Experimental Implementation . . . . .	96
6.3.4	Polarization and the rotating lattice . . . . .	99
6.3.5	Aligning the lattice optics . . . . .	101
6.3.6	Aligning the beam on to the atoms . . . . .	102
6.3.7	The Four Lens Objective . . . . .	103
<b>7</b>	<b>Experimental Results</b>	<b>108</b>
7.1	Calibrating the Lattice Spacing . . . . .	108
7.1.1	Theoretical calibration . . . . .	109
7.1.2	Diffraction from a static lattice . . . . .	110
7.1.3	Imaging Atoms in the Lattice . . . . .	116

7.1.4	Calibrating the Lattice Spacing . . . . .	120
7.1.5	Measuring Beam Separation before the 4-lens Objective . . .	120
7.2	Implementing Rotation . . . . .	125
7.2.1	Lattices at arbitrary angles . . . . .	127
7.2.2	Change in aspect ratio with rotation . . . . .	127
7.2.3	Calculating the Heating Rate due to Rotation . . . . .	133
<b>8</b>	<b>Conclusions</b>	<b>137</b>
8.1	Progress So Far . . . . .	137
8.2	Comparison to Other Work . . . . .	139
8.3	Future Steps . . . . .	141

## CHAPTER 1

---

# Introduction

In recent years there has been a wide range of exciting work around the field of Bose-Einstein condensates in optical lattices and optical potentials, including the work of Greiner *et al.* (2002) achieving the Mott insulator regime, the first steps taken towards a quantum register for neutral atoms by Schrader *et al.* (2004) and the demonstration of rapid manipulation of the single-atom qubits by Yavuz *et al.* (2006).

In this chapter I will describe the general area we seek to explore with our experiment, and explain why it interests us. I will then provide a more specific introduction to the original concept for the experiment and to the revised concept whose implementation is described in the following chapters.

### 1.1 Motivation

Much of the work referred to above has been related to the goal of implementing quantum information processing (QIP) in cold neutral atoms. In this section I will briefly describe the significance and current state of the art in the two major

sub-areas of QIP for which cold atoms are particularly well suited and then outline the current experimental limits.

### 1.1.1 Quantum Computation

Quantum computation - replacing binary, deterministic bits with superposable qubits and probabilistic measurements - offers potential breakthroughs in the fields of cryptography, simulation of quantum systems and handling large databases. (Shor, 1994; Grover, 1996) Proposed methods of implementing quantum computation have included cold atoms, trapped ions, solid state devices and even cluster states of multiple quantum particles. Thus far, nuclear magnetic resonance has realised the largest number of qubits but faces considerable difficulties in any attempt to reach large numbers of qubits (Vandersypen *et al.*, 2001). Ion traps have made rapid progress (Moehring *et al.*, 2007): although scaling to large numbers of ions in the same trap is problematic because of the long-range nature of the Coulomb force, schemes have been developed for handling multiple qubits in which ions only encounter one another in pairs.

Cold atoms seem an ideal implementation to produce computers with large numbers of qubits: experimentalists routinely obtain  $10^9$  cold atoms from laser cooling and trapping techniques and by using evaporative cooling to create a Bose-Einstein condensate (BEC) more than  $10^6$  phase coherent atoms can be obtained. Greiner *et al.* (2002) demonstrated a controlled transition from a BEC into a Mott insulator state in an optical lattice; when the number of lattice sites is commensurate to the number of atoms in the condensate this produces lattice sites occupied by single atoms, which is an excellent starting point for generating a large number of qubits.

These apparent advantages have led to the development of an extensive body of theoretical work on the topic, for example Jaksch (2004). In contrast, experimental

implementation is still in an early stage of development: Yavuz *et al.* (2006) have demonstrated the ability to perform  $\pi/2$  rotations of the qubit state in approximately 180 ns with no observed cross-talk to the adjacent qubit site while Schrader *et al.* (2004) have demonstrated loading of single atoms into a number of sites in a one-dimensional optical lattice, as well as the ability to perform single-qubit operations and to arbitrarily re-arrange the qubits.

### 1.1.2 Accordion Lattices

For quantum computation it is necessary but not sufficient (DiVincenzo, 1995) to be able to deterministically prepare single-qubit states and then to be able to address them individually. These two requirements are in competition for cold atoms because the Mott insulator transition which provides the easiest way of reliably obtaining single atom occupation of lattice sites also requires that atoms initially be able to tunnel between lattice sites. Thus the Mott insulator state is usually obtained (Greiner *et al.*, 2002) in an optical lattice with a period of  $\frac{\lambda}{2}$ , or approximately 400 nm. At such a small lattice spacing, the lattice sites cannot be individually addressed by optical means.

Several attempts have been made to bridge this gap: one approach is simply to change the periodicity of the lattice or of the loading. In this vein, Peil *et al.* (2003) demonstrated the loading of every third site of a lattice with 500 nm periodicity by using a second lattice with a period of 1.5 microns as the first stage of loading, while Scheunemann *et al.* (2000) have demonstrated an optical lattice using a retroreflected CO<sub>2</sub> laser: the lattice periodicity of 5.3 microns enabled addressing of single lattice sites.

A second approach is to use some form of adjustable optical potential that is not a lattice: such a potential could be formed by individual focussed beams with adjustable position or by using a spatial light modulator to generate a flexible

dipole potential. In this fashion we envision using a narrowly-spaced array of focussed beams to pass through the Mott insulator transition and then expand the array to allow addressability. Dumke *et al.* (2002) demonstrated a trapping potential formed by light focussed through a micro-fabricated array of lenses: by illuminating the lens array with multiple beams at different angles this can generate multiple arrays of dipole traps with separation dependent on the angle. In Oxford, Boyer *et al.* (2006) demonstrated dynamic splitting of a Bose-Einstein condensate using a spatial light modulator.

Another approach is to use an optical lattice with a lattice spacing which can be adjusted during the experiment, typically called an accordion lattice. Similarly to adjustable non-lattice potentials this could be used with a small lattice spacing to load the lattice sites and then moved to a larger lattice spacing for addressability. Huckans (2006) carried out a variety of experiments with a BEC using a one-dimensional accordion lattice based on a galvanometer-driven mirror and a beam-splitter to generate two beams with dynamically controllable angle between the beams. Li *et al.* (2008) have imaged a lattice potential in one dimension based on a similar concept to the scheme described in chapter 6.

### 1.1.3 Simulating Condensed Matter Systems

In section 1.1.1 we discussed some of the applications of optical lattice systems to quantum computing, which can be seen as an extension of classical digital computing. There is also considerable theoretical interest in extending analogue computing to quantum systems via direct quantum simulation: in other words, studying a simple model quantum system to derive insight into the behavior of a more complicated system with similar elements. Feynman (1982) pointed out that a simulation of a non-trivial quantum system must consider interactions between all the particles: this leads to an exponential increase in the computational resources

and time required for simulation as particle number increases linearly. Thus quantum systems of practical interest are impractically complicated to simulate using a classical digital computer and so one needs to use a quantum simulation instead.

If one can obtain an optical lattice with single-atom occupation at each lattice site (often referred to as an atomic crystal) it becomes an ideal system to simulate condensed matter systems: the Mott insulator transition provides a method for achieving such a crystal in an optical lattice potential. Beyond this, optical lattices have other significant advantages for simulating many-body quantum systems: the shape of the potential can be adjusted almost arbitrarily by clever arrangement of optical beams, while the intensity and the phase of the potential can be adjusted using acousto- or electro-optical techniques. This gives the experimentalist many potential ways to change the Hamiltonian being simulated; some of these possible applications are discussed in Bloch (2005).

The first steps in experimental implementation of these ideas have already been taken. Notably Albiez *et al.* (2005) demonstrated a Josephson junction between adjacent Bose-Einstein condensates in a double-well potential including a transition between an oscillating regime and self-trapping dependent on the initial population difference between the wells. Another interesting area has been the application of random or pseudo-random potentials to Bose-Einstein condensates: Billy *et al.* (2008) and Roati *et al.* (2008) independently demonstrated Anderson localization, which arises when a disordered potential weaker than the chemical potential nevertheless limits the expansion of the wavefunction.

A final area of interest which has motivated our experiment is the idea of simulating the effect of magnetic fields in condensed matter system by using rotation in an optical lattice. Explored theoretically by Palmer *et al.* (2008) and others, the analogy between rotation and a magnetic field perpendicular to the plane of the lattice arises because the forces exerted by the two situations have the same

form  $\kappa \mathbf{K} \times \mathbf{v}$ , where  $\kappa$  is a constant,  $\mathbf{v}$  is a vector in the plane of the optical lattice and  $\mathbf{K}$  is a vector perpendicular to the plane of the optical lattice.

## 1.2 Experimental Concept

Our experiment was designed to implement a more flexible optical lattice-like potential: while this general idea has remained constant, our specific experimental implementation is now quite different from the concept we had when I began my D.Phil. In this section I will briefly discuss the original concept, as familiarity with it will explain some of the choices made in the design and construction of the system. I will also discuss some of the experimental problems we encountered in pursuit of the original concept before moving on to describe the concept behind the work reported here.

### 1.2.1 Original Concept

When our experiment was designed (by Martin Shotter, Andrian Harsono and Gerald Hechenblaikner) the concept was to implement a flexible lattice-like potential from individual focussed Gaussian beams. A schematic of how this would have worked (including trapping beam cross-section) is shown as figure 1.1.

We installed an objective lens with a numerical aperture of 0.27 so that the individual beams have diffraction limited waist sizes: thus one can imagine with the Gaussian beams separated by a distance of the order of their waist size an approximately Gaussian potential would be obtained. Such a potential is illustrated in figure 1.2.

We intended to use the flexibility of this potential (with individual rows or columns of microtraps able to be moved independently) to explore such issues as sub-shot noise interferometry, Josephson tunneling and BECs in random poten-

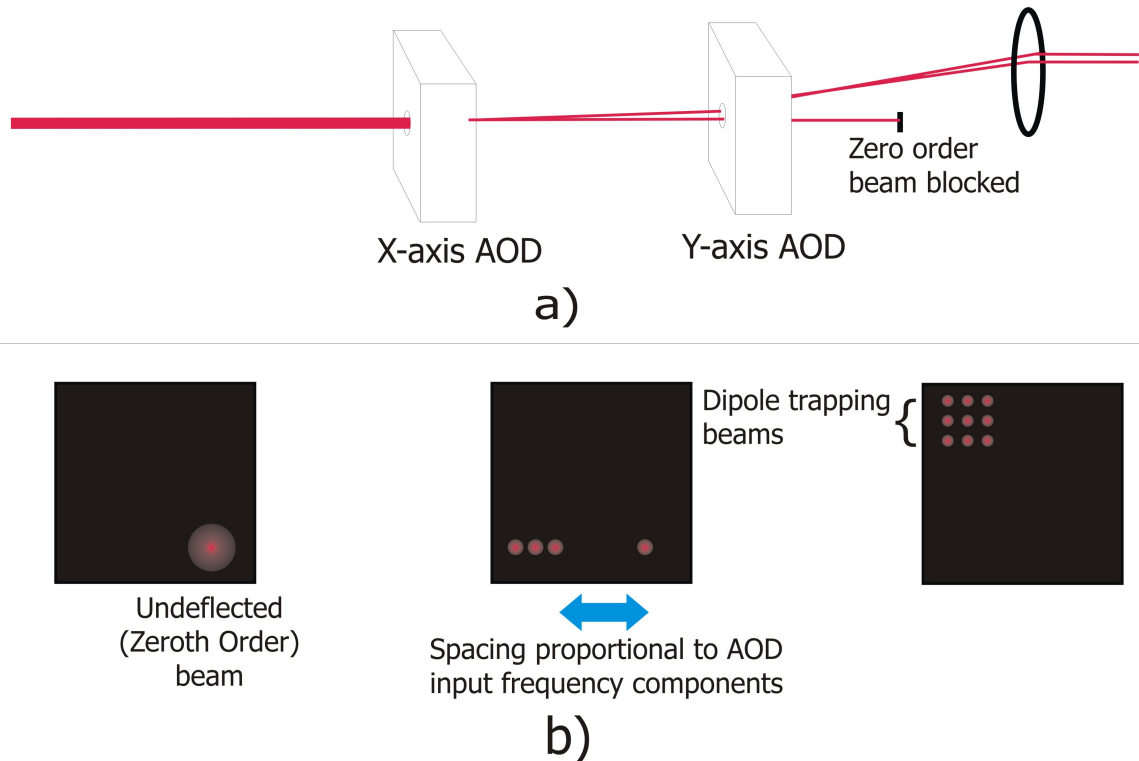


Figure 1.1: The original concept which inspired our experimental design. a) is an illustration of the path of the dipole trapping beam through the acousto-optical deflectors in the  $x$  and  $y$  axes: in practice the two modulators are as close together as possible. b) illustrates the beam cross-section in the plane perpendicular to the direction of propagation of the dipole beam as it would appear at the position of the atoms.

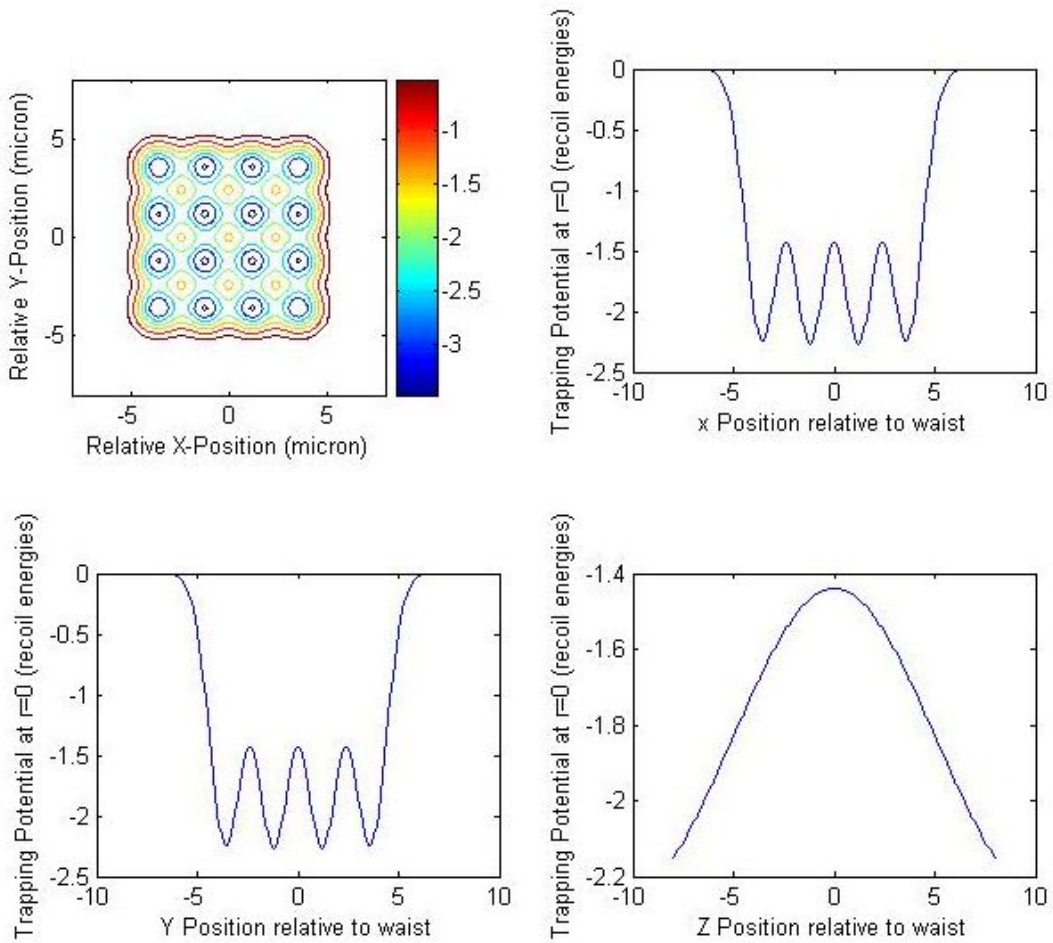


Figure 1.2: These graphs illustrate various aspects of the trap formed by several adjacent Gaussian beams; here there are a 4x4 array of beams with a 1.6 micron waist separated by 2.4 microns and 100 nW of power per beam. Note that the axial profile in lower-right graph is correctly anti-trapping, as the profile is taken at  $x = y = 0$  (a potential maximum). The recoil energy referred to in the labels is the ‘lattice’ recoil energy - e.g. the recoil energy for a lattice with spacing 2.4 microns. The color-bar on the top-left graph is also in units of lattice recoil energies.

tials.

We did implement this scheme and observed atoms held in multiple dipole traps (Harsono, 2006), but a few experimental issues made it more difficult than we had expected. The major issue was to do with coherence: the simulation illustrated in figure 1.2 assumes completely incoherent beams so that the intensities of the Gaussian beams may be added. In the experimental arrangement one laser beam provides the basis for all of the focussed spots, so there will always be some interference between beams: this interference will occur at a beat frequency equal to the difference between the frequencies of the two beams, thus the intensity of the beams may only be added when this beat frequency is much larger than the trapping frequencies. As the frequency difference between the beams also determines their separation in the focal plane, bringing the traps closer together reduces the frequency difference and thus brings the beat frequency towards the trapping frequency: this will clearly provide one bound on the minimum spacing between intensity maxima, though we were not able to determine if this would be the limiting factor.

There were two more minor issues that also caused us some difficulty in trying to implement these arrays of microtraps. One was a question of alignment: we did not have an absorption imaging beam propagating along the same axis as the dipole trapping beams, so we had no good reference point from which to start alignment of the dipole trapping beams. (We implemented such an additional absorption beam later: this is discussed in section 3.9.) It was also difficult to measure and control the power of the lattice trapping beam that we would have during the original experiment: the potential graphed in figure 1.2 was for only 100 nW per beam.

### 1.2.2 Revised Concept

The experimental issues discussed above led us to change our method for obtaining a flexible lattice potential. The final scheme is discussed extensively in section 6.3: to summarize the key idea, rather than generating a lattice like potential by using several lattice beams we generated the optical lattice potentials by sending parallel pairs of beams through the four-lens objective. The lattice spacing depends on the angle at which the beams intersect, and thus can be adjusted by changing the spacing between the beams at the four-lens objective.

Additionally, lack of coherence between the orthogonal pairs of beams is guaranteed by using orthogonal polarizations for the two sets of beams. A final key advantage of this revised setup is that the optical lattices can be rotated by rotating the parallel pair of beams around the optical axis of the 4-lens objective.

## CHAPTER 2

---

# Bose-Einstein Condensation: Theoretical Overview

Since it was first achieved by Anderson *et al.* (1995), Bose-Einstein condensation in dilute atomic vapors has become a common tool for experiments in quantum physics. Moving beyond simple bosonic condensates, new frontiers have been opened up with the loading of a BEC into the Mott insulator state by Greiner *et al.* (2002) and the achievement of quantum degeneracy of fermion gases by Regal *et al.* (2004). In this section, I shall describe briefly the theory describing Bose-Einstein condensation in a harmonic potential.

### 2.1 The Basics

The experimental achievements of the last ten years in relation to ultra-cold atomic gases have been matched by a proliferation of theoretical work. Fortunately for those of us more inclined to experiment than theory this growth has included introductory texts as well as advanced research, including the excellent works by

Pethick and Smith (2002) and Foot (2005).

Here, I shall concentrate primarily on the description of Bose-Einstein condensation in a harmonic trap. This corresponds to the potential experienced by very cold atoms ( $T < 1 \mu\text{K}$ ) in our magnetic trap.

### 2.1.1 The Bose distribution for material particles

As is well known in statistical mechanics (see Glazier and Wark (2001)) for photons in thermal equilibrium the number of photons  $N_i$  found in the state with energy  $\epsilon_i$  is given by the distribution  $f(\epsilon)$ , where:

$$N_i = f(\epsilon_i) = \frac{1}{e^{\beta\epsilon_i} - 1} \quad (2.1)$$

where  $\beta = (k_B T)^{-1}$ . Note that in the case of photons, the number of particles is directly proportional to the energy of the system; as the temperature tends towards zero, the number of photons in the system does likewise. This becomes physically unacceptable when we turn our attention to material bosons like atoms of Rubidium-87, so an additional constraint must be introduced to ensure that the sum of  $N_i$  over all energy levels  $\epsilon_i$  is equal to the number of particles in the system  $N$ . If this is done, it leads to the full Bose distribution  $f_B$  given below.

$$N_i = f_B(\epsilon_i) = \frac{1}{e^{\beta(\epsilon_i - \mu)} - 1} \quad (2.2)$$

$\mu$  is called the chemical potential, and is a function of  $N$  and  $T$  determined by the condition

$$\sum_{i=0}^{\infty} N_i = \sum_0^{\infty} \frac{1}{e^{\beta(\epsilon_i - \mu)} - 1} = N \quad (2.3)$$

### 2.1.2 Bose-Einstein Condensation

Let us consider  $\mu$  in equation 2.2. For a system of fixed, finite particle number we require that the occupation number  $N_i$  be finite and greater than or equal to zero. What does this imply for  $\mu$ ? Let us consider first letting  $\mu$  tend to zero; this amounts to removing the restriction that particle number is fixed and thus reproduces equation 2.1.

Now consider large values of  $\mu$ : for this case, we obtain negative occupation numbers which are clearly unphysical. In order to keep all occupation numbers positive, we find the condition  $\mu < \epsilon_0$  where  $\epsilon_0$  is the ground state energy.

As  $T$  approaches zero,  $\mu$  will tend to  $\epsilon_0$ ; thus the occupation number of a state with energy  $\epsilon_n$  cannot be greater than  $(e^{\beta(\epsilon_n - \epsilon_0)})^{-1}$ . If we sum the occupation number for all states with  $n > 0$  and find a total less than  $N$ , the excess must be located in the ground state. When this excess becomes a significant fraction of  $N$  we have a macroscopic number of atoms sharing the same wavefunction: this is known as a Bose-Einstein condensate (BEC). This very large occupation of a single quantum state makes BEC a phenomenon of great physical interest as it allows experimental probing of quantum behavior on length scales of ten to a hundred microns instead of the usual scales of angstroms.

## 2.2 The Statistical Mechanics of BEC

The schematic argument outlined above gives a good first handle on the phenomenon of Bose-Einstein condensation, but does not answer crucial questions like where the transition to BEC appears and to what extent a real system will depart from the ideal system of thought experiments. To answer these questions, we must consider the statistical mechanics of the process.

As a first approximation, we assume that condensation occurs at low temper-

ature. Just before condensation we can then assume that  $\mu \approx \epsilon_0$  and so we can rearrange equation 2.3:

$$\begin{aligned} \sum_{i=0}^{\infty} N_i &= \sum_0^{\infty} \frac{1}{e^{\beta(\epsilon_i - \mu)} - 1} \\ &= \frac{1}{e^{\beta(\epsilon_0 - \mu)} - 1} + \sum_{i=1}^{\infty} \frac{1}{e^{\beta(\epsilon_i - \mu)} - 1} \end{aligned} \quad (2.4)$$

$$= N_0 + \int_{\epsilon_0}^{\infty} \frac{g(\epsilon)}{e^{\beta(\epsilon - \epsilon_0)} - 1} d\epsilon \quad (2.5)$$

$$= N_0 + \int_0^{\infty} \frac{g(\epsilon)}{e^{\beta(\epsilon)} - 1} d\epsilon \quad (2.6)$$

Here, we treat the ground state as a reservoir separate to the excited states and assume that the gap between energy levels is smaller than the thermal energy. Having done this, we can change the sum over individual states to an integral over energies if we multiply the Bose distribution by the density of states at energy  $\epsilon$ ,  $g(\epsilon)$ . This produces equation 2.4 if we consider a low-temperature regime such that  $\mu \approx \epsilon_0$ . If we assume a large number of particles (in our experiment we typically observe  $10^5$  atoms at condensation) we can neglect zero-point energy and take  $\epsilon_0 = 0$ . This produces equation 2.5.

Note that this combination of assumptions also has  $\mu = 0$ ; this no longer leads to violating atom number conservation because of the separate consideration of the ground state. We have replaced  $\mu$  with  $N_0$  as a guarantor of constant particle numbers.

### 2.2.1 Density of States in a Harmonic Potential

Before we can evaluate the integral in equation 2.5 we need to know the density of states for particles in an anisotropic harmonic potential. Such a potential has

the form:

$$V(x, y, z) = \frac{m}{2}(\omega_x^2 x^2 + \omega_y^2 y^2 + \omega_z^2 z^2) \quad (2.7)$$

and quantized energy states:

$$\frac{\epsilon(n_x, n_y, n_z)}{\hbar} = (n_x + \frac{1}{2})\omega_x + (n_y + \frac{1}{2})\omega_y + (n_z + \frac{1}{2})\omega_z \quad (2.8)$$

If we assume that internal degrees of freedom are suppressed (by spin polarization, for example) and energy levels are sufficiently large that the zero-point energy may be neglected in equation 2.8 then a single state will occupy a volume of  $\hbar^3 \bar{\omega}^3$  in the available volume of (positive) energy space, where  $\bar{\omega}$  is the geometric mean of the trapping frequencies  $\omega_x$ ,  $\omega_y$  and  $\omega_z$  ( $\bar{\omega} = \sqrt[3]{\omega_x \omega_y \omega_z}$ ). The total number of available states is then given by the integral:

$$\begin{aligned} G(\epsilon) &= \frac{1}{\hbar^3 \omega_x \omega_y \omega_z} \int_0^\epsilon d\epsilon_1 \int_0^{\epsilon - \epsilon_1} d\epsilon_2 \int_0^{\epsilon - \epsilon_1 - \epsilon_2} d\epsilon_3 \\ &= \frac{\epsilon^3}{6\hbar^3 \bar{\omega}^3} \end{aligned} \quad (2.9)$$

The density of states is then, by differentiation:

$$g(\epsilon) = \frac{dG(\epsilon)}{d\epsilon} = \frac{\epsilon^2}{2\hbar^3 \bar{\omega}^3} \quad (2.10)$$

### 2.2.2 The transition to BEC

Armed with the density of states, we look again at equation 2.5 to find the critical temperature  $T_c$  at which Bose-Einstein condensation occurs. Recalling the definition of BEC as macroscopic occupation of the ground state, we can see that just before this occurs the number of atoms in excited states  $N_{ex}$  will be equal to the total number of atoms  $N$ . We use this requirement to define  $T_c$  by using the

expression for  $g(\epsilon)$  from equation 2.10:

$$\begin{aligned} N &= N_{ex}(T_c) \\ &= \int_0^\infty \frac{g(\epsilon)}{e^{\beta_c(\epsilon)} - 1} d\epsilon \\ &= \int_0^\infty \frac{1}{e^{\beta_c(\epsilon)} - 1} \frac{\epsilon^2}{2\hbar^3\bar{\omega}^3} d\epsilon \end{aligned} \quad (2.11)$$

where  $\beta_c = (k_B T_c)^{-1}$ . By changing the variable of integration to  $x = \frac{\epsilon}{k_B T_c}$  we obtain:

$$N = \frac{(k_B T_c)^3}{2\hbar^3\bar{\omega}^3} \int_0^\infty \frac{x^2}{e^x - 1} dx \quad (2.12)$$

$$= \frac{(k_B T_c)^3}{2\hbar^3\bar{\omega}^3} \Gamma(3)\zeta(3) \quad (2.13)$$

where the second equation follows from the first by applying the definition of the Riemann zeta function for real numbers greater than one (equation 2.14) and the definition of the gamma function (equation 2.15).

$$\zeta(n) = \Gamma(n)^{-1} \int_0^\infty \frac{u^{n-1}}{e^u - 1} du \quad (2.14)$$

$$\begin{aligned} \Gamma(p) &= \int_0^\infty x^{p-1} e^{-x} dx \\ &= (p-1)! \text{ where } p \text{ is an integer} \end{aligned} \quad (2.15)$$

In our experiment the trapping potential has frequencies  $\omega_x = 5.4 \times 2\pi \text{ s}^{-1}$  and  $\omega_y = \omega_z = 167 \times 2\pi \text{ s}^{-1}$ . As  $\Gamma(3) = 2$ , this gives the transition temperature for 500,000 atoms:

$$\begin{aligned} k_B T_c &= \frac{\hbar\bar{\omega}\sqrt[3]{N}}{\sqrt[3]{\zeta(3)}} \\ &\approx 0.94\hbar\bar{\omega}\sqrt[3]{N} \end{aligned}$$

$$T_c \approx 170 \text{ nK}$$

Attaining such low temperatures in dilute gases is a considerable experimental challenge - some of the techniques used are discussed in section 3. This figure is still an approximation: we neglected zero-point energy, for example. These effects are derived in detail in Pethick and Smith (2002), but for the relatively large condensates observed in our experiment these effects only alter the transition temperature by a few percent.

## 2.3 Quantum Mechanics of BEC

The statistical mechanical approach is very successful for predicting transition temperatures and the existence of Bose-Einstein condensation, but to understand the behavior of a condensate once formed we need to approach it quantum mechanically. In this section I will outline the major tool in this endeavor, the Gross-Pitaevskii equation that models BEC behavior in large-scale potentials.

A more detailed discussion of the quantum description of a Bose-Einstein condensate is given in chapter six of Pethick and Smith (2002).

### 2.3.1 The Gross-Pitaevskii Equation

To establish the conceptual framework, we consider first an ideal gas of non-interacting particles with integer spin (bosons). In this case, the quantum mechanical description is so simple as to be trivial: each atom occupies some state  $\phi_n$  which is an eigenstate of the single particle Hamiltonian:

$$H_{sp} = \frac{\mathbf{p}^2}{2m} + V_{ext} \quad (2.16)$$

where  $V_{ext}$  represents the trapping potential. The state of the atoms can be simply described by listing the number of atoms in each eigenstate  $n$ ; at zero temperature,

for example, a non-interacting gas will have condensed entirely into the ground state  $|N, 0, 0\dots 0\rangle$ .

Alkali gas atoms are notably non-ideal in their mutual interactions. In the general case these interactions are mathematically complicated, but in our case two important simplifications are possible. First, as the number density of atoms is low, we can neglect all but two-body collisions. (Three body recombination also occurs at non-negligible rates, but its effect is primarily to limit the lifetime of a magnetically trapped cloud.) Further, as we are dealing only with atoms at very low energy we can restrict our attention to what is known as ‘s-wave scattering’: collisions in which the relative angular momentum between the colliding particles is less than  $\hbar$ . It can be shown (see section 5.2 of Pethick and Smith (2002) for a derivation) that s-wave scattering can be modelled as scattering from a hard sphere of radius  $a_s$ , giving the pseudo-potential:

$$V_s(\mathbf{x}_1 - \mathbf{x}_2) = \frac{4\pi a_s \hbar^2}{m} \delta(\mathbf{x}_1 - \mathbf{x}_2) = U_{sc} \delta(\mathbf{x}_1 - \mathbf{x}_2) \quad (2.17)$$

where  $\mathbf{x}_i$  represents the position of particle  $i$  and  $a_s$  is a parameter known as the scattering length which may be imagined as the radius of the model hard sphere. This approximation holds provided the separation between atoms is much greater than the scattering length. For Rubidium, s-wave scattering lengths are on the order of one hundred times the Bohr radius  $a_0$ , or approximately 5.3 nm. (See Table III in Weiner *et al.* (1999).) Thus the limiting density for the pseudo-potential to be applied is on the order of  $10^{25}$  atoms  $\text{m}^{-3}$ , many orders of magnitude greater than the typical density of our cloud ( $\approx 10^{20}$  atoms  $\text{m}^{-3}$ ). Thus we can see that the pseudo-potential approximation is excellent for our purposes.

Using this approximation, we obtain the single-quantized Hamiltonian for ul-

tracold interacting alkali gases:

$$H_{int} = \sum_{i=1}^N \left\{ \left( \frac{\mathbf{p}^2}{2m} + V_{ext} \right) + \sum_{j < i} V_s(\mathbf{x}_i - \mathbf{x}_j) \right\} \quad (2.18)$$

Here the sum over  $j < i$  serves to ensure that the interaction between particles  $i$  and  $j$  is only counted once overall. We take the Hartree approximation, assuming that all the atoms are in the same state  $\phi$ . Then the energy of the system can be found by substituting 2.17 into 2.18. For convenience, we replace  $\phi$  with  $\psi = \sqrt{N}\phi$ , so  $|\psi(x)|^2$  gives the number density of the cloud.

$$E = N \int \left( \frac{\hbar^2}{2m} |\nabla \phi|^2 + V_{ext} |\phi|^2 + \frac{N-1}{2} U_{sc} |\phi|^4 \right) d\mathbf{x} \quad (2.19)$$

$$\approx \int \left( \frac{\hbar^2}{2m} |\nabla \psi|^2 + V_{ext} |\psi|^2 + \frac{U_{sc}}{2} |\psi|^4 \right) d\mathbf{x} \quad (2.20)$$

We now make use of the variational principle, assuming that function  $\psi$  which minimizes the energy of the system will be a near approximation to the system's ground state. Our attempt to minimize the energy is subject to the constraint that we must conserve the particle number  $N = \int |\psi|^2 d\mathbf{x}$ . Using the method of Lagrange multipliers, we thus attempt to minimize the expression:

$$\delta E + \mu \delta N = 0 \quad (2.21)$$

As  $\psi$  is a complex function, we can regard its real and imaginary parts as varying independently; equivalently, we can let  $\psi^\dagger$  vary independently of  $\psi$ . Differentiating by  $\delta\psi^\dagger$ , we obtain from the minimization condition 2.21:

$$\frac{\hbar^2}{2m} \nabla^2 \psi + V_{ext} \psi + U_{sc} |\psi|^2 \psi = \mu \psi \quad (2.22)$$

Equation 2.22 is the Gross-Pitaevskii equation. As mentioned earlier, this

model is an excellent tool for describing Bose-Einstein condensates in potentials which vary slowly relative to the wavefunction.

## CHAPTER 3

---

# Bose-Einstein Condensation in Practice

A detailed description of the methods and apparatus used to achieve BEC in our apparatus is provided by Harsono (2006); rather than reproduce that information here, I shall merely describe the principle and state the results achieved at each stage.

Experimentally we obtain atoms to be cooled from a getter (a ceramic material which has captured rubidium to be released when it is heated) which produces rubidium atoms at room temperature; for BEC, the atoms need to be cooled below 170 nK. Two complementary technologies let us bridge this gap: magneto-optical trapping (MOT) and magnetic trapping.

In magneto-optical trapping, the momentum transferred to the atoms by resonant scattering of photons is exploited to slow and capture atoms at room temperature and reduces the atom temperature sufficiently (to a few  $\mu\text{K}$ ) that the atoms can be trapped within a magnetic potential. Evaporative cooling can be used within the magnetic potential to reduce the temperature of the atoms to quantum

degeneracy. The principles of operation of both MOTs and magnetic traps are well described in Metcalf and van der Straten (2002): in this chapter I will give a brief overview of each with some details relevant to our experiment.

### 3.1 Alkali Gases

Photons carry an extremely small amount of momentum relative to that of an atom, so a very large number of photons must be scattered for significant laser cooling to occur; this is most easily accomplished by use of a closed, cycling transition. In such a transition the selection rules mean that an atom in the excited state of the transition is overwhelmingly likely to decay back to the initial state from which it was excited. Thus the atom is immediately ready to absorb another photon, continuing the cooling process.

As the alkali metals have only one electron outside a closed shell, the first three available states for the electron are  $^2S_{1/2}$ ,  $^2P_{1/2}$  and  $^2P_{3/2}$ . (For rubidium-87, these states and the most useful transitions between them are illustrated in figure 3.1.) This structure of available states includes a closed cycling transition between the  $^2S_{1/2}$  F=2 state and the  $^2P_{3/2}$  F=3 state and thus alkali gases are widely used in laser cooling experiments. The popularity of alkali gases can be judged from the initial observations of BEC in 1995, made in rubidium (Anderson *et al.*, 1995), sodium (Davis *et al.*, 1995) and lithium (Bradley *et al.*, 1995).

In the ensuing years, BEC has also been achieved in hydrogen (Fried *et al.*, 1998), caesium (Weber *et al.*, 2003) and potassium (Modugno *et al.*, 2001) - though due to complications in scattering and other parameters these elements required techniques beyond the magnetic trapping and evaporation used for the elements condensed in 1995.

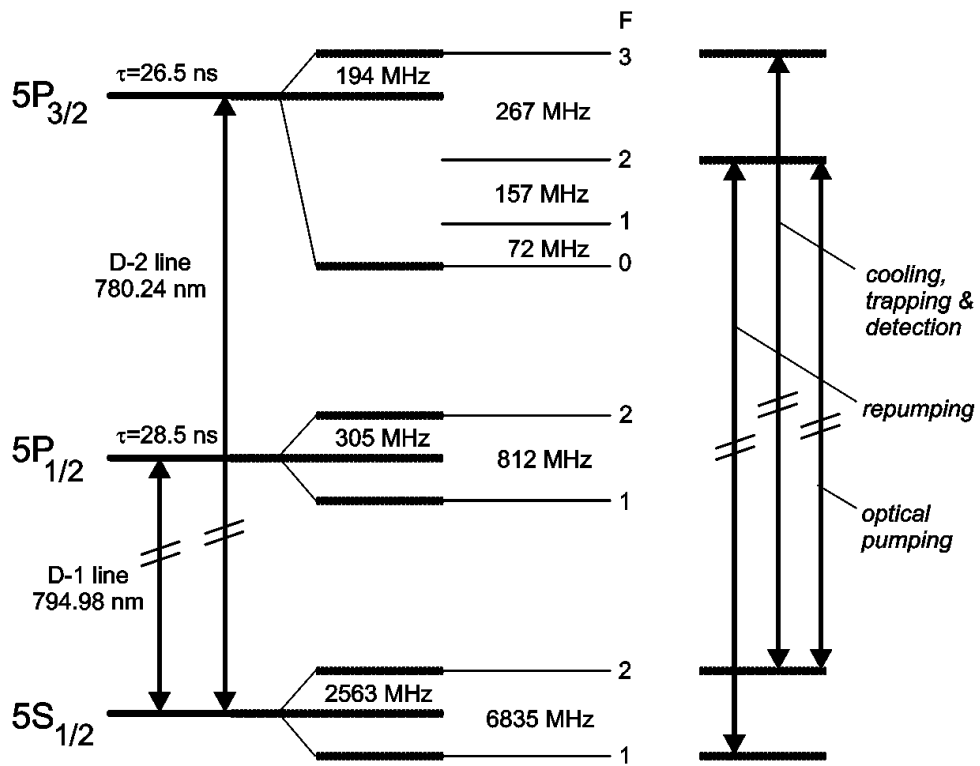


Figure 3.1: This figure illustrates the lowest three energy levels for  $^{87}\text{Rb}$ 's single valence electron, with the transitions used for laser cooling and trapping indicated. Figure is taken from Harsono (2006), based on data from Steck (2003).

### 3.1.1 Rubidium-87

In our experiment we use rubidium-87, which has emerged as perhaps the easiest isotope to condense. The energy levels of rubidium are illustrated in figure 3.1, with some of the most useful transitions between them. For laser cooling, we make use of the cycling transition within the D2 line between the  $F=2$  and  $F'=3$  states<sup>1</sup>. A small but significant fraction of the atoms are excited non-resonantly to the  $F'=2$  state. From this state, they can decay to either  $F=1$  or  $F=2$ . If they decay to  $F=1$  they thus depart from the cycling transition; in order to return these atoms to the cycling transition we add a laser tuned to the  $F=1$  to  $F'=2$  transition, known as the repumper. Atoms initially decaying to the  $F=1$  state will thus be excited back

<sup>1</sup>From this point on, the notation  $F'$  will refer to the  $F$  value of the  $5\text{p } ^2\text{P}_{3/2}$  state while  $F$  will refer to the  $F$  value of the  $5\text{s } ^2\text{S}_{1/2}$  ground state

to  $F'=2$  until they decay back to  $F=2$ , rejoining the cycling transition.

A third transition - from  $F=2$  to  $F'=2$  - is used as the opposite of the repumper, pushing atoms into the  $F=1$  state. By adding an appropriate quantization axis and using circularly polarized light this can also be arranged to favor  $\Delta m_F = -1$  transitions. This is known as the optical pumping transition, and is used to populate the  $F=1$ ,  $m_F = -1$  state for magnetic trapping.

## 3.2 Lasers

Figure 3.2 illustrates the optical layout needed to obtain light resonant with the three transitions discussed in section 3.1.1. We have two commercial diode lasers: one is tuned to the laser cooling transition (known as the master) and one to the repumping transition. The master diode is an Eagleyard anti-reflection coated diode (EYP-RWE-0790) and gives approximately 80 mW of output power while the repumper is a Sanyo DL7140 uncoated diode giving approximately 60 mW of power.

These diodes are mounted with external cavities: this means that optical feedback and stabilization for the laser is provided using the diffracted orders from a diffraction grating. In combination with the laser diode's internal cavity this produces laser light with a linewidth of approximately 10 kHz. Both of these lasers are locked to absorption features in rubidium using a combination of current and cavity modulation; the master is locked to the  $F'=2$  to  $F'=3$  crossover of the D2 line while the repumping laser is locked to the  $F=1$  to  $F'=2$  transition. The repumping laser provides all the repumping light needed for the experiment. We need a larger amount of cooling light than a single diode laser could supply, so we use light from the master to inject two slave lasers. Each of the slave lasers provides the cooling light one of the two MOTs discussed in section 3.3. The diode used for the first (or

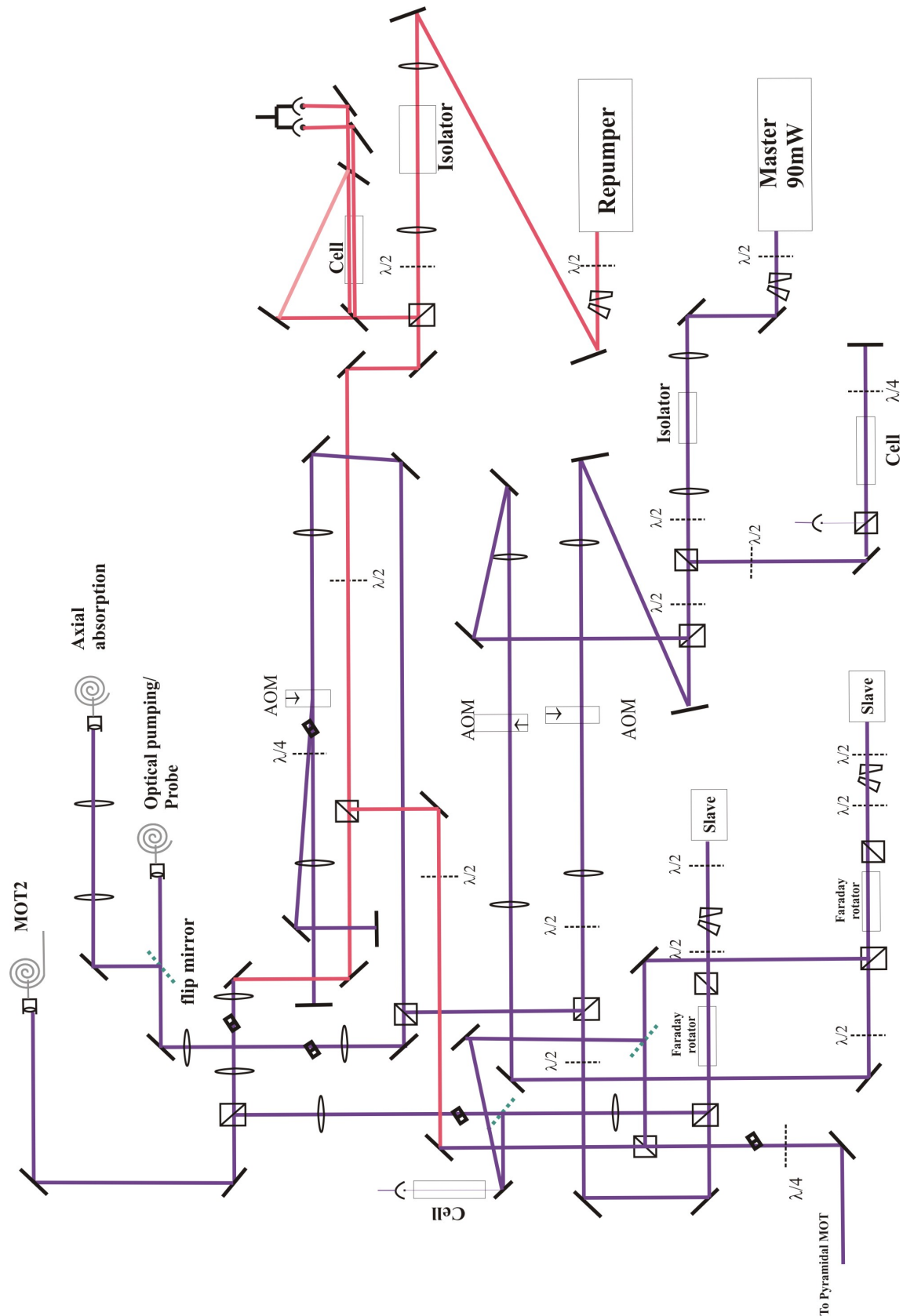


Figure 3.2: This figure illustrates the layout of the optical table which is devoted to generating the various frequencies of laser light which are required for laser cooling and trapping of Rubidium.

pyramid) MOT slave is an Eagleyard 100 mW uncoated diode (EYP-RWL-0780); the second MOT slave is another Sanyo.

The lasers described above cover two of the three transitions; finally the optical pumping and probing beams are generated by using a double-pass acousto-optic modulator setup. This modulator takes advantage of the 'cross-over resonance': a third absorption peak which arises when the laser in a pump-probe spectroscopy setup is tuned halfway between two resonances<sup>2</sup> to frequency shift light from the master laser over the approximately 133 MHz between the cross-over resonance to which the laser is locked (see above) and the F=2 to F'=2 resonance.

### 3.3 Magneto-Optical Traps

In our experiment, we use two MOTs to accomplish the trapping and cooling of atoms from the getter: this has the advantage of separating the relatively high-pressure region around the getter from the magnetic trapping region and thus extending the magnetic trap lifetime. The MOT in the getter region is a pyramid MOT, as initially developed by Arlt *et al.* (1998) - a single beam illuminates an inverted pyramid of mirrors with a gap at the peak. The reflections from the sides of the mirror create a six-beam MOT, while the gap at the peak results in a 'hole' in the MOT; slow atoms are thus pushed by an unpartnered laser beam into the magnetic trapping region. The atoms pass through an aperture which maintains the pressure differential between the two regions.

On reaching the second cell, the atoms are trapped by a standard six-beam MOT. This has a lifetime of approximately 240 s, and reaches equilibrium with approximately  $10^8$  atoms trapped.

---

<sup>2</sup>When the laser is tuned to a resonance, both the pump and the probe beams interact with atoms which have a velocity of zero. When the laser is tuned to the cross-over resonance halfway between two resonances some atoms will be moving at a speed which brings the pump beam into resonance with one transition while the probe beam is in resonance with the other.

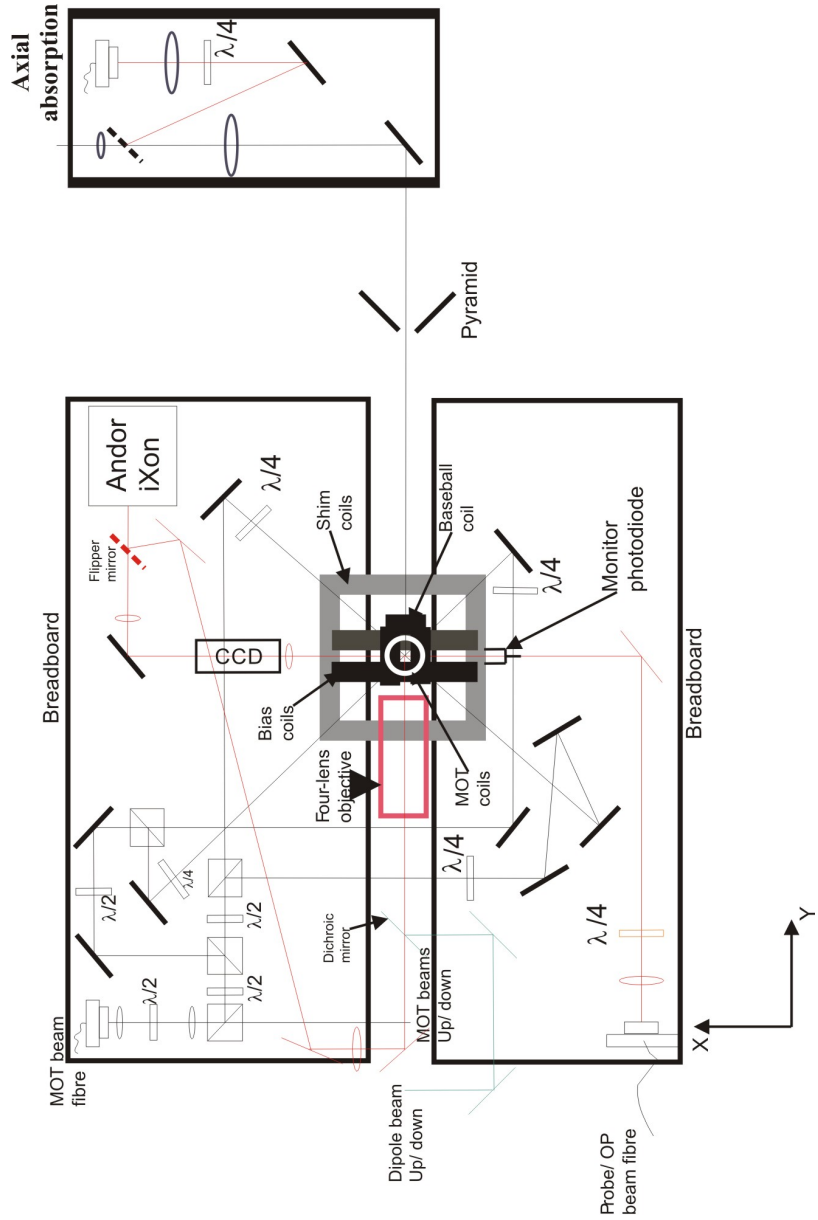


Figure 3.3: This figure illustrates the layout of the optical table surrounding the vacuum system. Most of the optics shown are there for the second MOT; also shown are elements of the absorption, axial absorption and fluorescence imaging systems and of the dipole trapping path.

## 3.4 Compressed MOT, Molasses and Optical Pumping

In a magneto-optical trap containing a large number of atoms, the size of the cloud is often increased by radiation pressure; this is the term given to the heating effect observed when the resonant light given off by an excited atom decaying is reabsorbed before escaping the cloud. Before loading into the magnetic trap it is important to reduce the size of the cloud as much as possible to give a high phase-space density. This is accomplished in our sequence by suddenly increasing the MOT detuning from -10 MHz to -30 MHz and by increasing the quadrupole field gradient. The increased detuning reduces the radiation pressure while the increased field gradient tightens the MOT itself. During this compressed MOT (CMOT) stage we use smaller coils known as the shims to move the cloud as close to the centre of the magnetic trap as possible.

Clearly loading hot atoms into the magnetic trap will also result in a hot cloud in the magnetic trap! Thus immediately after the CMOT stage we apply optical molasses (similar to the laser cooling in a MOT, but with the Earth's magnetic field cancelled out - for a detailed description see Metcalf and van der Straten (2002)) to reduce the cloud temperature. In this stage we increase the frequency detuning of the cooling light to approximately 60 MHz below the atomic resonance with the quadrupole field turned off and the shim coils set to cancel the background magnetic field.

At the end of the molasses stage we apply a magnetic field to set a quantization axis to the atoms and then illuminate them with the optical pumping beam (resonant with the  $F=2$  to  $F'=2$  component of the D2 line). This pumps all the atoms into the  $F=1$  multiplet of the ground state with a bias towards the  $m_F = -1$  state: this is the state we aim to trap (see section 3.5). Typically 60% of the available

atoms are trapped.

## 3.5 Magnetic Trapping

The Zeeman effect - that is, the splitting of atomic energy levels due to the interaction energy of the atomic magnetic moments in an external  $B$ -field - is well known to students of quantum mechanics. An excellent summary of the relevant quantum mechanics is given in sections 3.9 and 18.1 of Corney (1977).

To summarize: where the Zeeman splitting is small compared to the hyperfine structure and the LS coupling approximation applies (i.e. the hyperfine structure is much weaker than the spin-orbit interaction which in turn is much weaker than the electrostatic interactions) the Zeeman effect can be treated by simple perturbation theory, giving the result that the energy shift  $\Delta E_Z$  is:

$$\Delta E_Z = -\mu \cdot \mathbf{B} = g_F m_F \mu_B B \quad (3.1)$$

where  $\mu$  and  $\mathbf{B}$  are vectors representing the magnetic moment of the atom and the magnetic field respectively,  $g_F$  is the effective g-factor,  $m_F$  is the projection of the total angular momentum  $\mathbf{F}$  along the direction of the applied magnetic field,  $\mu_B$  is the Bohr magneton and  $B$  is the magnetic field strength. Figure 3.4 shows the splitting of the sub-levels of the ground state of  $^{87}\text{Rb}$  - including various effects beyond the scope of the simple perturbation theory given above.

Where the product  $g_F m_F$  is positive, the energy of the atom will be minimized at a minimum of the magnetic field. As we can see from figure 3.4, this condition is fulfilled for three states:  $F = 1, m_F = -1$ ;  $F = 2, m_F = 1$  and  $F = 2, m_F = 2$ . By generating a suitable minimum in the magnetic field, we can trap atoms in any of these three states - in this experiment, we trap in the  $F = 1, m_F = -1$  state as this state has a high collisional cross-section and thus will re-thermalize rapidly

during evaporative cooling.

The simplest possible arrangement for a magnetic trap is two identical coaxial coils carrying equal and opposite currents. As the coils are symmetrically arranged, there will be no magnetic field on the axis halfway between the two. The fact that the minimum point is at zero field is problematic for experiments with ultracold atoms: where magnetic field is small, the energy difference between trapped and untrapped  $m_F$  states is small, and so atoms make spontaneous transitions between states (Majorana flops) and are lost from the trap.

A similar field in one plane is produced by the Ioffe-Pritchard trap, illustrated in figure 3.5. Equal currents run through the four bars whose orientation defines the direction of the trap axis: each bar carries current in a direction opposite to its two nearest neighbors. This generates a quadrupole trapping field in the plane perpendicular to the axis of the trap with translational symmetry along the axis. Axial trapping is provided by the ‘pinch’ coils - these are spaced by much more than their radius in order to provide a non-uniform axial field with a minimum at the midpoint of the pair. This also displaces the field at the center of the trap from zero, so avoiding the issue of Majorana flopping discussed above.

Instead of using the Ioffe-Pritchard trap as illustrated in figure 3.5, we use a variant trap known as a baseball trap because the coils are arranged in the same fashion as the seams on a baseball (or a tennis ball). The field generated by this trap is equivalent to a Ioffe-Pritchard trap (Bergeman *et al.*, 1987), but gives a stronger confining field for a fixed amount of available current and allows slightly better optical access.

The arrangement of coils for the second MOT and the magnetic trap is shown in figure 3.6. The magnetic portion of the second MOT is formed by a pair of coaxial coils, shown. The magnetic trap is primarily from the current running through the baseball coil shown; we also use the bias and secondary bias coils. These allow

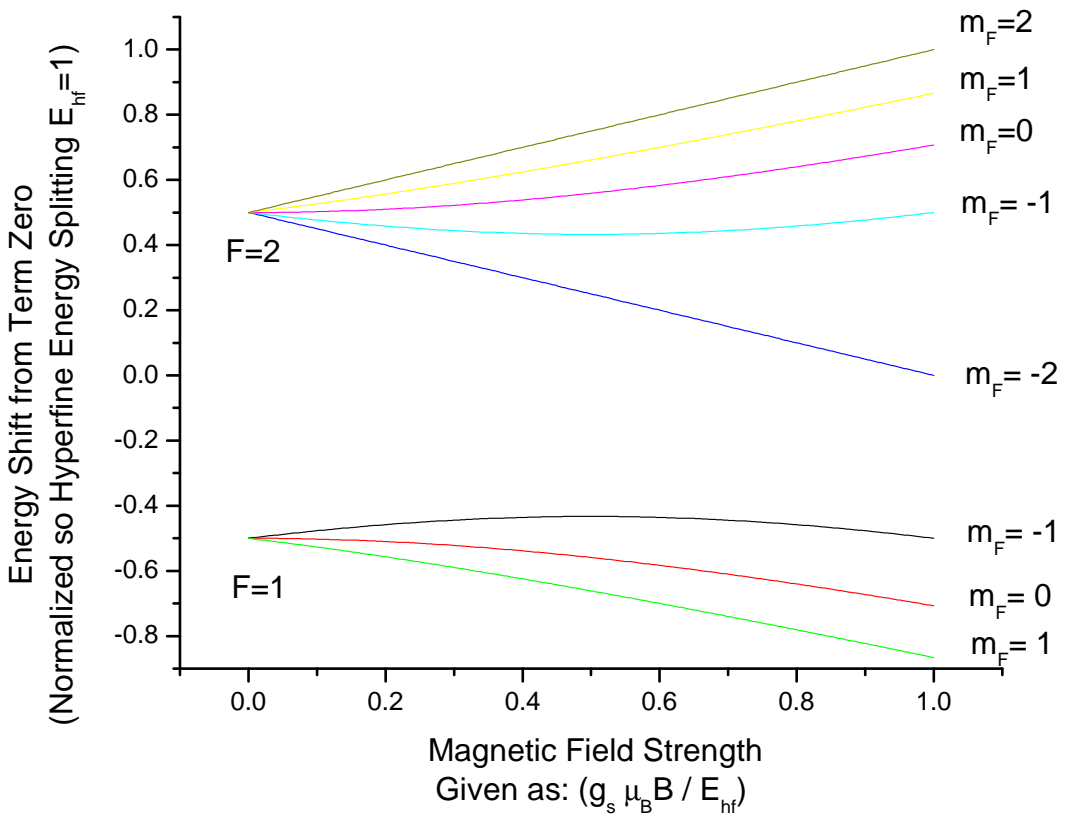


Figure 3.4: This figure shows the splitting of the Zeeman sub-levels of the ground state of  $^{87}\text{Rb}$  in the presence of an external magnetic field, including effects such as the quadratic Zeeman effect not discussed in the text. The x axis is magnetic field strength, scaled to the ratio between the Zeeman energy of the electron dipole in that field and the hyperfine energy splitting. The y axis is the Zeeman energy shift, also scaled to the hyperfine energy splitting. Individual states are labelled by the  $m_F$  states which describe them in the low-field approximation (i.e. at the far-left of the figure) on the far right: physical subtlety has been sacrificed for clarity of the diagram.

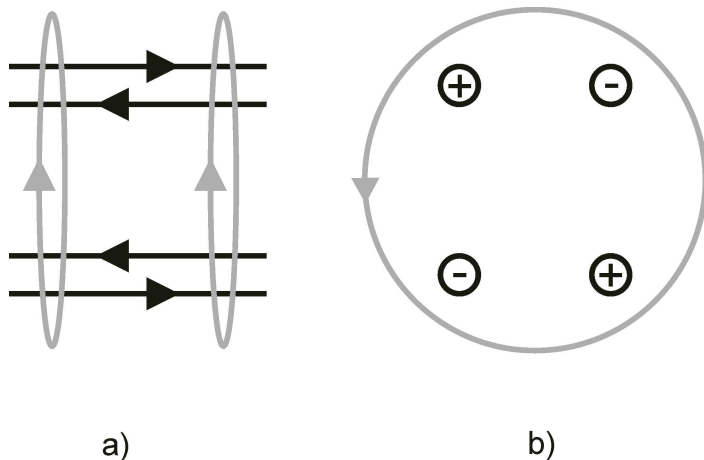


Figure 3.5: Here we see a schematic outline of the Ioffe-Pritchard trap. a) shows a view from the side of the trap and above it, while b) shows a view looking down the axis of the trap. Arrows indicate directions of current flow. The four bars running parallel to the trap axis generate a quadrupole field in the plane perpendicular to the bars; the two coils provide a trapping potential along the trap axis.

us to change the trap geometry during the experiment. This is primarily used to allow us to load the cloud from the molasses into a relatively weak magnetic trap to minimize heating. We can then tighten the radial confinement for more efficient evaporative cooling approximately adiabatically. The shim coils shown are used for fine adjustments of the magnetic field - for example, to move the cloud in the CMOT stage to the center of the baseball trap.

We measure the trapping frequencies for our trap by using the shim coils to displace the cloud from equilibrium and then measuring the cloud's position after a variable delay. We observe sinusoidal oscillations which correspond to the trapping frequency. For the weak trap used for initial loading, we find that the trapping frequencies are  $\omega_r = 2\pi \times 12$  Hz and  $\omega_a = 2\pi \times 4.8$  Hz, where  $\omega_r$  is the frequency in the direction perpendicular to the trapping axis and  $\omega_a$  is the trapping frequency along the trapping axis. After the trap has been tightened for evaporation, we observe oscillation frequencies  $\omega_r = 2\pi \times 167$  Hz and  $\omega_a = 2\pi \times 5.4$  Hz.

Care must be taken to avoid adding heat to the system when tightening the

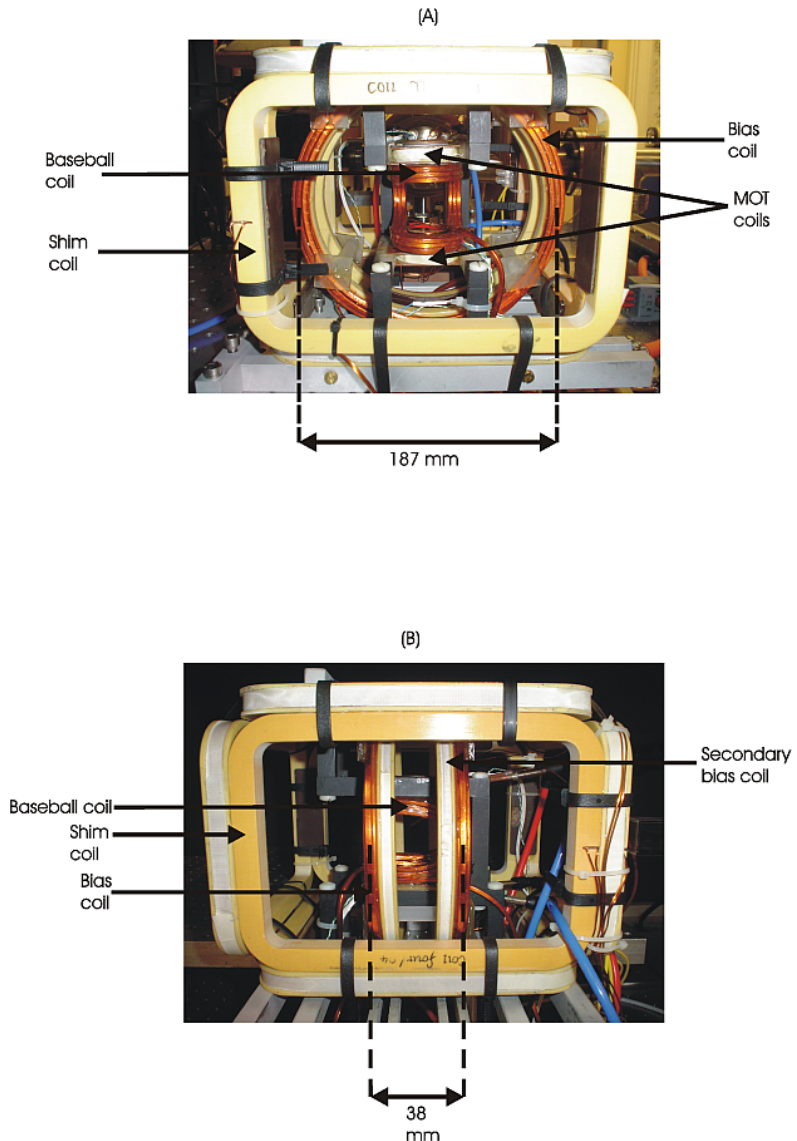


Figure 3.6: These two figures show the coils involved in our magnetic trap and where they are positioned. A is taken looking down the axis of the magnetic trap, while B is taken looking in perpendicular to the axis, along the direction in which the conventional absorption imaging beam propagates. Figure from Harsono (2006)

radial magnetic trap frequency  $\omega_r$  from its initial state to its final state: that is, the transition must be made adiabatically. The adiabatic condition can be stated as:

$$\frac{d\omega_r}{dt} \ll \omega_r^2 \quad (3.2)$$

By taking 5 seconds to ramp from  $\omega_r = 12.7 \times 2\pi$  to  $\omega_r = 167 \times 2\pi$ , a linear approximation suggests  $\frac{d\omega}{dt} = 193 \text{ sec}^{-2}$  whilst  $\omega_r^2 = 6400 \text{ sec}^{-2}$  satisfying the condition in equation 3.2 for the initial conditions and thus throughout the transition.

When initially loaded into the magnetic trap, our cloud is too large to be imaged by our absorption setup. We make our initial measurements of trapping by tracking how many of our atoms are recaptured by the MOT after some time held in the magnetic trap. We find that typically 60% of the atoms initially held in the MOT are still present after a 5 second hold in the magnetic trap. We also find that this number is unchanged when we ramp to the tight magnetic trap and back to the weak trap before measurement, which is an initial indication that we are ramping our magnetic traps adiabatically.

## 3.6 Evaporative Cooling

The principle of evaporative cooling is well known and its practice is widespread wherever there are drinks too hot to be palatable. Many textbooks consider the example of an ideal gas in a box to simplify the mathematics; as we are dealing instead with an anisotropic harmonic oscillator potential, this is at best an inexact analogy. Pethick and Smith (2002) give an equally simple illustration without a direct dependence on the trapping geometry, which I will follow here.

We consider a gas of  $N$  atoms at a mean energy  $\bar{\epsilon}$ . Suppose that we can remove all those atoms with energy greater than  $(1+x)\bar{\epsilon}$  and allow the gas to rethermalize - what will happen to the energy? We let  $dN$  represent the change in atom number

and  $d\bar{\epsilon}$  represent the change in mean energy - note that both quantities will be negative. Now we demand that energy is conserved, so the total energy after evaporation (right hand side) is equal to the total energy before less the energy carried away by the evaporated atoms:

$$\begin{aligned}
 N\bar{\epsilon} + (1+x)dN\bar{\epsilon} &= (N+dN)(\bar{\epsilon}+d\bar{\epsilon}) \\
 \frac{N+(1+x)dN}{N+dN} &= \frac{(\bar{\epsilon}+d\bar{\epsilon})}{\bar{\epsilon}} \\
 \frac{xdN}{N+dN} &= \frac{d\bar{\epsilon}}{\bar{\epsilon}} \\
 x &= \frac{d(\ln(\bar{\epsilon}))}{d(\ln(N))} \\
 \left(\frac{N}{N_0}\right)^x &= \frac{\bar{\epsilon}}{\bar{\epsilon}_0}
 \end{aligned} \tag{3.3}$$

In equation 3.3,  $N_0$  and  $\bar{\epsilon}_0$  represent the initial atom number and initial mean energy.

From equation 3.3 we can see that when only the most energetic particles are removed, the average energy of the gas can be reduced much faster than the atom number. (Note that this model describes a single evaporation; in practice, evaporation is carried out continuously.) In an ideal magnetic trap, then, the goal would be to make  $x$  as high as possible in order to maintain a large number of atoms during cooling. This is not a practical approach in real magnetic traps, as collisions with atoms in the background gas and inelastic collisions between atoms mean that lifetime in the trap is limited to some hundreds of seconds - real evaporation ramps are thus always a compromise between efficiency of cooling and time-dependent losses.

In order to maintain generality, we have so far avoided the question of how high-energy atoms are removed from the trap. In magnetic traps, this is usually accomplished by taking advantage of the position-dependent energy changes caused by the spatial variation of the B-field (which is approximately harmonic for cold

atoms near the center of a Ioffe trap). The most energetic atoms travel further from the center of the trap, and thus reach areas where the B-field and thus the splitting between  $m_F$  states is comparatively large. By applying radio-frequency radiation at these large frequencies, we induce transitions between trapped and untrapped states for only these energetic atoms, whilst the colder atoms are held at the center of the trap.

## 3.7 Imaging

During the MOT stage, we can monitor the number of trapped atoms non-destructively simply by using a photodiode to monitor the light scattered by the atoms in the trap. Once loaded into the magnetic trap, however, our primary tool for obtaining information about the cloud is imaging it on to an Andor CCD. We use two principal imaging schemes, each of which is described in more detail below: absorption imaging for large atom numbers and fluorescence imaging for small atom numbers.

### 3.7.1 Absorption imaging

When light with a frequency close to an atomic resonance passes through a cloud of atoms, some incident light will be absorbed. The rate of change in intensity with penetration into the cloud  $\frac{dI}{dz}$  will depend on the absorption cross-section  $\sigma_a$  of the atoms (which itself depends on the frequency of the incident light), the number density of atoms present  $n_a$  and the intensity of light incident on the atoms  $I$ . This leads to the differential equation:

$$\frac{dI}{dz} = -n_a I \sigma_a \quad (3.4)$$

Solving equation 3.4 we find Beer's law:

$$\ln \frac{I}{I_0} = - \int_0^z N_a \sigma_a dz \quad (3.5)$$

where  $I_0$  represents the intensity of the beam before it enters the atomic cloud,  $I$  represents the intensity after passing through the atomic cloud and  $z$  represents the thickness of the atomic cloud along the axis of the absorption beam. The integral on the right-hand side of 3.5 gives a quantity known as the optical depth: it represents the total number of atoms in the region of atoms which the beam passed through. In our absorption imaging setup we measure  $I$  and  $I_0$  and use them to calculate the optical depth of atoms which the beam has passed through: by ensuring that the cross-section of the absorption beam is much larger than that of the atomic cloud, we measure the total number of atoms in the cloud.

To apply this procedure in practice, we first release the atoms from the magnetic trap so that the density is reduced by free expansion. After a time of flight of order milliseconds and a brief period of repumping, we illuminate the atoms with a weak ( $I/I_{sat} \leq 0.1$ ) collimated beam of light resonant with the  $F=2$  to  $F'=3$  transition. Experimentally we use an exposure time of  $200 \mu\text{s}$ ; we observe approximately 400 counts per pixel from the beam, of which between thirty and fifty percent is typically absorbed by the beam. We then image the plane of the atoms on to the camera using an arrangement of lenses like that illustrated in figure 3.7. This image is recorded by the camera and sent to a PC for image analysis (henceforth this image will be referred to as  $Im_a$ ).

We then wait for 800 ms to allow the data from  $Im_a$  to be read out from the CCD. After this pause, we repeat the same sequence of illumination with the lasers but without any atoms; again we save the image recorded by the camera to a PC ( $Im_l$ ). We wait another 800 ms, and then record an image with the same exposure

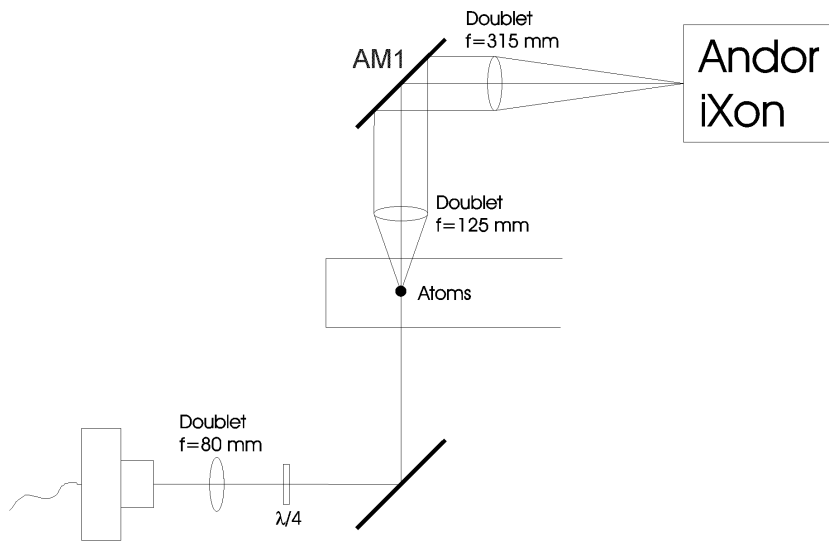


Figure 3.7: The optical arrangement for absorption imaging along the radial trap direction. The absorption beam is prepared on another optical table and brought to the MOT table using a polarization-preserving fibre. The output from the fibre is collimated using a doublet lens with focal length 80 mm. This collimated beam then passes through the atoms; a second doublet of focal length 125 mm is used to collimate the image of the atoms, then a final doublet of focal length 315 mm focuses the image of the atoms on to the CCD.

time as the previous two but without any light being introduced deliberately; this too is sent to the PC. ( $Im_b$ )

Let us consider the images recorded in reverse order for clarity.  $Im_b$  is simply the background light observed by the camera, perhaps due to a leak in one of the light shields: this image is subtracted from each of the others to remove any effect of contamination by this background.  $Im_l$  is principally made up of the image of the probe beam at full power, though it may also have some contribution arising from light scattered out of the other beams being used. If no atoms were present,  $Im_a$  would be identical to  $Im_l$ : if atoms are present when  $Im_a$  is taken, however, those atoms will absorb some of the probing light. We thus see a ‘shadow’ in the beam due to the atomic absorption, and by comparing  $Im_a$  to  $Im_l$  can determine the parameters of interest (e.g. phase space density, number density, etc) from the spatial distribution of absorption. A full discussion of how to derive these

parameters from images can be found in Ketterle *et al.* (1999).

### 3.7.2 Fluorescence imaging

The same principle used to track atom numbers in the MOT can be used for imaging - after the atoms are released from the magnetic trap, they are exposed to repumper light to move them into the  $F=2$  multiplet. The atoms are then briefly exposed to light resonant with the  $F=2$  to  $F'=3$  transition. The atoms excited to the  $F'=3$  state will decay back to the  $F=2$  state, emitting resonant photons isotropically. Using a high numerical aperture lens we gather some of these emitted photons and focus them on to the Andor camera with a second lens. This image is compared to an image taken with identical pulses of laser light but without atoms to correct for any light scattered out of the illuminating beam by the coils or other experimental apparatus. The optical setup used for this is illustrated in figure 3.8.

The signal strength obtained from fluorescence imaging is generally limited by the limited solid angle observed by the high numerical aperture lens: for large atom numbers this gives signals at least one and often two orders of magnitude smaller than for absorption imaging. When imaging a few hundred atoms or less, however, the expected absorption signal becomes comparable to the shot noise on the absorption beam (typically 14 counts per pixel) so fluorescence becomes the method of choice.

## 3.8 Bose-Einstein Condensation

Using and optimizing all of the techniques described above for our particular experimental conditions (see Harsono (2006)), we reliably obtain a Bose-Einstein condensate of approximately 400,000 atoms with a cycle time of approximately 3 minutes. We verify that we have achieved BEC by observing images of the cloud

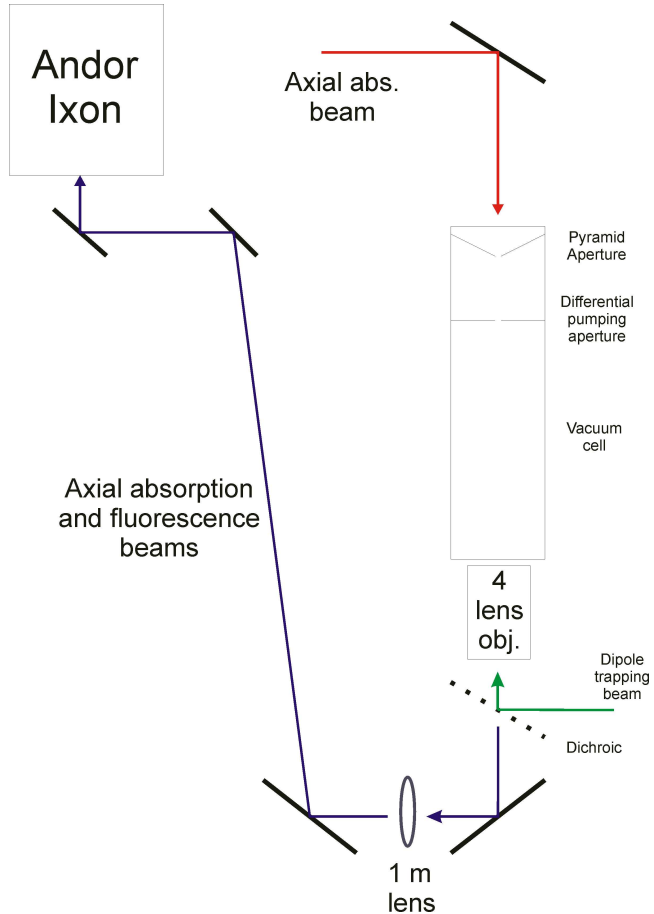


Figure 3.8: The optical setup for axial absorption and fluorescence imaging. This allows imaging along the axis of the magnetic trap, which will also form the axis for rotation. In both cases the 4-lens objective (see section 6.3.7) serves to collimate the image of the atoms while the 1 meter lens focuses this image on to the Andor.

approximately 20 ms after release from the magnetic trap and fitting to the density profile to determine the phase space density.

We see further confirmation of Bose-Einstein condensation by studying the way the cloud expands from the trap in time of flight. For a thermal cloud in an cylindrically symmetric trap, we expect the aspect ratio  $a_r$  to evolve with time-of-flight  $t$  as (Ketterle *et al.*, 1999):

$$a_r = \frac{\omega_r}{\omega_z} \sqrt{\frac{1 + \omega_z^2 t^2}{1 + \omega_r^2 t^2}} \quad (3.6)$$

By contrast, for a Bose-Einstein condensate the hydrodynamic pressure in the tight-trapping direction results in a much more rapid expansion in that direction than in the axial direction. For a trapping potential with  $\omega_r/\omega_z \gg 1$  Castin and Dum (1997) establish that the aspect ratio should evolve as:

$$a_r = \epsilon^{-1} \frac{1 + \epsilon^2 (\tau \tan^{-1} \tau - \ln \sqrt{1 + \tau^2})}{\sqrt{1 + \tau^2}} \quad (3.7)$$

to second order in  $\epsilon$ , where  $\tau = \omega_r t$  and  $\epsilon = \omega_z/\omega_r$ .

Both of these theoretical predictions are plotted in figure 3.9 for long times of flight (short times of flight are neglected because saturation makes it difficult to fit well and the difference is in any case less marked). Also plotted in the figure are experimental data taken at a range of times of flight for two different clouds; one is evaporated to 0.85 MHz, approximately 250 kHz above the trap bottom, while the second is evaporated to only 30 kHz above the trap bottom at 0.63 MHz. We can see that the cloud evaporated to 0.63 MHz is a good fit to the theoretical prediction for BEC.

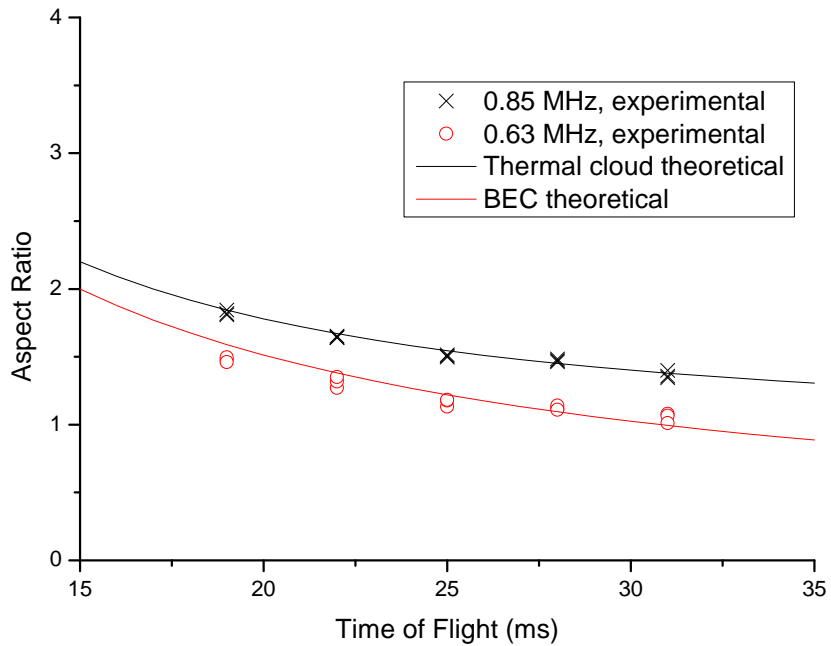


Figure 3.9: This figure shows the development of aspect ratio with time for two clouds, one evaporated to 0.85 MHz and one evaporated down to 0.63 MHz. Note that three points are plotted for each cloud at each time of flight. Also plotted are the theoretical predictions for aspect ratio against time for a thermal cloud and for a Bose-Einstein condensate. When the cloud is evaporated to 0.63 MHz it is clearly following the prediction for a Bose-Einstein condensate. The figure is confined to long times of flight as for short times of flight the difference is less marked and saturation makes accurate fitting difficult.

## 3.9 Seeing things in a new light: Axial Absorption Imaging

The setup discussed in section 3.7.1 is a typical absorption arrangement, and is what we use for our diagnostics and in the initial search for Bose-Einstein condensation. However, the imaging axis of this setup is perpendicular to the axis of the magnetic trap and of the lattice system. For alignment of the lattice system, it is significantly more helpful to image along the axis, so when we decided to implement the lattice system we also decided to add a second absorption beam. In this section I will discuss the implementation of this system and the issues to be overcome.

### 3.9.1 Mechanical implementation

With the rest of the experiment complete and in place, the optical access to the magnetic trap is quite limited: the axial direction is particularly restricted, as the 4-lens objective occupies the whole of one side while the vacuum system and pyramid MOT occupy the other. The only way that light can be sent to the atoms in the axial direction is to pass it through the narrow slit (approximately 1 mm wide and 2 mm tall) in the apex of pyramid MOT.

The most straightforward way of passing a beam through the pyramid slit would have been to send the probe light through the pyramid fibre: this was impractical, however, as between the pyramid cooling and repumping light there are already two orthogonal polarizations in that beam. If any further beams were added, it would thus have to be done with non-polarizing beam-splitters and would result in a loss of approximately 50% in transmitted power. Such a scheme would also be awkward in terms of beam path, as the pyramid fibre and the probe beam are on opposite sides of the optical table without a clear path between them.

Given these issues, a second fibre was installed to transmit the probing light to the pyramid end of the MOT table. I used a single mode polarization-preserving fibre which had been purchased for earlier experiments in the group: in testing we achieved approximately 60% transmission through this fibre with stable polarization and an output beam diameter of 2.4 mm. This new fibre's output mount was installed next to and parallel to the pyramid fibre output.

The use of a second fibre presents two further complications. Firstly, the optical pumping light comes from applying a different detuning to the probe beam and thus comes from the same fibre. In order to apply optical pumping after the molasses stage we need the optical pumping/probe (OP/Probe) light passing through the conventional absorption fibre, while to use axial absorption imaging we need the OP/Probe light to pass through the axial absorption fibre. It was thus necessary to find a way to redirect the light from one fibre to the other while the experiment is running. Secondly, as the pyramid beam is already aligned on to the slit the axial probe beam needed to be introduced into the pyramid optics: whatever means used to do this could not block or reduce the pyramid power during loading.

Both of these issues were resolved by using flipping mirror mounts controlled by a voltage output (RD-KLS-1", from Radiant Dyes GmbH). When the voltage input to these mounts changes state, an actuator raises or lowers them by 90 degrees over approximately 1.5 seconds. The manufacturer's test showed that the flipping produces a beam alignment stable to less than  $10^{-4}$  radians. We performed our own test by repeatedly flipping the mirror up and down and measuring the position of the dipole trapping beam using the position sensitive photodiode approximately 1 m away. Taking the standard deviation of 84 position readings taken over 15 minutes gives a standard deviation of approximately  $2 * 10^{-5}$  radians.

One of these mirrors was installed immediately before the entrance to the conventional probe fibre, deflecting the beam on to the axial fibre. This is illustrated

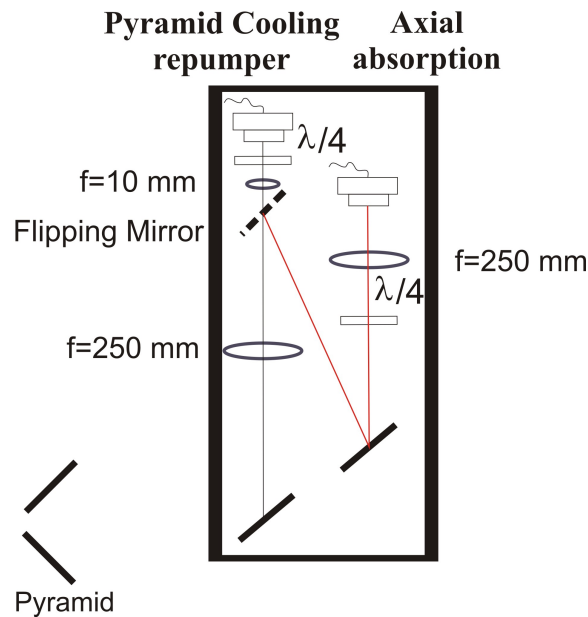


Figure 3.10: This figure shows a detailed view of the pyramid and axial absorption optics just before the pyramid MOT. The dashed line indicates where an RD-KLS-1" flipping mirror is installed: this mirror is down for loading and is flipped to upright during evaporation.

and labelled in figure 3.2 earlier in this chapter. The second flip mirror was installed immediately after the 10 mm lens in the pyramid telescope: this is illustrated on figure 3.10. This positioning ensures that the pyramid beam is as small as possible when passing over the flip mirror in order to eliminate clipping. Both mirrors are left in the ‘down’ position normally: when we want to run the experiment with axial absorption imaging we move the mirrors upright during evaporative cooling. The same absorption imaging sequence is used as for conventional absorption imaging.

### 3.9.2 Axial beam profile

With the mechanical arrangements for absorption imaging complete, we moved on to consider how to handle the beam. There were two sensible approaches: either to use a collimated beam and accept that some of the beam will be clipped on the

edges of the pyramid slit or to focus the beam into the pyramid slit to maximize power through the slit. In either case, in order to use conventional absorption imaging techniques we needed to ensure that the intensity of the absorption beam at the atoms was much less than the saturation intensity of the imaging transition ( $I_{sat} = 1.667 \text{ mW cm}^{-2}$  for circularly polarized light in  $^{87}\text{Rb}$ ). In our conventional absorption setup we use  $\frac{I}{I_{sat}} = 0.1$ , so this was the benchmark used for low intensity.

Given where the flip mirror is positioned, the axial absorption beam certainly had to pass through the 25 cm lens which forms the second half of the pyramid telescope. Thus the most straightforward approach was to use this lens either to focus the beam or as the second half of a 1:1 telescope for the axial probe beam.

The propagation of the beam through the system for both of these methods was modeled using the more intuitive version of ray matrix propagation outlined in Self (1983): in this method we regard the waist of the incoming outgoing beam as the object and the waist of the outgoing beam as the image and use formulae analogous to geometric optics to transform them. These formula are:

$$\frac{1}{f} = \frac{1}{u + z_R(u - f)^{-1}} + \frac{1}{v} \quad (3.8)$$

$$M = \left( \sqrt{\left(1 - \frac{s}{f}\right)^2 + \left(\frac{z_R}{f}\right)} \right)^{-1} \quad (3.9)$$

where  $u$  indicates the distance to the incoming beam waist,  $v$  the distance from the lens to the outgoing beam waist,  $z_R$  the Rayleigh range,  $f$  the focal length of the lens and  $M$  the magnification of the transformation.

Using this model and applying the constraint that the intensity at the atoms should be equal to  $0.1I_{sat}$  showed that in either approach we would predict approximately 500 counts per pixel in our usual exposure time of 200  $\mu\text{s}$ . The 25 cm lens already built into the pyramid setup was approximately 40 cm away from the pyramid slit: thus the beam passing through the slit would be almost the same

size as if it had been collimated. Given this, a 1:1 telescope was used to produce a collimated axial absorption beam with a waist on the order of 1 mm.

### 3.9.3 Axial Absorption Magnification

The axial absorption beam is imaged by a telescope consisting of the 4-lens objective (with focal length  $f_1$  mm) and a doublet lens with focal length  $f_2 = 1000$  mm. The 4-lens objective has been simulated to have a focal length of 37 mm: thus for an ideal system the magnification in axial imaging would be  $f_2/f_1 = 27.0$ . As the four-lens objective was assembled manually, however, its focal length should be verified experimentally.

This was accomplished by taking a series of pictures of a cloud falling under gravity at different times of flight: we measure the z-center of each cloud and plot these against time of flight. As the size of the pixels on the camera and  $g$  are known, the magnification of the imaging system is determined by fitting the cloud's z-position  $z$  with time of flight  $t$  to:

$$z = z_0 + \frac{g}{2} M t^2$$

where  $z_0$  is the initial position of the cloud on the camera,  $g$  is the acceleration due to gravity and  $M$  is the magnification of the imaging system.  $M$  and  $z_0$  are left as free parameters. Such a data set and fit are illustrated in figure 3.11. From these data, we measure a magnification of 24.7(2): if all other components of the system were ideal, this would imply a focal length of 40.5(3) mm for the four-lens objective.

The possibility that the lens is simply not focussed on to the magnetic trap is neglected because a single beam sent through the four-lens objective produces trapping at a position which may be varied along the z-direction by moving the

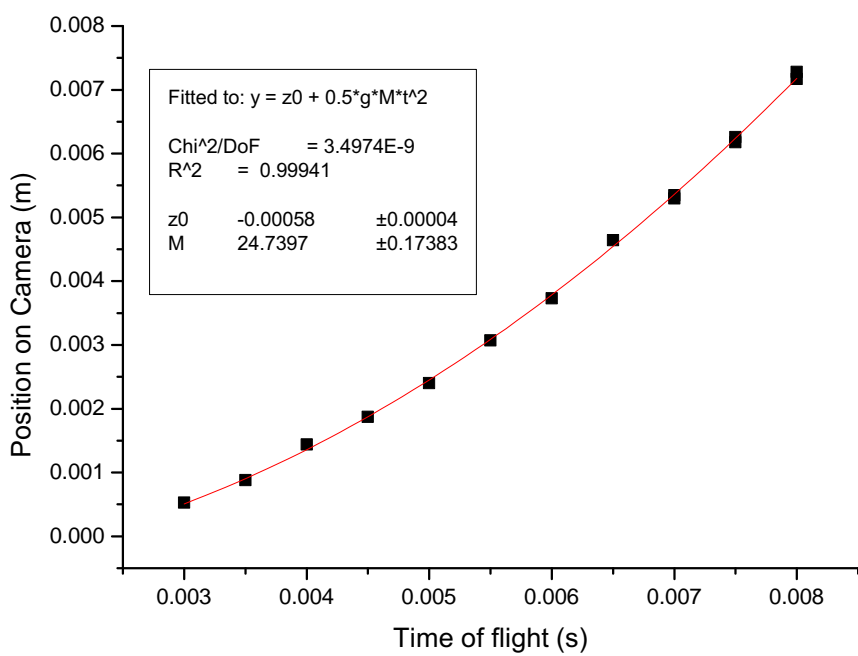


Figure 3.11: This figure shows our measurement of the magnification of the axial absorption imaging system as discussed in the text.

four-lens objective axially. The position of the four-lens objective has been set so as to fix this dipole trapping at the center of the magnetic trap.

### 3.9.4 Remaining Issues

As a new addition to the experiment, the axial absorption system is still rough around the edges. In this section, I will outline a few of the areas in which we would like to improve the system and the thoughts we have on how such improvements could be made.

The first issue is one of quantitative reliability: in short times of flight there is a small fixed field perpendicular to the axis of propagation of the probe beam. Thus the quantization field is not coaxial with the probe beam and we cannot assume that the atomic population will be optically pumped into the 'stretched'  $F = 2, m_F = 2$  to  $F' = 3, m'_F = 3$  transition: this prevents the analytical solution discussed by Steck (2003) for resonance fluorescence. This makes the absolute calibration of our imaging uncertain.

As an additional complication to the problems with the quantization axis, the small length scales we are forced to operate on along the axial direction the probe beam intensity is higher than can be accounted for in the low-intensity picture of absorption imaging. When we apply a probe beam at low intensity ( $I < 0.5I_{sat}$ ) we cannot detect any photons reliably, even if the signal from the camera is boosted before read-out. We are looking into addressing the issue of intensity by implementing the scheme for high-intensity absorption imaging described by Reinaudi *et al.* (2007).

If further work can successfully implement a high-intensity absorption imaging scheme, this will help with the final problem we have encountered with axial absorption imaging: saturation. As we are imaging along the axis of the trap rather than across, we often observe total absorption of the probe beam. Normally this

can be addressed by increasing the time of flight but given the narrow aperture for axial absorption light and the high magnification of the imaging system it is time-consuming to change the field of view. Aligning on long times of flight also precludes direct observation of lattice trapped atoms in axial absorption.

## CHAPTER 4

---

# Dipole Trapping and Optical Lattices

Optical forces were vital to the second observation of BEC (Davis *et al.*, 1995) and to the observation of interference between two BECs in the same group. (Andrews *et al.*, 1997) As the field has developed, the flexibility of potential depth, phase and shape which these technologies allow have kept them at the center of advances in the field of ultracold atoms. Amongst other applications, they have been key to the observation of sub-Poissonian atom number statistics (Chuu *et al.*, 2005), to the first steps towards a neutral atom quantum register (Schrader *et al.*, 2004) and to the observation of the Berezinskii-Kosterlitz-Thouless transition by Hadzibabic *et al.* (2006).

In this chapter, I shall briefly review the theory underlying the interaction of light fields with ultracold atoms and Bose-Einstein condensates. In preparing this chapter I have referred extensively to Loudon (1983), Scully and Zubairy (1997) and to review articles by Grimm *et al.* (2000) on dipole trapping in general and by Morsch and Oberthaler (2006) on the dynamics of condensates in optical lattices.

## 4.1 The Dipole Potential

The concept of the dipole potential is easily understood: if we consider an atom placed into an electrical field, it is clear that the atomic electron cloud will move in response to the field. This produces a net offset between the centres of charge for the nucleus and the electron cloud and thus the atoms acquire an electric dipole moment. The dipole potential arises from the energy of interaction between the dipole moment and the field which induced it.

In order to understand the dipole potential in a more quantitative way, we consider the interaction of an atom with an electric field  $E$  which is a function of position ( $r$ ) and time  $t$  with frequency  $\omega$  of the form:

$$\mathbf{E}(\omega, \mathbf{r}, t) = \hat{\mathbf{e}}_0 \frac{E(\mathbf{r})}{2} (e^{-i(kz - \omega t)} + e^{i(kz - \omega t)}) \quad (4.1)$$

where  $\hat{\mathbf{e}}_0$  is a unit vector in the direction of the polarization of the field,  $k = \frac{2\pi}{\lambda}$  where  $\lambda$  is the wavelength of the electromagnetic wave and  $i$  is the imaginary number. The complex atomic polarizability  $\alpha(\omega)$  gives the relationship between this field and the dipole moment induced in an atom by it,  $\mathbf{p}$ :

$$\mathbf{p}(\mathbf{r}, \omega, t) = \alpha(\omega) \mathbf{E}(\mathbf{r}, t)$$

If  $\alpha$  is known, then the dipole potential is simply given from the usual interaction energy between a dipole and a field:

$$\begin{aligned} U_{\text{dip}} &= \frac{-1}{2} \langle \mathbf{p} \cdot \mathbf{E} \rangle \\ &= \frac{-1}{2\epsilon_0 c} \text{Re}(\alpha) I \end{aligned} \quad (4.2)$$

Here the intensity  $I = (|E|^2 \epsilon_0 c)/2$  and angled brackets indicate a time-average

over rapidly oscillating terms. It remains to determine  $\alpha$ .

### 4.1.1 Classical Picture

Classically, we consider a system with one electron (with mass  $m_e$  and charge  $e$ ) bound to the nucleus with a spring such that its oscillation frequency is equal to the transition frequency  $\omega_0$ , driven by the light field at some frequency  $\omega$ . The acceleration of the electron will emit radiation, resulting in a loss of energy known as the Larmor damping (the term shown in equation 4.3) and leading to the Lorentz model of equation 4.4.

$$\Gamma_\omega = \frac{e^2 \omega^2}{6\pi\epsilon_0 m_e c^3} \quad (4.3)$$

$$\frac{-eE(t)}{m_e} = \ddot{x} + \Gamma_\omega \dot{x} + \omega_0^2 x \quad (4.4)$$

where  $x$  is the displacement of the electron from the atom in one dimension and  $\epsilon_0$  is the permittivity of free space.

Semi-classically, we can find a value for  $\alpha$  which is sufficiently accurate for our purpose by replacing the Larmor damping term in the Lorentz model with the quantum-mechanically determined natural linewidth of the transition given in equation 4.5. Doing so and solving equation 4.4 gives equation 4.6:

$$\Gamma = \frac{\omega_0^2}{\omega^2} \frac{2J+1}{2J'+1} \Gamma_\omega \quad (4.5)$$

$$\alpha = 6\pi\epsilon_0 c^3 \frac{\Gamma/\omega_0^2}{\omega_0^2 - \omega^2 - i(\omega^3/\omega_0^2)\Gamma} \quad (4.6)$$

where  $J$  is the total angular momentum quantum number of the ground state and  $J'$  is the total angular momentum quantum number of the excited state. For dipole trapping, we are generally working in a regime where  $\omega_0 \gg \omega_0 - \omega \gg \Gamma$ : this allows us to neglect the imaginary portion of the denominator of equation 4.6

when calculating  $U_{dip}$ , to neglect the resonance at  $\omega = -\omega_0$  and to treat  $\frac{\omega}{\omega_0} \approx 1$ . This gives us a simple expression for  $U_{dip}$ :

$$U_{\text{dip}} = \frac{3\pi c^2}{2\omega_0^3} \left( \frac{\Gamma}{\Delta} \right) I \quad (4.7)$$

### 4.1.2 Quantum Derivation

A purely quantum-mechanical treatment of polarizability is straightforward for the case of a two-level atom. Let the wavefunctions for the two atomic states in the absence of a field be given by:

$$\Psi_{1,2}(r, t) = e^{\frac{-iE_{1,2}t}{\hbar}} \psi_{1,2}(r)$$

$\Psi_{1,2}$  are by definition solutions of the Schrödinger equation for the free atom Hamiltonian  $\mathcal{H}_0$ , and  $E_2 - E_1 = \hbar\omega_0$ .

We now consider the response of this system when it is exposed to an oscillating field of the form of equation 4.1. For the cases of practical interest, the wavelength of the electric field is orders of magnitude greater than the scale of the atomic wavefunctions, so we take the magnitude of the E-field at the atoms to depend only on time:

$$\mathbf{E}(t) = \mathbf{E}_0 \cos(\omega t) = \frac{\mathbf{E}_0}{2} (e^{-i\omega t} + e^{i\omega t})$$

Here  $\mathbf{E}_0$  is a vector giving the maximum amplitude and the direction of the electric field at the atoms. The interaction Hamiltonian  $\mathcal{H}_d$  is then given by:

$$\begin{aligned} \hat{\mathcal{H}}_d &= \mathbf{d} \cdot \mathbf{E} \\ &= \mathbf{d} \cdot \mathbf{E}_0 \left( \frac{e^{-i\omega t} + e^{i\omega t}}{2} \right) \end{aligned} \quad (4.8)$$

where  $\mathbf{d} = e \sum_{i=1}^Z \mathbf{r}_i$ , where  $i$  runs over all the atomic electrons.

Once exposed to a time-dependent potential, the states  $\Psi_{1,2}$  are no longer eigenstates. Instead, the wavefunction  $\Psi$  will be a linear superposition of the two stationary state solutions for the zero-field case:

$$\Psi(\mathbf{r}, t) = C_1(t)\Psi_1(\mathbf{r}, t) + C_2(t)\Psi_2(\mathbf{r}, t) \quad (4.9)$$

Here  $C_1$  and  $C_2$  are complex and normalization of  $\Psi$  demands that  $|C_1|^2 + |C_2|^2 = 1$ . If we use this wavefunction in the Schrödinger equation, we can obtain differential equations for  $C_1$  and  $C_2$ ; it is more usual to re-express these differential equations in terms of the density matrix elements  $\rho_{ij} = C_i C_j^*$  and to introduce a phenomenological decay term to account for spontaneous decay. We also rewrite:

$$\begin{aligned} \frac{e}{\hbar} \int \psi_1^* \mathbf{D} \cdot \mathbf{E}_0 \psi_2 d\tau &= \nu \\ \bar{\rho}_{12} &= \rho_{12} e^{i(\omega_0 - \omega)t} \\ \bar{\rho}_{21} &= \rho_{21} e^{-i(\omega_0 - \omega)t} \end{aligned}$$

where  $d\tau$  indicates a volume integral over the system and  $\mathbf{D} = \frac{d}{e}$ . After these modifications, the differential equations for  $C_1$  and  $C_2$  become the optical Bloch equations:

$$\begin{aligned} \frac{d\rho_{22}}{dt} &= -\frac{d\rho_{11}}{dt} \\ &= \frac{-i\nu^*}{2} \bar{\rho}_{12} + \frac{i\nu}{2} \bar{\rho}_{21} - \Gamma \rho_{22} \end{aligned} \quad (4.10)$$

$$\begin{aligned} \frac{d\bar{\rho}_{12}}{dt} &= \frac{d\bar{\rho}_{21}^*}{dt} \\ &= \frac{i\nu}{2} (\rho_{11} - \rho_{22}) - \frac{\Gamma}{2} \bar{\rho}_{12} + i(\omega_0 - \omega) \bar{\rho}_{12} \end{aligned} \quad (4.11)$$

We can solve these equations for the steady state by setting equation 4.10, equation 4.11 and the complex conjugate of equation 4.11 all to zero and by using

normalization to eliminate  $\rho_{11}$ . This gives:

$$\rho_{22} = \frac{1}{4} \frac{|\nu|^2}{(\omega_0 - \omega)^2 + \frac{\Gamma^2}{4} + \frac{1}{2}|\nu|^2} \quad (4.12)$$

$$\rho_{12} = \frac{-e^{-i(\omega_0 - \omega)t}}{2} \frac{\nu(\omega_0 - \omega - i\frac{\Gamma}{2})}{(\omega_0 - \omega)^2 + \frac{\Gamma^2}{4} + \frac{1}{2}|\nu|^2} \quad (4.13)$$

The dipole moment  $d$  can then be determined from the wavefunction  $\Psi$ :

$$\begin{aligned} \mathbf{d}(t) &= -\langle \Psi | e \sum_{i=1}^Z \mathbf{r}_i | \Psi \rangle \\ &= -e \int (\rho_{21} e^{-i\omega_0 t} \psi_1^* \hat{\mathbf{d}} \psi_2 + \rho_{12} \psi_2^* \hat{\mathbf{d}} \psi_1 e^{i\omega_0 t}) d\tau \\ &= -e (\rho_{21} e^{-i\omega_0 t} \mathbf{D}_{12} + \rho_{12} e^{i\omega_0 t} \mathbf{D}_{21}) \end{aligned} \quad (4.14)$$

The polarizability is defined as  $\mathbf{d}(t) \cdot \mathbf{e}_0 = \frac{1}{2} * E_0 (\alpha(\omega) e^{-i\omega t} + \alpha(-\omega) e^{i\omega t})$ , where  $\mathbf{e}_0$  is the unit vector in the direction of polarization. Re-expressing the constants and matrix elements in terms of the quantum mechanical natural linewidth  $\Gamma$  we obtain:

$$\alpha(\omega) = \frac{3\pi\epsilon_0 c^3}{\omega_0^3} a^2 \Gamma \left( \frac{\Delta + \frac{i\Gamma}{2}}{\Delta^2 + \frac{\Gamma^2}{4} + \frac{|\nu|^2}{2}} \right) \quad (4.15)$$

where  $a$  is a factor of order unity representing the projection of the atomic dipole moment along the polarization direction. Substituting equation 4.15 into equation 4.2 we obtain:

$$\begin{aligned} U_{dip} &= \frac{-1}{2\epsilon_0 c} \text{Re}(\alpha) I \\ &= -\frac{3\pi c^2}{2\omega_0^3} a^2 \Gamma \left( \frac{\Delta}{\Delta^2 + \frac{\Gamma^2}{4} + \frac{|\nu|^2}{2}} \right) I \end{aligned} \quad (4.16)$$

$$(4.17)$$

where:

$$|\nu|^2 = \frac{3\pi\epsilon_0 c^3}{\hbar\omega_0^3} E_0^2 \Gamma \quad (4.18)$$

This reduces to equation 4.7 for the intensities under 300 MW cm<sup>-2</sup> and  $\omega_0 \gg \Delta \gg \Gamma$ . For comparison, in our experiment we typically work with a range of intensities from 5 W cm<sup>-2</sup> to 1 kW cm<sup>-2</sup>.

### 4.1.3 Choosing trap detuning

Consider again the dipole potential (equation 4.7) in which:

$$U_{\text{dip}} \propto \left(\frac{I}{\Delta}\right)$$

The first point to note about equation 4.7 is that the sign of the dipole potential depends on the sign of  $\Delta = \omega - \omega_0$ . The blue-detuned regime where  $\omega > \omega_0$  leads to a repulsive potential: atoms are repelled from the intensity maxima of the laser beam. Conversely, in the red-detuned regime ( $\omega < \omega_0$ ) atoms are attracted to intensity maxima.

Blue-detuned dipole traps have two major advantages: they can generally achieve tighter trapping frequencies than red-detuned traps and as the atoms are trapped in a minimum of the light field, heating by off-resonant scattering is significantly lower than in an equivalent red-detuned trap. Despite these advantages red-detuned traps remain widely used, in part because of their experimental convenience: as we will see below, a red-detuned beam can trap atoms simply by being focussed.

We decided to use a red-detuned trap largely for reasons of experimental convenience: the scheme which we will discuss in chapter 6 would be just as effective with blue-detuned light. One then has to settle on a particular wavelength to use.

In choosing a wavelength, it is worth considering the rate at which we would expect an atom to scatter photons from the dipole trapping beam  $R_{sc}$ . This can also be found from the polarizability:

$$R_{sc} = \frac{1}{\hbar\epsilon_0 c} \text{Im}(\alpha) \quad (4.19)$$

$$= \frac{3\pi c^2}{2\hbar\omega_0^3} \left( \frac{\Gamma}{\Delta} \right)^2 I \quad (4.20)$$

We see that the scattering rate scales with  $\Delta^{-2}$  while the trapping potential scales with  $\Delta^{-1}$ : thus an increase in detuning will cause a larger drop in scattering rate than the decrease in trapping potential. For our experiments, we choose to operate at 830 nm: at this wavelength we expect one in one hundred atoms to scatter a photon in a second. 830 nm has the additional practical advantage that it is a standard wavelength for commercial optics.

#### 4.1.4 Focussed Beam as a Dipole Trap

As mentioned above, with a red-detuned trapping beam atoms can be trapped simply by focussing a Gaussian beam. As such focussed Gaussian beams are the starting point for the lattice setup which will be described in chapter 6 this section outlines the theoretical properties of such a trap.

For a Gaussian beam, the intensity profile of the beam is:

$$I(r, z) = \frac{2P}{\pi w_0^2} \frac{w_0^2}{(w(z))^2} e^{\frac{-2r^2}{(w(z))^2}} \quad (4.21)$$

where  $r$  is the distance from the axis of the beam,  $P$  is the power of the trapping beam,  $\lambda$  its wavelength and

$$w(z) = w_0 \sqrt{1 + \left( \frac{z}{z_r} \right)^2} \quad (4.22)$$

$$z_r = \frac{\pi w_0^2}{\lambda} \quad (4.23)$$

In equation 4.22,  $w(z)$  gives the waist size of the beam at a distance  $z$  from the minimum waist size  $w_0$ .  $z_R$  defined in equation 4.23 gives the characteristic distance of the waist's expansion, known as the Rayleigh range.

Consider the beam at its focus, where  $w(z) = w_0$ . Using equation 4.7 to relate the trapping potential to the intensity, where  $r$  is small relative to  $w$  we can expand the exponential in equation 4.21 about  $r = 0$  to obtain a harmonic approximation to the trapping potential with trapping frequency  $\omega_{\text{gauss,r}}$ :

$$U_{\text{gauss,r}} = U_0 \left( 1 - \frac{2r^2}{w_0^2} \right) \quad (4.24)$$

$$\begin{aligned} U_0 &= \frac{3\pi c^2}{2\omega_0^3} \left( \frac{\Gamma}{\Delta} \right) \frac{2P}{\pi w_0^2} \\ \omega_{\text{gauss,r}} &= \sqrt{\frac{4U_0}{mw_0^2}} \end{aligned} \quad (4.25)$$

With a similar Maclaurin expansion of the  $(w(z))^{-1}$  factor for  $r = 0$ , we can obtain the axial trapping frequency  $\omega_{\text{gauss,a}}$ :

$$\omega_{\text{gauss,a}} = \left( \frac{2U_0}{mz_r^2} \right)^{0.5} \quad (4.26)$$

For the experiments in which we directly image atoms trapped in the lattice we generally work with 0.5 mW of power in a beam with a waist of 80 microns. For these conditions, the profile of the Gaussian beam gives an envelope with a trap depth of approximately 28 nK, radial trap frequency of approximately 7 Hz and negligible axial confinement.

## 4.2 Optical Lattices

A common technique to achieve smaller length scales with red-detuned light or to create a trap with blue-detuned light is to overlap two coherent beams and use the maxima or minima of the intensity of the resulting interference pattern to form a trapping potential: such periodic trapping potentials are known as optical lattices.

The simplest arrangement is to retro-reflect a single beam to create a potential of the form

$$U_{\text{retro}} = 4U_0 \cos^2\left(\frac{\pi x}{d}\right)$$

where  $U_0$  indicates the potential depth for a dipole trap formed by a single beam, and the  $x$ -axis is defined as being parallel to the direction of propagation of the laser forming the lattice. The factor of 4 arises because the overlapping coherent beams double the maximum amplitude of the E-field and thus quadruple the intensity. The lattice periodicity is  $d = \lambda/2$ : by writing the potential in this fashion the extension to non-counterpropagating beams becomes more straightforward.

Following a similar method to section 4.1.4, we make a harmonic approximation to the potential at each lattice site in order to estimate the trapping frequency for the individual lattice sites:

$$\omega_{\text{1D lat}} = \frac{\pi}{d} \sqrt{\frac{8U_0}{m}}$$

## 4.3 BEC in an optical lattice

In recent years, much attention has been focussed on the behavior of ultracold gases loaded into optical lattices (see, for example, Greiner *et al.* (2002)). Where these lattices are weak - with potential depth much less than the chemical potential - and have periods greater than the characteristic length for density changes in the condensate (called the healing length) they can simply be treated as part of the

trapping potential in the Gross-Pitaevskii equation.

Potentials which vary faster than the healing length of the condensate but without periodicity can produce interesting effects and phases of matter including Anderson localization and Bose glasses. These are beyond the scope of the current work and so will not be discussed further, but the interested reader may wish to consult Clément *et al.* (2005).

In periodic potentials which have a depth comparable to or greater than the chemical potential, it is no longer sufficient to regard all the atoms as being in the same state; some will be localized in one lattice site, some in another. A different approach is needed which both describes the localization of atoms at high lattice strengths and reduces to the Gross-Pitaevskii equation in the limit of no lattice potential. Jaksch *et al.* (1998) demonstrates how this model may be constructed by calculating the Bloch eigenstates of the periodic lattice: these can be used to construct the Wannier functions, a complete orthogonal set of wavefunctions localized at individual lattice sites. By expanding  $\psi$  in terms of the Wannier functions in equation 2.22, one obtains the following Hamiltonian:

$$H_{full} = - \sum_{i,j} J_{ij} a_i^\dagger a_j + \frac{1}{2} \sum_{i,j,k,l} U_{ijkl} a_i^\dagger a_j^\dagger a_k a_l + \sum_i (\epsilon_i - \mu) a_i^\dagger a_i \quad (4.27)$$

In this Hamiltonian,  $a_i$  is the destruction operator for a particle localized at the  $i$ th lattice site, with position  $\mathbf{x}_i$ .  $\epsilon_i$  represents the potential energy of an atom due to the slowly varying trapping potential  $V_T$ , and  $\mu$  is the chemical potential as usual.

The first term of the Hamiltonian in equation 4.27 represents the probability of tunnelling, with a particle created at site  $i$  and destroyed at site  $j$ . The coefficient  $J_{ij}$  represents the matrix element for this process, expressed as:

$$J_{ij} = - \int d\mathbf{x} w_0(\mathbf{x} - \mathbf{x}_i) \left( \frac{\mathbf{p}^2}{2m} + V_0(\mathbf{x}) + V_t(\mathbf{x}) \right) w_0(\mathbf{x} - \mathbf{x}_i) \quad (4.28)$$

Here  $w_0(\mathbf{x} - \mathbf{x}_i)$  is the Wannier function for an atom in the lowest Bloch band, localized at  $\mathbf{x}_i$ ,  $V_0$  represents the optical potential and  $V_T$  represents the slowly varying trapping potential. For an optical lattice potential with potential depth greater than five recoil energies, calculations show (Jaksch *et al.*, 1998) that the matrix element for nearest neighbor tunnelling  $J_{01}$  is an order of magnitude larger than other tunnelling coefficients, so we can neglect all but the nearest-neighbor tunnelling.

The second term in the Hamiltonian describes interactions between atoms at sites  $i, j, k$  and  $l$ .  $U_{ijkl}$  is again the matrix element for this process, given by:

$$U_{ijkl} = U_{sc} \int d\mathbf{x} w_0(\mathbf{x} - \mathbf{x}_i)w_0(\mathbf{x} - \mathbf{x}_j)w_0(\mathbf{x} - \mathbf{x}_k)w_0(\mathbf{x} - \mathbf{x}_l) \quad (4.29)$$

where  $U_{sc} = \frac{4\pi a_s \hbar^2}{m}$  as in equation 2.17. In Jaksch *et al.* (1998) we find that the matrix elements representing interactions between atoms at one site and its nearest neighbor (where at least one of  $i, j, k$  and  $l$  is set equal to one) are an order of magnitude smaller than the on-site interaction  $U_{0000}$ , so we consider only the latter.

By restricting our attention to on-site interactions and tunnelling only between nearest neighbors, we obtain the Bose-Hubbard Hamiltonian from equation 4.27:

$$H_{BH} = -J \sum_{\langle i,j \rangle} a_i^\dagger a_j + \frac{U}{2} \sum_i a_i^\dagger a_i^\dagger a_i a_i + \sum_i (\epsilon_i - \mu) a_i^\dagger a_i \quad (4.30)$$

where the sum over  $\langle i, j \rangle$  indicates a sum over all unique pairs of sites,  $U = U_{0000}$  and  $J = J_{01}$ .

The behavior of a Bose-Hubbard model has been extensively studied in relation to theoretical condensed matter physics, and previous experimental implementations include arrays of Josephson junctions and thin granular films (for an example of work involving lattices of Josephson junctions see Geerligs *et al.* (1989)). Using optical lattices and ultracold gases offers some advantage to investigations of the

model, as once the initial setup is complete such an experiment can access a wide range of parameter values with relatively painless adjustments to laser power or alignment.

A key feature of the Bose-Hubbard model in three dimensions is the Mott insulator transition: this is a quantum phase transition between the superfluid stage (in which atoms flow freely throughout the lattice) and the insulating stage (where atoms are localized in lattice sites). First observed by Greiner *et al.* (2002), this transition serves as the basis for some proposals for creating single-atom qubits in ultracold neutral atoms. (Scheunemann *et al.*, 2000)

## CHAPTER 5

---

# Direct Digital Synthesis for High Precision Frequency Synthesis

Radio frequency generation and manipulation is a mature discipline; the acousto-optic deflector discussed in section 6.2.1 allows us to bring the flexibility of RF technology to bear on generation and rotation of an optical lattice. In this chapter I will discuss the options available for generating radio frequency signals in general and then outline the considerations which determined our requirements. Considering these requirements led us to the conclusion that direct digital synthesis was the most suitable option; I shall give a more detailed description of the operation of a DDS before finally describing the practical details of the system we have developed and the software which controls it.

### 5.1 Experimental Requirements

The design requirements for our RF system were determined by our initial goal: reaching the conditions for the Mott insulator transition in an array of focussed

dipole trapping spots. In this arrangement, the atoms were trapped in a single focussed beam; we controlled the position of each beam in the imaging plane by the frequency of the RF input to the acousto-optical deflector. The experiments were intended to investigate a regime where the wavefunction of the atoms in the dipole trap extended over a region comparable to the lattice spacing, which implies that each pair of spots must be separated by no more than 1.5 microns. In order to have a stable trapping potential for the atoms, accuracy and stability of the radio frequency outputs was therefore crucial.

From an estimate based on the manufacturer's specifications for the AOD and a geometric optics model of our system we estimated that by changing the radio frequency by 1 MHz we would move the position of the beam where it intersected the atoms in the imaging plane by approximately 15 microns. If we assume that the non-RF portions of the system are ideal, we thus find that maintaining a separation of 1.5 microns to 0.1% requires a frequency accurate to approximately 100 Hz.

For this experiment all trap depths are ramped at the same rate so our main concern with the RF amplitudes is to balance out the diffraction efficiency at all frequencies used to ensure that all traps are of equal depth. Let us say that we want to do this to an accuracy of less than 0.1%, so we require that level of amplitude specification. For digital techniques the amplitude precision is often specified in terms of the number of bits used in the digital-analogue conversion; 0.1% corresponds to the precision of a ten-bit converter.

A significant advantage of our experimental design is the flexibility of our lattice. To take advantage of this flexibility to individually address a single well, we will need to be able to separate the wells adiabatically. Our numerical simulations suggest the trapping frequency of our wells will be on the order of 100 kHz, so for adiabatic changes we assume an update rate of approximately 5 kHz.

The requirements we have derived here are considerably less demanding than the requirements put on our optical system - indeed, for a single channel the requirements could be met with an off-the-shelf signal generator. With an initial aim of eight channels and an ultimate aim of up to twenty, we decided on investigation that it would be more efficient to build our own equipment, using Direct Digital Synthesis technology.

## 5.2 High Precision Frequency Synthesis

Traditionally, high stability generation of an arbitrary frequency was achieved by using a crystal or atomic oscillator to generate a stable signal at a fixed frequency in an appropriate range and then using analog circuits such as phase-locked loops to adjust from the oscillator frequency to the desired output frequency. (see Horowitz and Hill, 1989, section 13.12)

The analogue nature of the phase-locked loop means that a change of the desired output frequency will result in a gradual change from the original frequency to the new, often accompanied by some under- or over-shoot. In a traditional phase-locked loop one is also limited to output frequencies which are integral multiples of the reference frequency. Phase-locked loop circuits can also drift over time due to degradation of individual components.

Thus we see that PLLs on their own are not a good solution to the problem of generating rapidly changing RF frequencies with high precision. With the advent of digital signal processing, several more sophisticated techniques have been developed to address the problem - Goldberg (2000) gives an excellent account of the area. Below, I summarize the new technologies with most success:

**Fractional Phase-Locked Loops** The frequency resolution of a traditional PLL is given by its reference frequency; this tends to be large as the phase noise,

spurious signal and switching time all improve for higher reference frequencies. Fractional PLLs allow arbitrary non-integer ratios between the reference and the output frequencies by occasionally skipping cycles, in much the same way that leap-years keep the calendar in phase with the seasons. Fractional PLLs do still suffer from seek time on frequency changes, resulting in a relatively slow switching time.

**Direct Analogue Synthesis** A faster alternative to phase-locked loops comes in the form of direct analogue synthesis. In DAS, a number of different reference frequencies are combined via arithmetical operations to produce the desired output frequency. Switching time between frequencies can be as low as  $1\ \mu\text{s}$ . The disadvantage of this method is that each frequency required needs to be designed into the system explicitly, so system complexity scales linearly with resolution.

**Direct Digital Synthesis** An entirely digital alternative to the phase-locked loop for frequency synthesis was first implemented by Tierney *et al.* (1971); with recent advances in chip design the technology has matured to the point that single chips able to work at frequencies up to 400 MHz are now commercially available. This technology makes use of a digital phase counter and a sine lookup table to reconstruct a sine wave at arbitrary frequencies. The limitations of this technology are largely due to the digital-analogue conversion; this limits the maximum output frequency to 400 MHz and inevitably introduces some noise to the signal.

Having considered the available options, we decided that DDS was the most suitable technology for our purposes. Phase-locked loops were thought to be unsuitable because of their messy transition between frequencies, while a DAS system with 100 Hz resolution over 25 MHz would be very difficult to construct.

### 5.3 Direct Digital Synthesis: an overview

A schematic of the functional units making up a Direct Digital Synthesizer or DDS is shown in figure 5.1. With reference to the figure, let us consider how direct digital synthesis proceeds.

The reference clock at the lower left of figure 5.1 represents the oscillator input - as with analogue circuits, this is often supplied by a high-precision crystal or atomic source. In contrast to a phase-locked loop or direct analog synthesis, the oscillator input to a DDS is used only as a timing reference and not as an RF source. Each pulse of the reference clock results in an update of the analogue output value; clearly, the smallest time interval on which this output can repeat itself is every other sample. Accurate reconstruction of the signal is not possible from only two points, so in fact the condition for accurate reconstruction of an analogue signal is that the sampling frequency must be strictly greater than twice the highest frequency present in the wave to be reconstructed (known as the Nyquist criterion after Nyquist, 1928). In order to make implementation of anti-aliasing filters more straightforward, DDS designers recommend a reference clock frequency more than two and a half times greater than the highest frequency signal to be generated. (Gentile and Cushing, 1999)

From figure 5.1 we can see that two things happen simultaneously on each clock pulse: the constant  $M$  is added to the contents of the phase register and the current value of the amplitude is loaded into the digital-analogue converter. Let us consider the situation just after the circuit has been initialized, when all registers are empty. On the first pulse of the clock signal the DAC remains at its default state (the center of the sine wave) because the amplitude register is empty. At the same time, the user defined constant  $M$  is added to the empty phase register. The phase to amplitude unit reads in the value of the phase register and uses an internal look-up table to determine the amplitude of the sine function for that

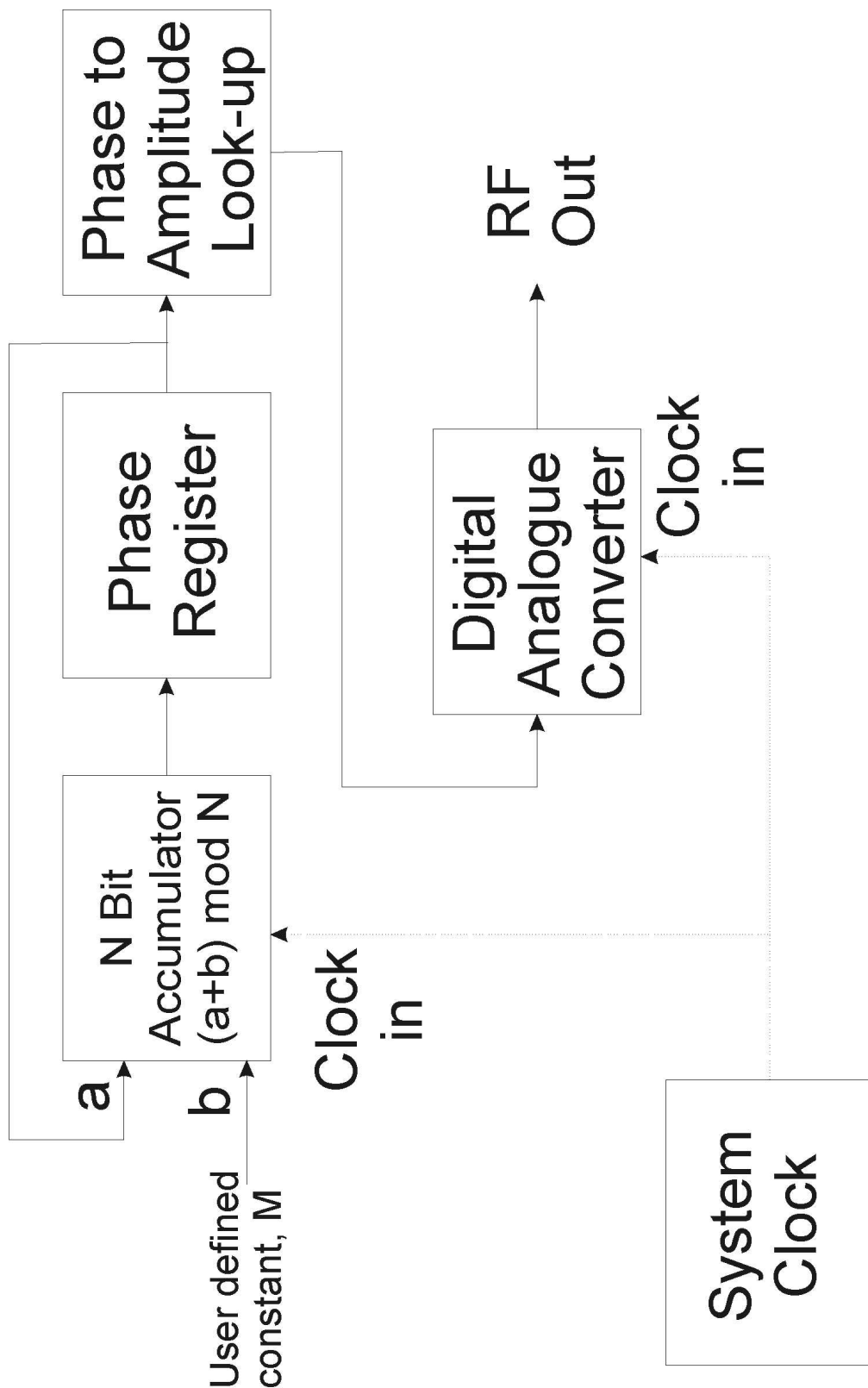


Figure 5.1: This figure shows the components making up a basic direct digital synthesis system. The user sets a frequency tuning word which determines how much phase is added to the output sine wave between updates of the digital-analogue converter. Having accounted for Nyquist's criterion, this allows the user to output any frequency up to half of the reference clock frequency.

phase. On the second clock pulse, this amplitude is loaded into the DAC and output as a current while the phase register (now equal to  $M$ ) is being added to  $M$  again to get the second value of phase. Thus the DAC is updating to the  $n$ th value of amplitude as the adder generates the  $n + 1$ th phase.

This discussion gives us some more perspective on some of the strengths and weakness of DDS technology mentioned briefly in section 5.2:

**Frequency Agility** From the preceding discussion, we see that the constant  $M$  defines the phase increment for each clock cycle and thus the frequency of the output sine wave.  $M$  is thus often described as the frequency tuning word, or FTW. Changing frequency thus requires only that a new value of the constant be loaded into the synthesizer's memory. In the present generation of chips this interface operates at 100 MHz so frequency can be updated to 48 bits resolution at more than 5 MHz.

**High Resolution** The  $N$ -bit width of the accumulator indicates the phase resolution of the synthesizer: typical DDS implementations use 48-bit phase accumulators, leading to a potential frequency resolution of less than a thousandth of a Hertz.

**Phase continuity** The phase accumulator continuously stores the present value of phase and is left unchanged when the frequency tuning word is altered. Thus changing the frequency does not result in a sudden change of output voltage, but instead starts from the same value of phase as the preceding signal. Sudden changes in output voltage introduce high-frequency signals into the output, so maintaining the continuity of the output voltage produces a cleaner signal.

The major remaining disadvantage of DDS technology is the relatively low frequency range (less than 400 MHz for a pure DDS system). In this case that

limitation is immaterial, as our desired operating range is 40-60 MHz. Because of the intrinsic dependence on digital-analogue conversion, DDS technology also has the drawback of a fixed noise floor: for a standard 12-bit DAC, the ratio between the signal power and the integrated noise cannot be higher than 75 dB for a full-scale signal at the maximum frequency of forty percent of the clock frequency. Note that this measurement is integrated over the full bandwidth: it does not tell us where or how individual peaks in the noise spectrum will be, though it sets an upper limit. (Gentile and Cushing, 1999) Analysis cannot improve on this measurement, but from the information supplied by DDS manufacturers we find that a typical maximum suppression of the largest spur relative to the signal is 52 dB for the range from 40-60 MHz (Analog Devices, 2004).

Ideally one would combine the amplitude outputs from several different signal generators digitally and then use a higher-quality DAC to convert the summed signal. This appears to be impractical as there is no commercial demand for DDS chips with digital rather than analogue outputs, and thus no commercial supply. We do not think that the noise ought to present major problems for our experiments, as even with only 52 dB of spur suppression noise on the RF will still be approximately two orders of magnitude smaller than the level of intensity stabilization we are planning for.

## 5.4 DDS Implementation

Our initial intention was for a lattice of up to ten rows by ten columns, requiring 20 DDS units. Buying off the shelf units would have been very expensive and difficult to interface, so we decided instead to commission a custom solution from the Physics Department's Central Electronics Group, working with Peter Hirst and David Halliday.

This solution is based around Analog Devices AD9852 Complete DDS chip, operating at up to 300 million samples per second (Analog Devices, 2004). Its 12 bits of amplitude resolution easily meet our requirement of control to 0.1%, while to meet our requirement of 100 Hz frequency resolution only requires 24 of 48 possible bits of frequency resolution. The amplitude and frequency settings are loaded into the chip via a parallel interface with a 6-bit address bus and an 8-bit data bus, both of which can cycle at up to 100 MHz. In addition to the basic DDS components discussed in section 5.3, the chip includes an internal phase-locked loop to multiply an easily obtainable 15-30 MHz signal to produce the chip's internal reference clock at up to 300 MHz.

The first iteration of the design had ten DDS chips on the same PCB. This iteration was not successful, in part because of a lack of understanding of the issues involved in the design of RF circuits and in part because of an over-optimistic design.

For the second iteration of the design, we decided that a modular scheme would be more flexible and robust and thus the design was based on several different components sharing the same interface. The components are listed and described below:

**Backplane** The backplane consists of two buses distributed along the back of a Eurocard mounting box: one carries a thirty-two bit data bus which interfaces with the DDS directly while the other carries power. Details of the data bus are given in table 5.1.

**DDS Module** After the first failed attempt at designing a PCB implementation of a DDS, we decided that it would be more efficient to use DDS modules on an evaluation board from Analog Devices. This board is mounted within a metal case which serves as a Faraday cage to reduce interference and coupling between channels. Each board receives power and instructions from the

backplane and the reference clock from an SMA connector on the front panel.

**Combiner** This module's primary purpose is to house the 4-way combiner which joins the signals from the individual DDS modules into a single RF output. It also houses the crystal oscillator which produces the reference clock at 60 MHz. It outputs the reference clock to via a front-panel SMA jack while drawing power from the backplane.

**PC Interface** This module provides an interface between the 68 pin output of our digital output card and the backplane. Just over half of the output pins are grounded or not connected; of the remainder, 25 form the data bus which is connected to the backplane, two are provided as SMA jacks for input/output and the final channel is the trigger input, also an SMA jack.

Rather than go directly to a ten by ten lattice, we decided to start on a smaller scale with eight DDS modules and two combiners. This gives us enough flexibility to do interesting experiments while reducing the technical complexity of the system.

### 5.4.1 Amplification

The evaluation board's output has an amplitude of approximately 0.1 V. For optimum diffraction efficiency, the AOD's RF input should be on the order of 12 V. To make up the difference between these figures we use a Minicircuits ZHL-5W-1 amplifier for each channel. This provides a fixed amplification of 37 dB at 50 MHz, so some reduction in amplitude is needed to stay within safe limits for the AOD. For our initial experiments, this reduction was supplied by reducing the DDS output intensity. As the noise generated by the digital-analogue conversion is constant, this approach results in a reduced signal to noise ratio. Ultimately, we hope to put a variable attenuator in place to allow us to operate the DDS at full amplitude throughout.

a)

<b>NI PCI-6534 Output Channel</b>	<b>Description</b>
A0-A5	Address Bus (6 bits)
A6-A7	Unused
B0-B7, C0-C1	Chip Select Bus (10 bits)
C2	Copy input buffers to operating memory (I/O Update)
C3	Master Reset
C4	Unused
C5-6	Available as Digital I/O
C7	Unused
D0-D7	Data Bus (8 bits)

b)

<b>Backplane Data Bus Channels</b>	<b>Description</b>
1-8	DDS Programming: Data Bus
9,16,18,29,31	Ground
10-15	DDS Programming: Address Bus
17	Copy input buffers to operating memory (I/O Update)
19-28	Chip Select
30	All DDS Modules: Master Reset
32	Channel One Control DAC Output

Table 5.1: Details of the data bus: a), as it is output by the DIO card and b), as it is distributed along the back plane of the DDS unit. Note that one signal appears on the backplane but not on the DIO; this is an analog signal output by DDS module one, intended for use as an amplitude control.

## 5.5 DDS Input/Output and PC Control

As discussed in section 5.4, the DDS modules are programmed via a parallel interface with six address bits and eight data bits. Each value of the address bus indicates eight bits of the DDS chip's memory which should be set to the value of the data bus: as one example, the amplitude of the DDS is stored in the last four bits of location 10 0001 and all eight bits of location 10 0010. The address and data buses are shared between all of the DDS modules but each module only loads the data presented if it is signalled using the chip select bus: each channel in the ten bit bus corresponds to one potential DDS module.

On a rising edge of the module's chip select line the DDS reads the value of the common address bus and prepares to write to that location in its input buffer. On the next falling edge of the chip select line, the DDS reads the value of the common data bus and writes this value to the location in its input buffer corresponding to the address bus previously loaded. Finally, by activating the IO Update line, all modules are instructed to copy the contents of their input buffers into their operating memory. This final stage is done separately so that modules can be updated with different operating data but all the changes come into effect simultaneously. As an aid to understanding, figure 5.2 shows the value of all relevant buses and registers during the process of loading data value D1 into address location A1.

Note that each DDS module has its own chip select line, while the IO update line is shared between all the modules. By using the chip select bus in this way we can use one address bus and one data bus to address ten different DDS modules separately or together, thus making most efficient use of our digital output lines. The address and data buses must be held in their final state for a minimum of 10.5 ns for the DDS modules to read their values accurately and thus the maximum possible update rate is just under 100 MHz.

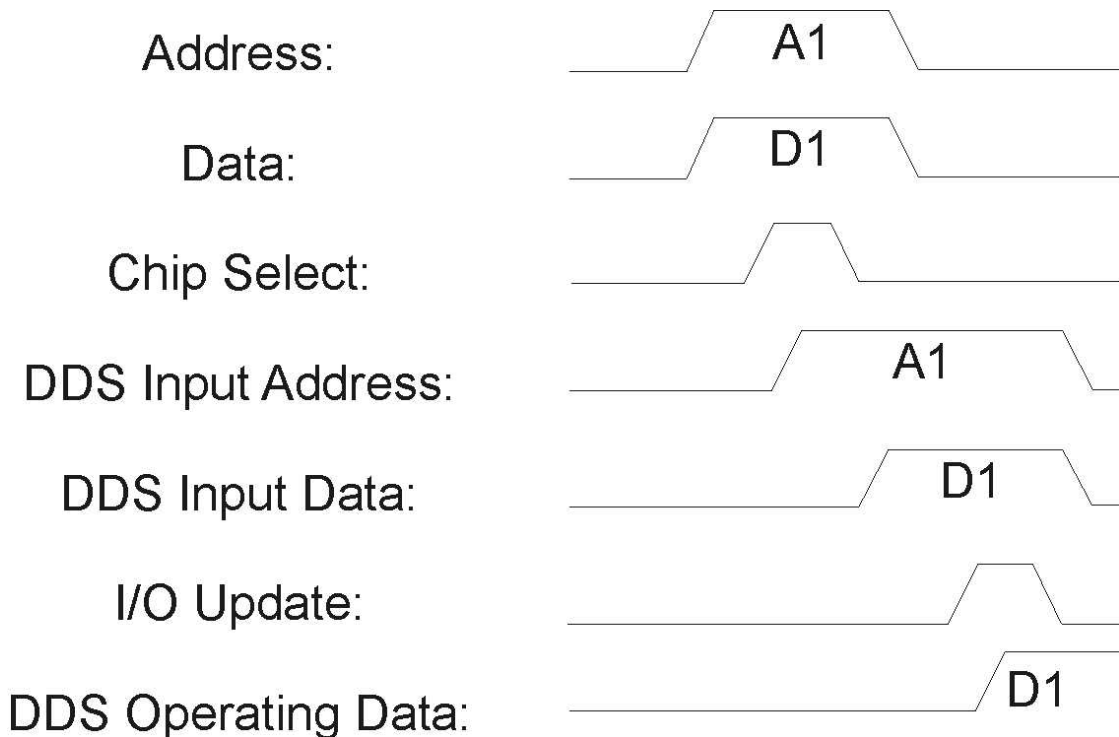


Figure 5.2: This is a visual illustration of the process of loading value D1 into address A1 of the DDS' operating memory. First the data and address buses are set to the desired value, then the chip select line for the DDS module in question is pulsed to load the value of the input buses to a temporary holding register. On the rising edge of the chip select pulse the address is loaded, whilst on the falling edge the data value is loaded. The IO Update channel is then pulsed: this causes the address and data held in the temporary register to be copied across to the DDS' operating memory and thus the change desired to take effect on the DDS output.

The input to this parallel programming system is driven by a National Instruments PCI-6534 digital output card installed on the PC which also controls the Andor camera used for imaging. The structure of the data bus as output from the PCI-6534 is described in table 5.1. This card outputs 32 bits and is capable of triggered or untriggered output at update rates of up to 20 MHz. There is 64 MB of memory available on the PCI-6534, allowing fully hardware controlled output sequences of up to 2.1 MHz-seconds: that is, 2.1 seconds at 1 MHz, 0.21 seconds at 10 MHz and so on.

Coordination between the DDS output and the remainder of the experimental sequence is handled by TTL logic: after evaporation is complete, the control computer uses a TTL signal to trigger the PCI-6534 board and thus begins the output of data to the DDS system for dipole trapping. The timing of the DDS output sequences is precise to less than 100 ns, so we put a delay equal to the length of the lattice ramps into the timing sequence for the main experiment and resume the imaging sequence when DDS output is complete.

### 5.5.1 Software Control

Automated control of the output from the PCI-6534 is clearly necessary to cope with update speeds of 20 MHz; it has the additional advantage of allowing the user to give human-intelligible instructions like ‘ramp the amplitude of module one from 20% to 40% over 200 ms, starting 400 ms into the sequence’ and have these converted into the much less intuitive instruction set understood by the DDS, briefly mentioned earlier in this chapter.

This automated control was achieved by designing a custom LabVIEW program. The major sub-sections of this program are described below: unless otherwise specified in the description, I did the design, programming and testing.

**DDS Control.** This is the backbone of the program; it co-ordinates the passing

of information between the other sections of the program described below. At execution, it allows the user to choose between running the sequence described in DDS Read-in (see below), initializing the DDS modules to zero output or controlling the data buses manually.

**DDS Read-in.** This sub-program provides the means for the user to specify the behavior desired from the DDS units in intuitive language. Users specify a series of events for each module; each event has a type, a start time and a duration. Event types allow the user to choose between sudden changes, linear ramps, exponential ramps or sinusoidal modulation of either frequency or amplitude. The program then compiles these individual module lists, counts the events to determine the required update rate and presents a master list of all required events to the remainder of the program. This structure of this part of the program was developed by Martin Shotter, a graduate student also working on this project but I have made some modifications to the details.

**Make Transfer Tables.** Converting the list of events generated by DDS Read-in into a list of output values for the PCI-6534 is a two-stage process: this sub-program is the first of those stages. It takes the list of events generated by DDS Read-in and generates for each one a list of instructions and timing values. For a simple amplitude or frequency change, this is just a single logical instruction (though it will take two sets of data values for amplitude and three for a frequency change); for a ramp the program generates an instruction for each step of the ramp. This sub-program then forms an unsorted array with all of the timing values and the PCI-6534 output values that need to be sent for each.

**Instructions to Output.** This is the second stage in the preparation of the out-

put values for the PCI-6534. It takes the unsorted array of output values and times from the Make Transfer Tables sub-program and outputs the sequence of values for the PCI-6534 output bus to assume in sequence. On first sight we might feel this to be simply a measure of sorting the input array; conceptually this is all that is required, but the detailed implementation is a bit more complicated because of the way the output is interpreted. No output takes effect until an IO update pulse has been sent. This means that we end up with a number of physical updates of the PCI-6534 bus being combined into a single logical unit of time - as an example of this phenomenon, three bytes are required to set the frequency of a single module to 24 bits of precision. To load each of these bytes takes three updates of the PCI-6534 bus. To put the change into effect requires an IO update pulse. Thus ten physical updates are required for a single logical update like a change of frequency; we might then set the physical update rate to 10 MHz, but we would only be able to specify changes at 1 MHz. Clearly this situation gets even more complicated if there are simultaneous frequency changes for multiple modules, or simultaneous frequency and amplitude changes for one module. In order to deal with this distinction between logical and physical updates this sub-program takes the time specified for each instruction and finds the set of physical updates corresponding to it. The program then scans through that set of physical updates to find the first unused update slot and puts the necessary instructions in place. It then checks to ensure that there is an IO Update pulse at the end of that logical update. The end result of this process is an array of values for the PCI-6534's output bus in the order in which they should be output.

**Strobbed Output** This sub-program takes the array of output bus values generated by the Make Transfer Tables sub-program, loads it into the PCI-6534's

onboard memory and then either executes the sequence immediately or sets the conditions for later triggered output. This program was largely assembled by a LabVIEW wizard, with only minor modifications required to allow the update frequency and size of the output array to be set within the program.

## CHAPTER 6

---

# A dynamically flexible lattice via acousto-optical deflection

In this chapter, I will briefly describe the apparatus used to implement our dipole trapping scheme where it is broadly similar to established techniques in the field. Those areas where our implementation is novel will be described in detail, particularly the direct digital synthesis (see chapter 5) of high-precision radio-frequency (RF) signals in combination with an acousto-optical deflector to generate a dynamically flexible dipole trapping potential.

In this chapter I will also describe the lasers used to generate the dipole trapping beam and the optics and acousto-optics that transfer the light of the laser to the atoms.

### 6.1 Lasers and Intensity Servo

We chose a wavelength of 830 nm for our dipole trapping light because it is close enough to the D2 lines to produce a strong dipole trapping potential in rubidium

while not being so close that heating effects from photon scattering are significant (see section 4.1.3). The wide availability of commercial optics for light at 830 nm was also an advantage.

From numerical simulations of the dipole trapping potential it is calculated that for a worst-case estimate of a 5-micron beam waist, approximately  $220 \mu\text{W}$  of power per spot would be required to generate a trapping potential of  $10 E_r$ , the correct order of magnitude for the Mott insulator transition. Thus, for a ten by ten array of spots, we require approximately 25 mW of useful power leaving the AOD. Given that the fibre-optic cable and the AOD have transmission efficiencies of approximately 50% , at least 100 mW of power is required at the fibre input. This is at the upper end of the power range available for diode lasers; using a pumped laser increases the complexity of the setup but rewards the effort with higher output power. As the group already owned a suitable titanium-sapphire laser, a pumped setup was chosen.

### 6.1.1 Lasers

The pump power for our dipole trapping beam is generated by a Coherent Verdi V-10 laser, supplying up to 10 W of light at 532 nm to pump a Coherent MBR-110 titanium-sapphire laser, adjusted to output at 830 nm. With a 9.4 W input beam, the MBR-110 generates approximately 1.3 W of light at 830 nm. The MBR also includes passive cavity stabilization using a piezo-controlled etalon.

A Coherent Innova 310 argon-ion laser was used for some early experiments; it was replaced with the V-10 to improve energy efficiency and quantum efficiency of the titanium-sapphire laser.

The layout of the dipole trapping laser table is given in figure 6.1 - the main point of interest on this figure is the acousto-optical modulator. This serves as the control element for the intensity servo, discussed further in section 6.1.2.

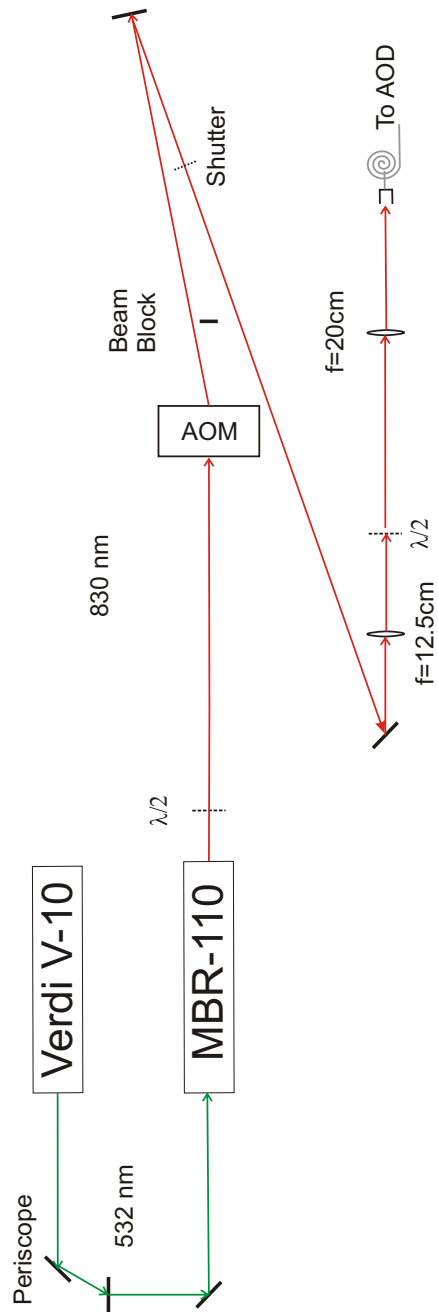


Figure 6.1: This figure illustrates the layout of the optical table on which the dipole trapping beam is generated and its intensity controlled. The input to the AOM used for intensity control comes from a lock circuit driven by the signal from the monitor photodiode on the main optical table. See figure 6.2 to follow the beam through the fibre.

### 6.1.2 Intensity Servo

As in earlier, similar work (Chuu *et al.*, 2005) dipole trap intensity is a critical parameter of our experiment. Left uncontrolled, factors ranging from thermal changes in the lasers to alignment drift will cause unpredictable changes in the intensity of the laser itself and thus in the trapping potential. In order to ensure that the power reaching the atoms is stable, we have installed a feedback servo, the optical elements of which are shown in figures 6.1 and 6.2.

A Crystal Optics 3080 acousto-optic modulator immediately after the MBR-110 on the main dipole trapping table provides the intensity control needed for the servo (see figure 6.1). The AOM's response time is governed by the time taken for a signal to propagate from the transducer to the interaction region, which from the AOM's data sheet (Crystal Technology, 2002) we deduce to be approximately 300 ns.

The two lenses between the beam-splitting cube and the fibre simply serve to change the beam waist from that output by the MBR to the correct waist for the fibre's input optics. Typically we achieve greater than 60% coupling efficiency through the fibre.

The intensity monitoring system can be seen illustrated in figure 6.2 - we use a series of polarizing beam-splitter cubes immediately after the fibre exit. The first cube serves as a polarization isolator, ensuring that any fluctuations in polarization caused by incorrect polarization alignment into the fibre are converted into intensity fluctuations in the beam to be servoed. The second cube is then used to pick off a small amount of light to use for the intensity servo - we use neutral density filters to ensure that even at maximum power through the cube, the power directed to the photodiode is within the linear regime ( $< 1 \text{ mW}$ ). The monitor beam is focused on to a ThorLabs DET110 photodiode to provide an analogue measurement of beam power; as the photodiode is terminated through a  $50 \Omega$  re-

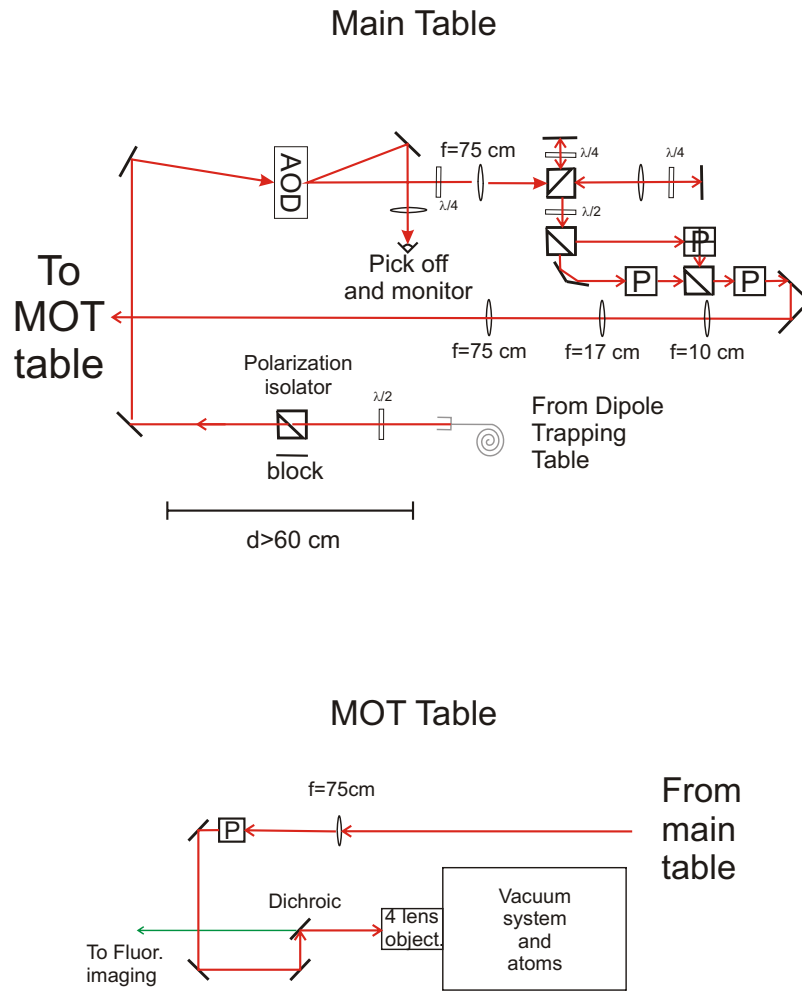


Figure 6.2: This figure illustrates the layout of the dipole trapping optics found on the main optical tables (that is, the tables primarily used for the cooling and trapping optics.) Note the change of direction of the laser beam after passing through the AOD; the first order beam in the center of the device's bandwidth defines the axis for all points after the AOD. Note also the slightly off-axis beam directed to a photodiode; this is used as the monitor signal for the intensity servo. The lattice optics begin with the 75 cm lens immediately after the intensity servo pick-off and are discussed at length in section 6.3.1: in this diagram, periscopes which do not change the beam's direction in the plane of the table are represented by the letter P within a box. A cross superimposed on the P indicates a periscope that also deflects the beam by 90°. Another point to note is the dichroic mirror, which reflects the dipole trapping light while allowing fluorescent light through to the imaging system.

sistor, it has a bandwidth of approximately 160 MHz, which gives a rise time of approximately 20 ns.

The link between intensity monitoring and control is provided by a proportional-integral-differential lock circuit designed for our experiment by Dr. D. T. Smith of the Physics Department's Central Electronics Group. This circuit compares the voltage from the photodiode to a control voltage supplied from the experimental control computer and changes its output voltage to try to make the two input voltages equal.

This output voltage is connected to the control voltage input of a Minicircuits ZX73-2500 voltage variable attenuator via an adder which offsets it to the center of the linear range. This attenuator is used to control the RF power input to the servo AOM, and thus controls the amount of light passed through the AOM setup described above. The response time of the ZX73 is specified as 25  $\mu$ s, and is thus the limiting factor in our intensity control setup. Given this limit, we can expect to stabilize the beam power against noise at up to 40 kHz, approximately one order of magnitude greater than the expected lattice trapping frequencies in our apparatus.

In order to measure the stability achieved by the intensity servo, we placed mirrors immediately before the four-lens objective to divert the lattice beams via a lens to be focussed on to a second, identical DET110 photodiode. Monitoring this power, we observed that the photodiode signal from the beam was stable to less than 0.5% for timescales from milliseconds to tens of minutes.

## 6.2 Acousto-Optics

Acousto-optical devices are widely used in experiments with cold atoms for tuning laser beams and providing fast intensity switching and modulation. The same

effect can be used to produce spatial deflection: this effect has been used by Yavuz *et al.* (2006) to demonstrate addressability of cold atom qubits for single-qubit operations in separate dipole traps and by Shin *et al.* (2004) to coherently split a single BEC into two.

In this section I will briefly review the principles of acousto-optical deflection and then discuss the details of our experimental implementation of it.

### 6.2.1 Acousto-Optical Deflection

A crucial feature of our experiment is the use of a two-axis acousto-optical deflector: in combination with the optics discussed in section 6.3.1 the motion produced by the AOD generates the dynamic lattice spacing and lattice rotation. In this section, I will review the theory describing acousto-optical deflection, largely following the path laid out in Yariv (1971, Chapter 12). A more technical short review of acousto-optics is given by Gordon (1966), while Magdich and Molchanov (1989) cover the field in considerable detail.

Consider a sound wave as a sinusoidal perturbation of the material density travelling through the medium with speed  $v_s$  and frequency  $\omega_s/(2\pi)$  on the order of 50 MHz. The sound wave will have associated with it a perturbation in the refractive index  $n$  of the material arising from the fluctuation in number density of the particles making up the medium and the change in the optical polarizability of the medium due to the strain of that fluctuation. For simplicity, we assume that the variation in refractive index is related to the sound wave by a scaling factor, so that

$$\delta n(z, t) = \delta n_0 \sin(\omega_s t - k_s z) \text{ where } \frac{\omega_s}{k_s} = v_s$$

A change in refractive index leads to some reflection of a beam crossing the interface, so for a simple classical picture we can consider the sound wave as a series

of mirrors separated by the sound's wavelength  $\Lambda$  - implicitly, this model assumes that the width of the sound wave is much greater than  $\Lambda$  and thus that diffraction effects can be neglected for the sound wave. By arguments familiar from consideration of Bragg scattering in crystals, we can derive the Bragg condition determining the required incident angle  $\theta_i$  for a optical beam of wavelength  $\lambda$  to be diffracted:

$$2\Lambda \sin \theta_i = m\lambda$$

where  $m$  is a non-negative integer. For practical applications, this result is usually rewritten using the relationship  $v_s = f\Lambda$ , as experimentally we have a much better idea of the frequency of the radiation  $\nu$  and the speed of sound in the crystal  $v_s$  than of the wavelength of the sound in the crystal! Substituting these quantities in we find that the deflection angle  $\Theta = 2\theta_i$  of the first-order beam from the zeroth order is:

$$\sin \frac{\Theta}{2} = \frac{\nu\lambda}{2v_s} \quad (6.1)$$

### 6.2.2 Beam steering

Using a plane acoustic wave as above, it is possible to choose the diffraction medium, incidence angle and sound wave frequency so as to get nearly perfect deflection of the incident beam. Yariv (1971, Section 12.3) goes through the mathematics involved in detail. In relation to acousto-optical deflection, it is important to note that in the simple case described above a change in acoustic frequency will necessarily mean that a beam with constant  $\theta_i$  will no longer be at the Bragg angle. This deviation from the Bragg angle means that momentum can no longer be conserved in the scattering process; scattering will still occur in the direction closest to conserving momentum, but the scattering efficiency is reduced. The

effective bandwidth<sup>1</sup>  $\Delta f$  of a deflector driven by a plane-wave transducer is given by Korpel (1981) as:

$$\frac{\Lambda}{L} > \frac{1}{2} \frac{\lambda}{v_s} \Delta f \quad (6.2)$$

where  $L$  is the length of the transducer producing the acoustic wave in the direction perpendicular to the wave's propagation. We can qualitatively understand equation 6.2 as requiring that the range of acoustic propagation angles due to diffraction (the left-hand side) must be greater than the total angular deflection required from the system (the right-hand side, to a factor of 2). For a plane wave AOD, then, a large deflection range requires a small transducer, and the resulting narrow interaction region results in poor diffraction efficiency.

Deflectors with a wider bandwidth can be obtained by using an array of transducers to create a frequency-dependent distribution of acoustic power in place of the fixed plane acoustic wave discussed above: this is known as beam-steering. The simplest case of a flat grating is analysed in Gordon (1966). The following discussion follows the clear explanation presented in section 3.6 of Magdich and Molchanov (1989).

Consider an array of  $M$  transducers with width  $d/2$ , all driven coherently from the same source but with a phase difference of  $\pi$  radians between adjacent transducers, illustrated in figure 6.3 (c). This arrangement produces an intensity pattern equivalent to that of two transducers of the same total length at angles of  $\pm\alpha = \pm(v_s/(fd))$  to the x-axis defined by the array of transducers. Note that the magnitude of  $\alpha$  is dependent on the frequency of the acoustic wave, so the change

---

<sup>1</sup>Note that the term bandwidth is used with slightly different assumptions when discussing acousto-optical modulators (the more common case) and acousto-optical deflectors. In discussing acousto-optic modulators, it is assumed that you will pick one frequency to drive the modulator and align the modulator for that frequency: thus bandwidth is determined by the range of frequencies over which it is possible to find an alignment of the AOM that gives good diffraction efficiency. When dealing with deflectors, it is assumed that the AOD has a constant alignment for a range of frequencies: bandwidth is thus the range of frequencies over which good diffraction efficiency can be obtained for a constant alignment of the detector relative to the beam.

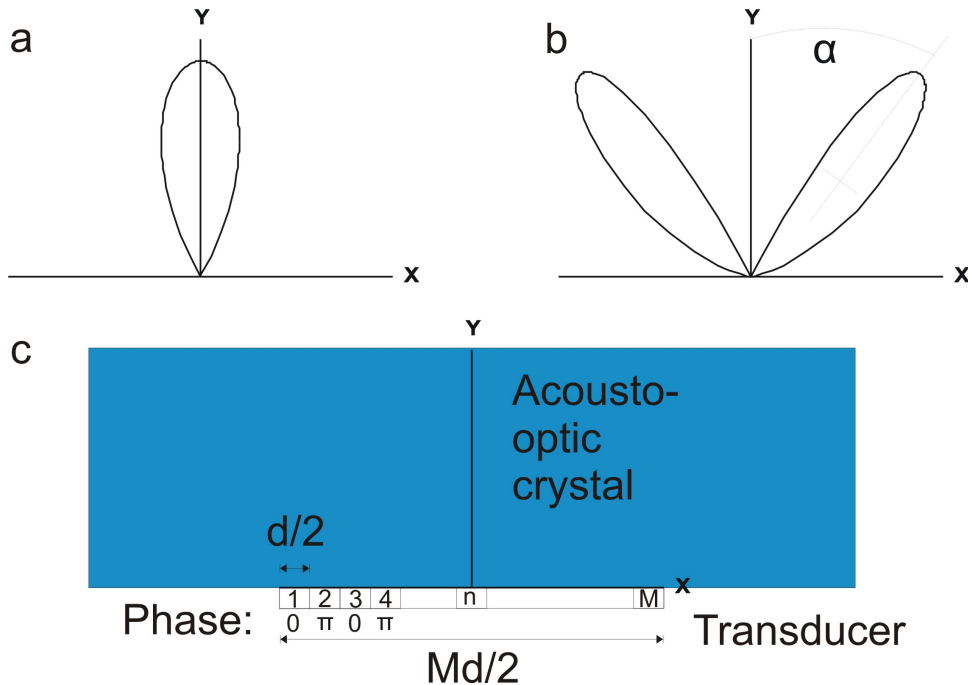


Figure 6.3: Graphs (a) and (b) are the polar graphs for two different types of transducer. The distance from the origin to the line at a given angle indicates the proportion of output power radiated along that direction. Graph (a) is the pattern for a single transducer of size  $\frac{Md}{2}$ . Graph (b) shows the pattern for an array of  $M$  adjacent transducers each of width  $\frac{d}{2}$ , where adjacent transducers are out of phase by  $\pi$  radians. Note that the angle  $\alpha$  separating each lobe from the  $\phi = 0$  axis is dependent on the frequency of the sound wave. Thus light incident at a constant angle to the transducer will experience an angle of incidence to the acoustic wave dependent on the acoustic frequency; this frequency dependence is used to keep the angle of incidence close to the Bragg angle over as wide a range of frequencies as possible. (c) is a schematic diagram of the layout of the transducer array used for beam steering.

in Bragg angle caused by a change in frequency can be partially compensated for by the change in direction of acoustic wave propagation. With appropriate choice of design parameters, the bandwidth of a deflector using such an array of gratings can be approximately four times greater than the bandwidth achieved with a single plane-wave transducer of equivalent length. (Magdich and Molchanov, 1989) As only one of the two lobes is used, approximately 60% of the energy in the acoustic wave does not produce deflection. Korpel *et al.* (1966) proposed the use of a blazed grating of transducers with alternating phase, which produces one lobe and thus achieves greater acoustic efficiency.

### 6.2.3 Details of Implementation

For our experiment we use an ISOMET LS110-830XY, built around two crystals of tellurium oxide ( $\text{TeO}_2$ ) mounted orthogonally, each providing deflection in one axis. The deflector has a bandwidth of 25 MHz centered on a frequency of 50 MHz; this corresponds to an angular deflection of 1.9 degrees. Beam-steering is used to maintain the Bragg angle continuously over this range, with the phase delay supplied by splitting the input RF signal in two and passing one of the two resulting signals through a delay line.

Typically we obtain diffraction efficiencies of approximately 75% in each axis individually, giving approximately 50% of the incident laser power being deflected into the beam deflected by 50 MHz in both axes.

### 6.2.4 Amplitude Normalization

As discussed in section 6.2.2, the diffraction efficiency of the AOD varies with the deflection frequency; the output power from the DDS and the gain of the amplifiers will also vary, though these effects are less significant over the relatively small frequency range with which we work. This clearly is not an issue when

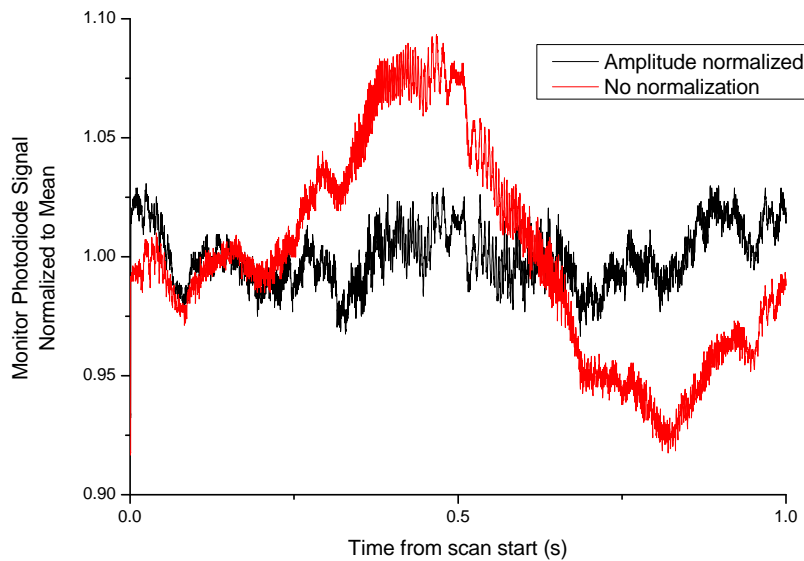


Figure 6.4: This figure illustrates the variation in power transmitted through the lattice optics to the four-lens objective both before and after amplitude normalization is applied. Before normalization is applied we observe intensity variation of  $\pm 8\%$ ; after normalization this is reduced to  $\pm 2\%$ . The data shown is one complete rotation of the lattice.

dealing with a static lattice, but it could become a source of significant heating when we come to rotate the lattice. The level of power fluctuation observed for a typical rotation is illustrated in figure 6.4

In order to reduce the impact of this noise, we implemented a method we describe as ‘normalized amplitudes’ to level out the power variation during rotation. When amplitude normalization is active, each time the DDS software changes the output frequency it also changes the amplitude by a corrective factor in order to obtain the same output power. Say that at 55 MHz on the x-axis the power output for a given DDS amplitude is 95% of its value at 50 MHz. Thus, if the DDS was set to give 50% of full scale output at 50 MHz and the frequency was then changed to 55 MHz, the DDS software would simultaneously change the output amplitude to  $\frac{50}{0.95} = 52.6\%$  of full scale.

In order to determine these normalization coefficients, we used a 10 cm lens to focus first-order output from the AOD on to a photodiode as soon as practical after the AOD itself. We then scanned each axis through a range of frequencies around the optical axis while the other axis was left at its center value and recorded the power reaching the photodiode using a digital storage oscilloscope.

We saved these traces digitally, normalized each trace to its value at the center of the frequency scan and inverted the resulting values to obtain the correction factor for that point in the sweep. We then picked out the correction factors which corresponded to frequencies at even multiples of 100 kHz for 3 MHz either side of the optical axis of the lattice system to save as correction factors. The software will automatically perform a linear interpolation to determine the correction factor for any frequency which lies between two of the saved normalization points.

Applying these normalization coefficients to a single rotation of a 2 MHz-spacing lattice and monitoring the lattice beams just before the 4-lens objective as before we obtain the black trace in figure 6.4. This is stable to approximately  $\pm 2\%$ : it is likely that this could be improved further, but we decided to wait for the improved setup discussed in section 8.3 before attempting this.

## 6.3 Optical Setup

In this section I shall discuss the optical setup around the acousto-optical deflector. As the optics surrounding the intensity servo have been discussed extensively in section 6.1.2, this section deals only with the optics illustrated in figure 6.2. To illustrate the principle of the scheme, I will first describe the simplest implementation of the same principles: hopefully this will illuminate the later technical discussion of the system as it exists in our experiment. Another discussion of the technical details of the implementation can be found in Williams *et al.* (2008).

### 6.3.1 Initial Optics

From the dipole trapping table (illustrated in figure 6.1), the dipole trapping beam is transferred to the main table by means of a single mode polarization preserving optical fibre: this also serves as a spatial filter, improving the mode quality of the output light. Typically we obtain approximately 60% transmission efficiency through this fibre.

On emerging from the fibre, the light is collimated to a  $1/e^2$  beam diameter of approximately 5 mm. By using such a large beam diameter, we reduce the extent to which the beam will diffract in passing through the aperture of the AOD and thus we maximize the number of distinguishable beams generated by the AOD: this is not crucial for the current configuration of the experiment. The optical layout after being collimated out of the fibre is shown in figure 6.2

The polarization preservation of the fibre is not perfect, so we also place a polarizing beam-splitter immediately after the fibre. This converts any fluctuations in polarization from passing through the fibre into intensity fluctuations, which are removed by the intensity servo. The polarization of the beam is then adjusted to give maximum diffraction efficiency in the AOD.

Immediately after the AOD, we have a single, 5 mm diameter beam deflected once in each of the  $x$  and  $y$  axes: the other orders are blocked by a beam shield. This first order beam must be converted into a set of beams which when focussed by the four-lens objective will generate a two-dimensional lattice in the focal plane of the objective lens. This can be accomplished by an arrangement of optics developed by my co-workers Ross Williams and Jean-Damien Pillet.

### 6.3.2 Scheme in Principle

Figure 6.5 illustrates the basic principles of the scheme. The simplest implementation of the concept resembles a Michelson interferometer: we begin with a non-

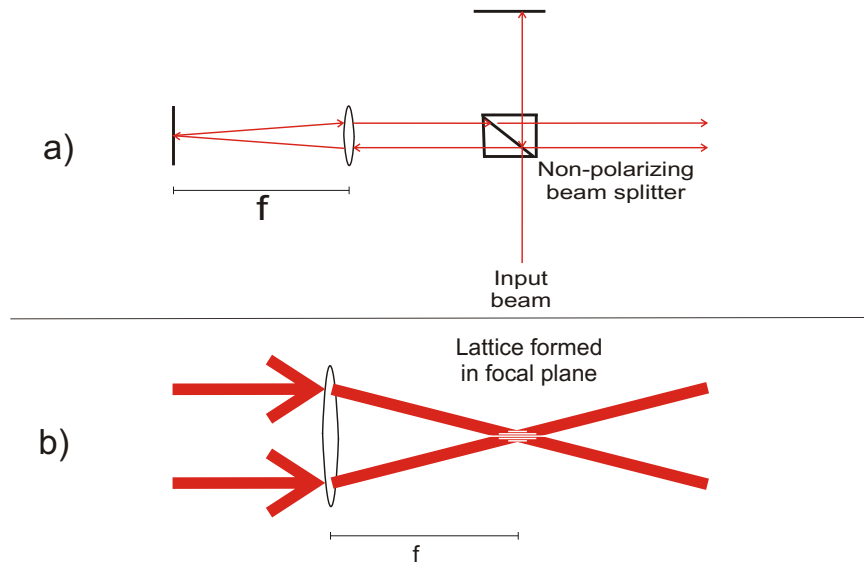


Figure 6.5: An illustration of the lattice scheme in one dimension. a) illustrates the optics involved, discussed further in the text. b) is a depiction of how the beams generated by this scheme interact to form a lattice in the focal plane of a focussing lens.

polarizing beam splitter (NPBS) which divides the incoming beam equally between the two arms of the interferometer. One arm just consists of a mirror reflecting the beam back on to the NPBS, where half of it is reflected off towards the remainder of the system.

The other arm contains a lens, which bends the beam to the axis of the lens in its focal plane. A mirror is then placed in the focal plane and aligned perpendicularly to the incoming beam path so the beam is reflected back towards the lens at the same angle to the optical axis but on the opposite side of the axis. When this beam reaches the lens it is made parallel to the optical axis of the lens and thus to the incoming beam, but it is displaced to the opposite side of the optical axis. This beam is partially transmitted through the beamsplitter: thus the result of the whole apparatus is to produce two parallel beams at  $90^\circ$  to the incoming beam path. Part b of the same figure illustrates how these two parallel beams create a one-dimensional optical lattice in the focal plane of a focussing lens.

Note that as the lenses and mirrors are rotationally symmetrical that this scheme will produce a one-dimensional lattice regardless of the direction in which the input beam is displaced from the optical axis: the orientation only determines the orientation of the fringes. Thus a one-dimensional horizontal lattice can be constructed by using the AOD to deflect a beam by 52 MHz in the  $x$  axis and 50 MHz in the  $y$  axis, while a vertical lattice might use a deflection of 52 MHz in the  $y$  axis and 50 MHz in the  $x$  axis. A rotating lattice can be constructed by sinusoidally varying the frequency of deflection for both axes, with a  $\pi/2$  difference between the two axes' modulation phase.

### 6.3.3 Experimental Implementation

The simple scheme discussed above is a poor idea experimentally because it discards half the available power: with an ideal NPBS each of the two output beams will have only a quarter of the power of the input beam. To generate a lattice we require that the two beams are coherent, which implies that this power loss is unavoidable for the two-beam case corresponding to a one-dimensional lattice. More options become available when we move to the four-beam configuration needed for a two-dimensional lattice. Figure 6.6 is a detail from figure 6.2, giving a clearer view of the lattice optics as we have actually implemented them experimentally. We now use polarization components instead of the non-polarizing beam-splitter used in the simpler discussion. Thus the first component of the lattice optics is a quarter-wave plate: this is adjusted to ensure that the beam power is divided equally between the two outputs of the polarizing beam splitter. The 75 cm lens is placed so that its back focal plane is the output of the AOD, and thus it converts the angular displacement of the deflected beam into a displacement from the optical axis. The optical axis in this case is defined as the path of the beam deflected by 50 MHz in both conventional axes. The optical axis is indicated by the arrows

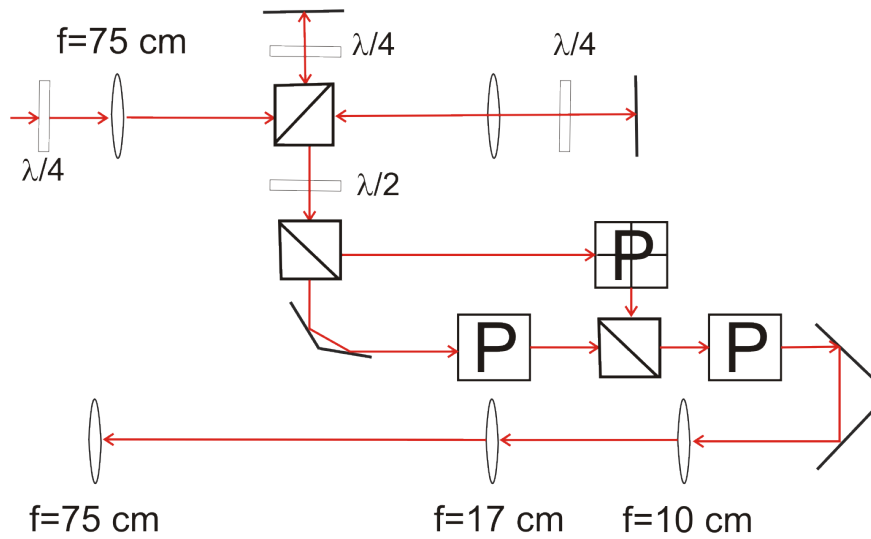


Figure 6.6: A detailed view of the optics used to generate the four parallel beams which produce a two-dimensional optical lattice when focussed through the four lens objective. Note that this setup uses polarizing beam-splitters in place of the PBS in figure 6.5. As in figure 6.2, the letter P enclosed in a square represents a normal periscope while a cross superimposed on the boxed P indicates a periscope which also deflects the beam by 90° in the horizontal plane.

in figure 6.6.

The next section of the apparatus is almost identical to the system discussed in section 6.3.2: the one change is the use of a polarizing beam splitter (PBS). As the input light is circularly polarized, the beams in each arm have equal power and orthogonal linear polarizations. The quarter-wave plates in each arm are set so that when the beam has passed through the wave plate twice (once outwards, once on the return journey) the polarization is rotated by 90°. The arm that was reflected is now transmitted and vice-versa, so both beams continue "down" the diagram.

Leaving the upper, interferometer-like section of the apparatus we have two parallel beams of orthogonally polarized light: these both pass through a half-wave plate which rotates their plane of polarization through 45°. Thus each of the two beams is now made up of an equal mixture of horizontally and vertically polarized light. When the beams pass through the following PBS, both spots

are split equally to give two parallel beams of identical polarization in each arm. (Clearly the polarization of the beams in one arm is orthogonal to that of the beams in the other.)

The vertically polarized components are reflected by the PBS and directed into a periscope with the upper and lower mirrors mounted at  $90^\circ$  to each other. This rotates the pair of beams through  $90^\circ$  and thus changes the horizontal displacement between the beams before the periscope into a vertical displacement between the beams afterwards.

The horizontally polarized components of the two beams are transmitted by the PBS, and sent to an arrangement of two mirrors at  $45^\circ$  to each other. This arrangement is similar to that of the pentaprisms commonly used in photography: it deflects the parallel beams through  $90^\circ$  without changing the handedness of the image. This is required to ensure that when the lattice is rotated both the horizontal and vertical fringes rotate in the same sense.

Both arms are recombined on the final PBS, producing a square of four parallel beams, with adjacent vertices of the square having orthogonal polarization. The intensity distribution of these beams when focussed through a lens is illustrated in figure 6.7.

After leaving the final PBS, all that remains is the remainder of the telescopes for preparing the beam size and separation for the 4-lens objective. Looking at the optics laid out in figure 6.2 we see that there are six lenses between the output of the AOD and the atoms; all are separated from the preceding and following lenses by the sum of the two lenses' focal lengths, so there is effectively a series of three telescopes. There are two quantities of interest to trace through this system: the displacement of the beam from the optical axis and the waist size of the beam. The displacement of the beams from the optical axis determines the lattice spacing, and so will be discussed in relation to our calibration in section 7.1.1.

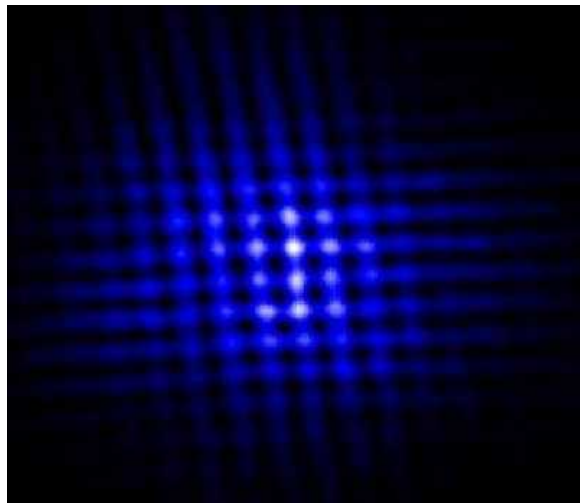


Figure 6.7: This image was taken by focusing the four beams generated by the apparatus discussed in section 6.3.3 on to a Starlight XPress SXVF M7 camera. It illustrates the formation of a two-dimensional lattice at the intersection of the beams. This data was taken and the figure generated by Ross Williams.

The lattice trapping beam is initially collimated with a  $1/e^2$  radius of 2.75 mm. In passing through the telescopes the beam waist of the lattice beam is reduced by a factor of 0.03, resulting in a beam waist after the 4-lens objective of approximately 80 microns.

### 6.3.4 Polarization and the rotating lattice

Section 6.3.3 describes the scheme as it existed for the experiments described in this thesis: in particular, the lattice beams were polarized vertically and horizontally. In this arrangement the potential depth of the lattice will vary sinusoidally during a circular rotation.

To understand how this variation occurs, let the focal plane of the lattice optics be parallel to the  $x$ - $y$  plane and consider the horizontally polarized lattice beams. If we allow the lattice beams to rotate around the axis of the system, the lattice beams will have some separation in each of the  $x$  and  $y$  directions. We consider the two extreme situations: first, where the lattice beams are initially separated

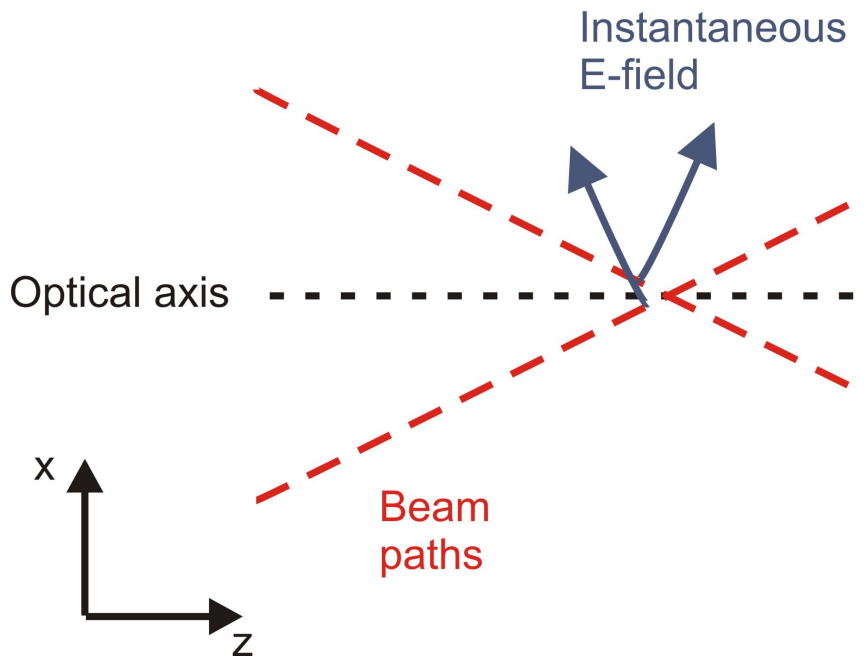


Figure 6.8: This figure illustrates the situation when horizontally polarized lattice beams are separated in the  $x$  direction. The instantaneous  $E$  field from the upper and lower beams have components in the  $x$  and  $z$  directions. The component in the  $x$  direction provides the lattice: the fields interfere constructively to increase the field. The components in the  $z$  direction from the two beams have opposite signs, and cancel out. Thus some of the  $E$  field does not contribute to the lattice, resulting in a lower lattice depth than is obtained when the beams are separated vertically.

in the  $x$  direction to give fringes parallel with the  $y$  direction and secondly where the lattice beams are initially separated in the  $y$  direction and give fringes parallel with the  $x$  direction.

When horizontally polarized lattice beams are separated in the vertical direction, their associated electric fields will be parallel to each other: when the two beams interfere, the intensity in the peaks  $I_p$  will be equal to four times the intensity in a single beam  $I_0$  ( $I_p = 4I_0$ ) and the intensity in the troughs  $I_t$  will be zero ( $I_t = 0$ ). When horizontally polarized beams are separated in the horizontal direction, however, their electric fields do not lie completely in the focal plane of the lattice system. Figure 6.8 illustrates this situation. At  $x = 0$ , for example, that portion of each beam's electric field which lies in the plane of the lattice will

interfere constructively while the portion which is perpendicular to the plane will interfere destructively. In this case the maximum intensity in the lattice will be less than four times a single beam intensity ( $I_p < 4I_0$ ) and so the lattice depth will be lower than it was for a vertical separation of the beams.

Thus as this pair of beams is rotated from vertical to horizontal and back again the lattice depth will fluctuate. This change in the potential will heat the atoms. This problem does not arise when the lattice beams are circularly polarized: in this case the proportion of the field lost as described above is constant throughout the rotation. Circular polarizations are thus strongly recommended for future implementations of the rotating lattice scheme!

### 6.3.5 Aligning the lattice optics

The procedure for aligning the lattice optics requires care and patience, but is conceptually simple. For the purposes of alignment, the system can be broken into two portions. In figure 6.6, the first section is the interferometer setup above the half-wave plate and the second section the periscopes below it.

The two arms of the interferometer are aligned by removing the waveplates so that light incoming along the optical axis of the system is reflected from the mirrors and transmitted back along the input beam. This can be optimized by arranging the reflected light to be back-coupled through the dipole trapping fibre.

The second half of the system should be aligned with two conditions in mind: first, that the output beams from the two arms are counter-propagating and secondly that the beam should be able to be rotated at the largest possible frequency gap without clipping. This is best accomplished by monitoring the beam just after the lattice optics and just before the 4-lens objective with CCD cameras; counter-propagation can be achieved roughly by viewing a single beam rotating and more carefully by ensuring the lattice fringes do not change size during rotation.

Following this procedure carefully can take several days.

### 6.3.6 Aligning the beam on to the atoms

As we built the experiment, one of the major hurdles we faced was obtaining and maintaining the alignment of the lattice beams on to the atoms: in all we probably spent months on this alone. In time, we developed the procedure which I will describe in this section: by following this procedure we can align the lattice beams from scratch within approximately a week.

The largest single improvement in our alignment procedure came from adding the axial absorption beam, discussed in section 3.9. We begin aligning the axial absorption beam by ensuring that the beam falls on to the CCD; we then try to use the axial absorption beam for imaging, successively increasing the size of the cloud until we can see the edge of the cloud in the absorption image. The axial absorption beam can then be walked so that it is centered on the BEC.

If aligning the system from scratch, the next step is to ensure that the axis of the 4-lens objective is aligned along the axial absorption beam (and thus hopefully along the axis of the cloud). We accomplish this by inserting a carefully machined cylinder into the barrel of the 4-lens objective; the cylinder has small central apertures top and bottom and is machined to within 50 microns of the objective barrel's diameter along a length of 30 mm. We align the objective by measuring the power of the axial absorption beam after passing through the objective and change the alignment of the lens to maximize the transmitted power.

Having followed the procedure thus far we have a well-aligned set of lattice beams and an axial absorption beam which is centered on the magnetic trap and passing along the axis of the four-lens objective. The next stage is to take a single dipole trapping beam on the axis of the lattice optics and ensure that it is counter-propagating with the axial absorption beam. This alignment cannot be done as

precisely as other stages of the procedure because the axial absorption beam is rapidly expanding after the 4-lens objective. Thus the lattice beams should be focussed near the magnetic trap, but are not necessarily precisely aligned on to it.

Having followed the procedure thus far, ideally one would observe an effect on the cloud from exposure to the dipole trapping beam and then optimize the alignment to maximize the effect. Because of the uncertainty in the final stage of the alignment discussed above, however, sometimes no effect is observed. In order to locate the atoms more precisely we tune the Ti-Sapphire from 830 nm towards resonance at 780 nm in order to increase the effect of the beam on the cloud. Having observed some effect it is then straightforward (if time consuming) to optimize the alignment, changing the laser wavelength towards 830 nm in steps of about 20 nm as one goes.

### 6.3.7 The Four Lens Objective

Recall from equation 7.1 that the fringe spacing  $d$  in the focal plane of a lens is inversely proportional to  $\sin \alpha$  where  $\alpha$  is the angle between the interfering laser beams and the optical axis in the focal plane of the lens. Thus for a fixed wavelength increasing the angle  $\alpha$  decreases the fringe spacing: the maximum value of  $\alpha$  and thus the minimum fringe spacing is determined by the numerical aperture of the lens used to focus the beams<sup>2</sup>. We therefore seek to maximize numerical aperture in order to obtain the smallest lattice spacing possible.

As part of the previous experimental concept, we intended both to pursue high resolution fluorescence imaging to resolve small numbers of atoms and to produce an array of tightly focused spots. Both of these aims also require a high numerical aperture lens so a suitable lens was designed and built by Baranowski (2005),

<sup>2</sup>The numerical aperture or NA is defined as  $NA = n \sin \theta$ , where  $n$  is the refractive index outside the lens and  $\theta$  is the largest angle to the optical axis obtained when collimated light is focussed through the lens. (Jenkins and White, 1937)

modified from an original design by Alt (2002). In his original design, Alt looked for a system to collimate radiation from a point source that would meet five criteria:

- The lens system must produce a diffraction limited spot-size on axis for high resolution imaging.
- In order to capture as many fluorescence photons as possible, the lens system must have a large numerical aperture.
- It must minimize spherical aberration for the combined lens-vacuum cell system.
- The working distance must be large ( 40 mm) to allow space for magnetic coils and optical access.
- The diameter of the system must be less than 30 mm to fit between the existing coils.

All of these criteria are still relevant for our purposes - the most significant modifications made to Alt's scheme were to shift its operating wavelength from caesium's resonance at 852 nm to rubidium's at 780 nm. Both the original design work and Baranowski's modifications were done by using Sinclair Optics' OSLO ray-tracing software to vary the radii of curvature of the lenses and the spacing between them for fixed values of the operating distance and numerical aperture to find the configuration which produced minimum aberrations<sup>3</sup>.

Figure 6.9 shows the final lens system, as optimized for imaging at 780 nm. Given that the lens nearest to the atoms has a clear aperture of 23.5 mm and the working distance of the lens is 40.5 mm, geometry tells us that the numerical aperture must be less than or equal to 0.28. In fact, OSLO suggests an effective numerical aperture of 0.27 after accounting for residual aberrations.

---

<sup>3</sup>See <http://www.sinopt.com/> for more information about OSLO

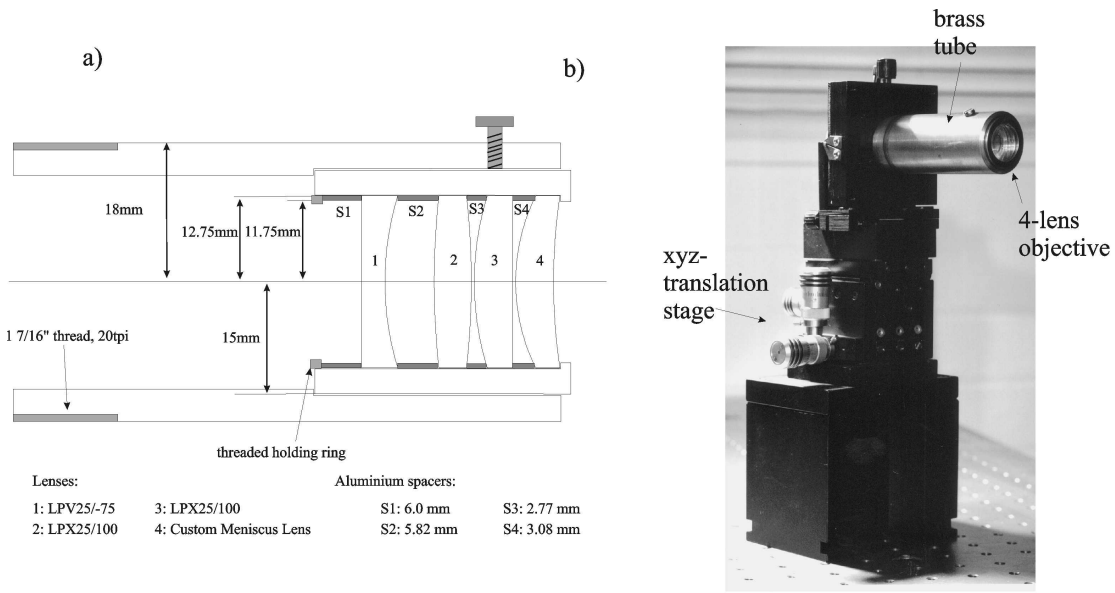


Figure 6.9: a) illustrates the construction of the 4-lens objective. It was assembled in a brass tube, with precisely machined spacers between the lenses. All lenses are 25.4 mm in diameter. The aperture is limited to 23.5 mm by the retaining ring visible at the end of the lens. b) is a picture of the assembled lens-system as it is in the experiment. This figure from Baranowski (2005).

### The Four Lens Objective for Imaging

The four lens objective is also used for fluorescence and axial absorption imaging: in this role, it is important to know what the resolution of the lens system is. The simulations performed by Baranowski (2005) suggest that the performance of the lens system should be diffraction-limited (for an aperture of 23.5 mm, this corresponds to a resolution of approximately 1.6  $\mu\text{m}$  for light at 780 nm): his experimental tests measured a resolution of approximately 2.5  $\mu\text{m}$ .

Once the four-lens objective was in place in the experiment and correctly aligned, further measurements could be taken to make an estimate of the resolution more directly applicable to our experimental purposes. We placed a glass slide including an Air Force R70 resolution target (as defined by MIL-STD-150A, 1959) into the experiment at a position close to the center of the magnetic trap. With a low-power ( $< 1 \text{ mW}$ ) beam illuminating the slide via the four-lens objec-

tive, we adjusted the axial position of the slide to minimize observed spot size and thus located the focal plane of the four-lens objective.

We then used the acousto-optical deflector to split the dipole trapping beam gradually into two. Figure 6.10 illustrates the spots observed through the four-lens objective at a variety of different frequencies. The frequencies have been converted to distances by a two-stage process: we used an image of the resolution target to calibrate the size of a pixel on the camera, then took note of the beam position in pixels against frequency to calibrate the deflection (in pixels) for a given change of RF frequency to the AOD. From the figure, we can see that the two spots are just distinguishable below  $3.1 \mu\text{m}$ , and clearly distinguishable at  $3.8 \mu\text{m}$ . This is consistent with the diffraction-limited simulated spot size of  $1.6 \mu\text{m}$ .

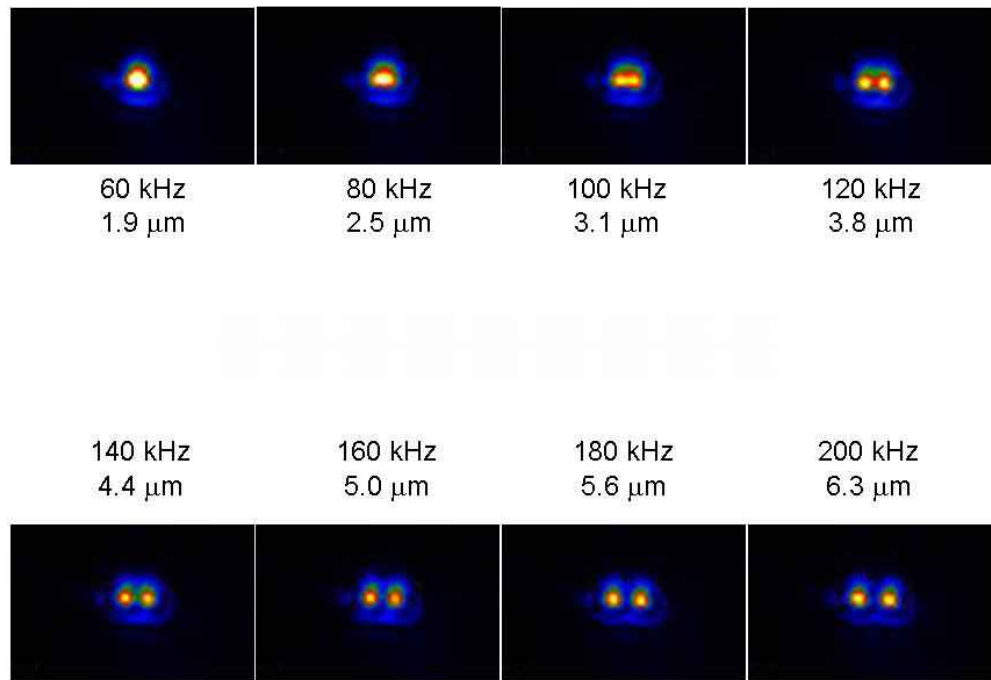


Figure 6.10: This figure shows the results of an in-situ measurement of the resolution of the four lens objective. Note that two laser spots are clearly resolved at a center-center separation of  $3.8 \mu\text{m}$  and just resolved at  $3.1 \mu\text{m}$ . This suggests an upper limit for spot-size of  $1.9 \mu\text{m}$ . Note that the frequencies listed are the deflection of each spot from the center, so the center to center distance is related to twice the given frequency. The separations given are according to a calibration with experimental error of 4%.

## CHAPTER 7

---

# Experimental Results

In this chapter I will lay out the first results achieved with the apparatus described in the preceding chapters. These experiments are not yet complete: obviously each could be improved with a larger dataset. Rather, these are intended as an indication of the potential of the apparatus and of some of the issues which my colleagues will be exploring in the coming months.

## 7.1 Calibrating the Lattice Spacing

Before any further experiments can be performed, it is necessary to determine the relationship between the frequency of the RF input to the AOD and the spacing of the resulting lattice. This section describes the theoretical relationship we expect from geometrical optics and the experiments we carried out in order to find the true calibration.

### 7.1.1 Theoretical calibration

The lattice spacing is determined by the separation of the interfering beams when they reach the four-lens objective, and thus by the optics laid out in figure 6.2. Consider a beam with frequency offset  $\delta\nu$  from the frequency corresponding to the axis of the lattice optics. By differentiating equation 6.1 we see that the angular deflection  $\delta\Theta$  of the beam will be:

$$\delta\Theta = \frac{\delta\nu\lambda}{v_s \cos(0.5\Theta_{OA})}$$

where  $\Theta_{OA}$  is the angle by which the optical axis of the lattice system is deflected from the zeroth order beam. The first lens is placed its own focal length ( $f_1 = 75$  cm) after the AOD: after passing through this lens, the beam will be travelling parallel to the optical axis at a linear offset of  $x = f_1 \tan(\delta\Theta)$  from the optical axis. It will then pass through the lattice optics, being split into four beams each offset by the same amount  $x$  in different directions.

The following two lenses have focal lengths of  $f_2 = 10$  and  $f_3 = 17$  cm respectively and thus magnify the displacement of the beams from the optical axis by a factor of  $M = f_3/f_2 = 1.7$ : the linear offset thus becomes  $x' = Mf_1 \tan(\delta\Theta)$ , where  $Mf_1 = 127.5$  cm. Two further 75 cm lenses act as a unity-magnification telescope, so when the beams reach the 4-lens objective they are each travelling parallel to the optical axis and offset by  $x'$  from it.

The four-lens objective focuses incoming parallel light at its focal length, and is positioned so that its focal plane falls on the magnetic trap. When a lattice is formed by the intersection of two beams we find from geometry that the lattice spacing  $d$  is given by

$$d = \frac{\lambda}{2 \sin \alpha} \tag{7.1}$$

where  $\lambda$  is the wavelength of the dipole trapping light and  $\alpha$  is the acute angle

between each of the beams and the optical axis. From geometry we see that a beam offset by a distance  $x'$  from the optical axis on entering a lens of focal length  $f$  will cross the optical axis in the focal plane of the lens at an angle  $\alpha = \tan^{-1}(x'/f)$ . Putting this all together, we expect the fringe spacing to vary with the frequency offset  $d\nu$  according to:

$$d = \frac{\lambda}{2 \sin \left( \tan^{-1} \left( \frac{Mf_1}{f_4} \tan(\delta\Theta) \right) \right)} \quad (7.2)$$

where  $f_4$  is the focal length of the four-lens objective, measured to be 4.05(3) cm. For a 1 MHz change in frequency,  $\delta\Theta = 10^{-3}$  radians and  $Mf_1/f_4 = 35$  so we can make the small angle approximation to eliminate all of the trigonometric functions in equation 7.2. We then obtain the approximate relation:

$$d = \frac{10.5}{\delta\nu}$$

where  $d$  is in microns and  $\delta\nu$  is in MHz.

### 7.1.2 Diffraction from a static lattice

One of the simplest situations in wave optics is a plane wave incident on a grating or series of gaps; each gap in the grating serves as a source of wavelets propagating in a semicircle forward from the gap (this is known as diffraction). Intensity maxima are observed where the distance from one gap to the plane of observation differs from distance from the next gap in either direction by an integer number of wavelengths. This results in intensity maxima which run parallel to the gaps in the grating.

Ultracold atoms can be treated using wave optics because the extremely low temperatures and momenta mean that the de Broglie wavelength of the atoms

is large in comparison to the scale of the atom. In a Bose-Einstein condensate these effects are even more clear because all of the atoms in the condensate share a common wavelength. When a sinusoidal trapping potential such as an optical lattice is applied it separates the condensate into a number of independent sources of matter waves. Just as in the simple case described above, this leads to intensity maxima parallel to the gaps between the wave sources (in this case, parallel to the fringes of the optical lattice.)

The fringes produced by this diffraction are a commonly-used method for calibrating the spacing of an optical lattice. Huckans (2006) We chose to pursue this method first because we could not observe the lattice spacing directly in our initial attempts at axial imaging.

For these experiments we loaded the lattice from a weakened trap, with  $\omega_z = 2\pi \times 4.2$  and  $\omega_r = 2\pi \times 14$  radians per second. Whilst weakening the radial trap from the high values used for evaporative cooling the vertical position of the magnetic trap was maintained by ramping up a constant field from the MOT quad coils in the Helmholtz configuration. This method was not used in the experiments discussed later in this chapter because it produces a sloshing motion with magnitude of approximately  $\pm 6$  microns radially and axial slosh on the order of  $\pm 20$  microns.

There are two regimes of interest for diffraction from optical lattices. In the first regime the atoms are loaded into the ground state of the lattice. This can be accomplished if the lattice is ramped on adiabatically with respect to the energy separation between lattice energy levels: Dahan *et al.* (1996) shows that the adiabaticity criteria for an optical lattice with potential depth less than the recoil energy  $E_R = \frac{\hbar^2 k^2}{2m}$  (where  $k = \frac{2\pi}{d}$  and  $d$  is the lattice spacing) is given by

$$\left| \frac{d}{dt} \frac{U_0}{E_R} \right| \ll \frac{32\sqrt{2}E_R}{\hbar} \quad (7.3)$$

where  $U_0$  is the lattice depth.

Experimentally, one typically wants to span the range from  $U_0 \approx 0$  to  $U_0 \approx 100E_R$ ; for a 5 micron lattice equation 7.3 shows this can be done linearly in approximately 4 ms. A non-linear ramp can be more rapid as the adiabatic rate increases with increasing  $U_0$ .

The second regime of interest is where the lattice is on for very short times. In the simplest case(the Raman-Nath regime) we neglect the kinetic energy term in the BEC's Hamiltonian during its interaction with the lattice. This approximation is valid so long as there is no change in density of the cloud on the scale of the lattice periodicity. In practice this means that the interaction time of the lattice with the atoms must be much less than the oscillation period of the harmonic oscillator potential at each lattice site and thus implies linear growth of momentum with interaction time. Beyond the Raman-Nath regime in short times of flight more complicated simulation is needed.

We choose to explore the short interaction time regime first. For these experiments, we exposed the BEC to a 1D lattice with horizontal equipotentials. Initially we saw clouds extended in the radial direction but not clearly resolvable as diffraction: by increasing the time of flight to 30 ms, we obtained the data shown in figure 7.1.

The diffraction of Bose-Einstein condensates in the short interaction time regime is discussed theoretically (without making the Raman-Nath approximation) in Janicke and Wilkens (1994), and explored experimentally in Huckans (2006). For deep optical lattices ( $U_0 > 10E_r$ ), the behavior can be treated satisfactorily in an entirely classical fashion. We imagine that initially the atoms are spread uniformly over a region of many lattice spacings. When the lattice is suddenly turned on, the atoms accelerate towards the center of the lattice site. Clearly the maximum kinetic energy which can be gained in this way is equal to the lattice depth  $U_0$ : thus

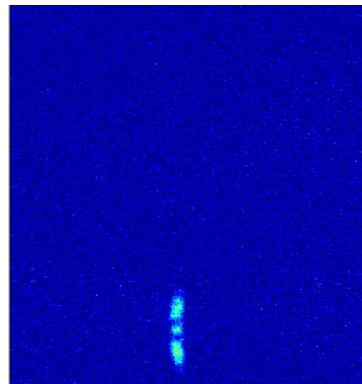


Figure 7.1: This figure shows the first evidence of diffraction from the lattice observed with our experiment. For this shot, the lattice spacing was approximately  $2.6 \mu\text{m}$  and the lattice depth was approximately 200 lattice recoils. The cloud was exposed to the lattice for approximately  $80 \mu\text{s}$  before simultaneous release from the magnetic and dipole potentials. The cloud was allowed to expand ballistically for 30 ms before this image was taken. The beam was detuned away from resonance by approximately  $0.5\Gamma$  to reduce absorption and highlight regions of high optical density. This image represents a region of approximately 4 mm on a side.

we expect the momentum of the atoms to be bounded by the value corresponding to a kinetic energy equal to  $U_0$ .

Extending this model slightly further, we can see that for very short time scales the atoms will not gain all of the energy available from the sudden imposition of the potential. Thus for short times the spread of the momentum distribution will increase with time before finally saturating.

Now consider the situation at saturation: all the atoms which had been at the edges of the potential have been accelerated to the center of the potential well and now have their maximum momentum (thus the Raman-Nath approximation is no longer valid). If we let the system evolve further with the lattice potential applied, this momentum will take the atoms away from the potential minimum and they will begin to decelerate. After a rephasing time  $t_r$  approximately equal to half the oscillation period of the lattice site trapping potential the atoms should again be in their initial state: evenly distributed across the lattice site with zero velocity. In time-of-flight this will appear as a ‘rephasing’, or a collapse of the

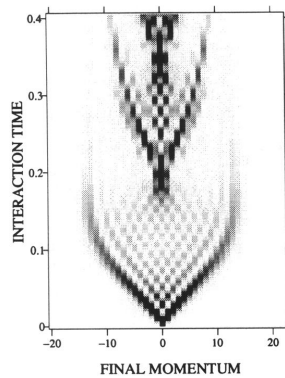


Figure 7.2: This figure illustrates the evolution of final momentum with the interaction time between a BEC and a standing-wave light field. The axes are plotted in normalized units, with momentum plotted in units of the recoil momentum of a photon in the light field and interaction time plotted in terms of the inverse of the angular frequency corresponding to the recoil energy. This figure is taken with permission from Janicke and Wilkens (1994).

spatial distribution back to the center of the distribution. Janicke and Wilkens (1994) use an exact diagonalization of the Hamiltonian coupled with numerical simulations to produce the predicted behavior illustrated in figure 7.2

In our experiment, we began by evaporating to obtain a BEC of  $2 \times 10^5$  atoms at a phase-space density of 5. In order to focus on the highest density portions of the cloud, we detuned 5 MHz from the probing resonance. We then took a series of shots in which we used a fast switch to suddenly turn on the lattice potential in the vertical direction. We left the lattice on for times varying from 10-250  $\mu$ s. The distribution of the atoms in time of flight is similar to a ‘top hat’, so the  $1/e^2$  width of the distribution was measured to determine  $z_{max}$  and thus the maximum momentum of the atoms.

We did this for three different AOD deflections: 3.5 MHz, 4 MHz and 4.5 MHz from the optical axis. Figure 7.3 illustrates the data taken for 4.5 MHz from the optical axis. Note both the expansion and collapse predicted by the model discussed above. From the classical model, we expect the maximum spatial extent of the cloud  $z_{max}$  to correspond to the momentum  $k_{max}$  which comes from a kinetic

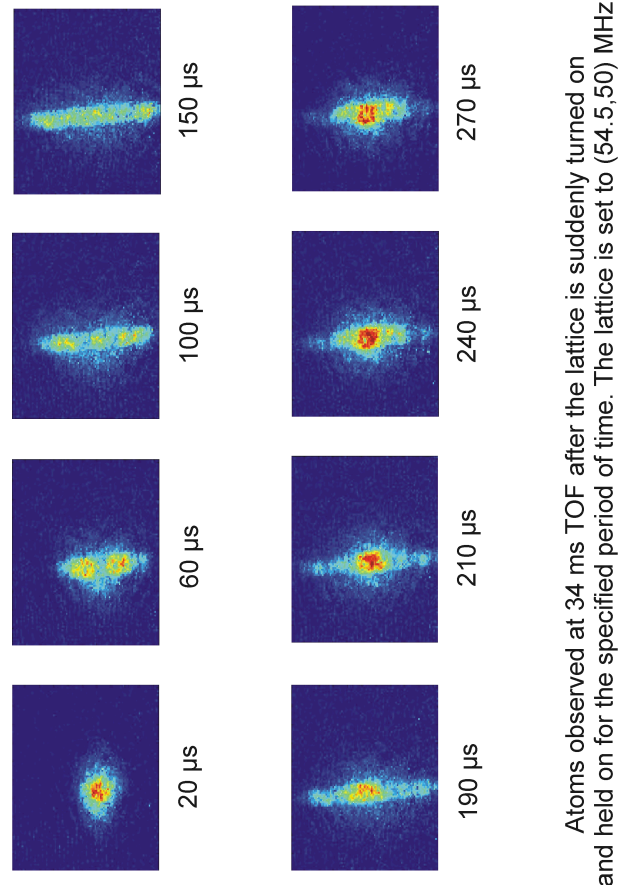


Figure 7.3: This figure shows absorption images taken after 34 ms of ballistic expansion which are a proxy for the momentum distribution of the cloud. The evolution with time is in reasonable agreement with the predictions shown in 7.2 - i.e. an initial approximately linear growth with time, followed by saturation at a fixed width and then collapse to zero momentum. The lattice depth  $U_0$  can be deduced from the maximum spatial extent of the cloud and this can be combined with the observed rephasing time to give an estimate of the lattice spacing. From these data we calculate a lattice spacing of  $2.6(2)$   $\mu\text{m}$ , which does not agree with the value of  $2.0$   $\mu\text{m}$  calculated in section 7.1.1. See text. Each image is a square of 800 microns on each side in the focal plane.

energy equal to the lattice depth  $U_0$ . Thus:

$$\begin{aligned}\hbar k_{max} &= mv_{max} \\ &= m \frac{x_{max}}{t_{tof}} \\ U_0 &= \frac{(\hbar k_{max})^2}{2m} \\ &= m \frac{x_{max}^2}{2t_{tof}^2}\end{aligned}$$

We expect the rephasing time  $t_r$  to be equal to half an oscillation period for the lattice site's trapping frequency  $\omega_L$ :

$$\begin{aligned}t_r &= \frac{\pi}{\omega_L} \\ \omega_L &= \frac{\pi}{d} \left( \frac{2U_0}{m} \right)^{0.5} \\ d &= t_r \left( \frac{2U_0}{m} \right)^{0.5}\end{aligned}$$

We performed these measurements and calculations for three different lattice spacings: the results for each are illustrated in table 7.1. We see that the experimentally calculated lattice spacings are increasing with frequency change rather than decreasing as we expect! We also note that there are measurement errors on the order of 10%: these arise in equal parts from the difficulty of determining the rephasing time given non-perfect rephasing and from the measurement errors in finding  $z_{max}$ . In order to check this unexpected result with smaller measurement errors, we decided to move on to improve axial absorption imaging of the lattice.

### 7.1.3 Imaging Atoms in the Lattice

We turned our attention back to optimizing axial absorption imaging of the lattice. We were able to improve the quality of the images we obtained by reducing the

---

Frequency change from axis (MHz)	Predicted lattice spacing (microns)	$x_{max}$ (microns)	$t_r$ ( $\mu$ s)	Calculated lattice spacing (microns)
3.5	2.57	$344 \pm 16$	$200 \pm 10$	$2.02 \pm 0.14$
4	2.25	$336 \pm 16$	$220 \pm 20$	$2.17 \pm 0.22$
4.5	2	$424 \pm 16$	$170 \pm 10$	$2.62 \pm 0.18$

Table 7.1: Results taken from using the simple classical model discussed in the text to fit to our data of the time-evolution of the momentum distribution with lattice interaction time. The error in  $x_{max}$  is assuming a measurement error of one pixel either way on the full width of the distribution. The error in the determination of the rephasing time  $t_r$  is due to the subjectivity of determining the rephasing time given that there is always some occupation of higher momentum states.

intensity of the probing beam and re-optimizing the detuning of the axial absorption probe beam. After taking these steps, we were able to obtain the image shown in figure 7.4 for a lattice corresponding to a 0.3 MHz deflection from the optical axis. We were unable to get clear images for lattices with smaller spacings using the optical setup as it then was.

With the resolution we have measured for the 4-lens objective, it ought to be possible to measure lattice spacings on the order of microns, rather than the spacings of roughly 25 microns we have measured here. We took several steps to try to improve the imaging: the first was to change the way we ramped our magnetic trap down. Previously we had ramped the currents through the baseball and bias coils to obtain a weak trap: this caused the axial trapping to change and induced a sloshing motion for the trapped atoms. We changed the sequence to ramp down only the bias coil, which should reduce the radial trapping frequency without changing the axial confinement or the radial field gradient.

While studying the magnetic trap ramps, we also discovered that it takes approximately 500 ms after the control voltage for the magnetic trap currents have been ramped down to reach a stable current in the magnetic trap. We adjusted our ramp-down sequence to ensure that we were not attempting to load the lattice until this settling was completed.

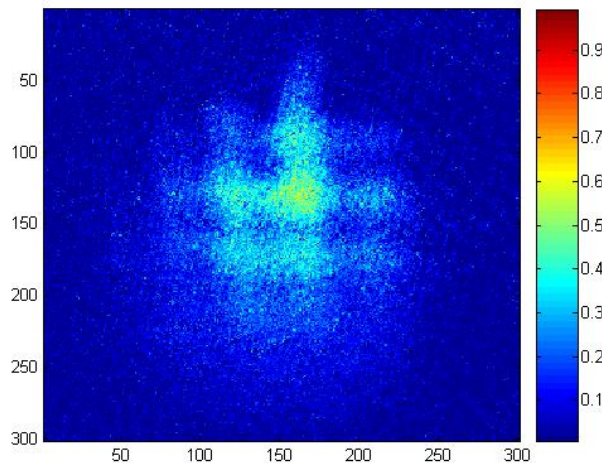


Figure 7.4: An image of atoms trapped in the optical lattice taken by absorption imaging along the axial direction. The signal input to the AOD to generate this lattice is offset by 0.3 MHz from the optical axis of the lattice system. The axes are labelled in pixels: as each pixel is 16  $\mu\text{m}$  on a side and the magnification is found to be 24.7 the image shown is approximately 200  $\mu\text{m}$  square.

We also abandoned the attempt to maintain the vertical position of the trap during the ramp-down by ramping up the MOT quads with opposite currents: while this supported trap did succeed in maintaining the vertical position of the trap, it offset the trap by approximately 100 microns in the axial direction and induced a sloshing motion. Returning to an unsupported trap resulted in the location of the weak trap moving down by a few mm: we realigned the axial absorption beam and the four-lens objective to ensure that they were aligned on to the new trap position.

Having made these changes, we obtained images like the one shown in part a) of figure 7.5: this shot was taken with a frequency deflection of 0.7 MHz from the optical axis, which according to the calibration in section 7.1.1 gives a lattice spacing of 12.9 microns.

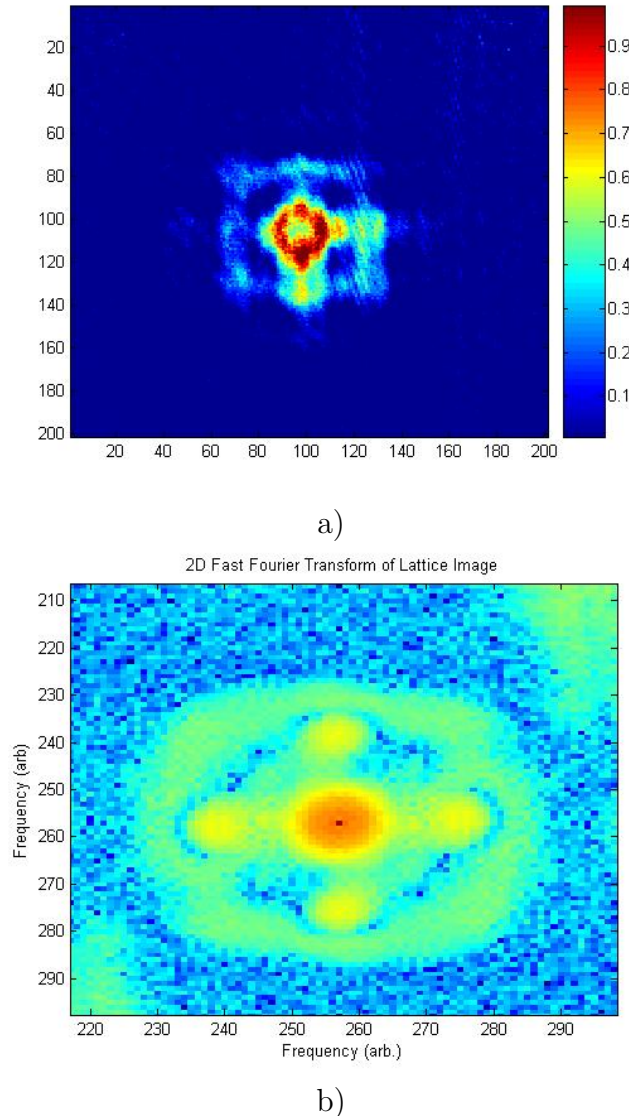


Figure 7.5: a) An image of lattice-trapped atoms in axial absorption. In this shot the AOD signal was offset by 0.7 MHz from the optical axis. The axes are labelled in pixels: as each pixel is  $16 \mu\text{m}$  on a side and the magnification is found to be 24.7 the image shown is approximately  $130 \mu\text{m}$  square. b) shows the frequency-space intensity distribution obtained by a two-dimensional fast Fourier transform of the data: this gives a lattice spacing of  $17.7(6)$  microns.

### 7.1.4 Calibrating the Lattice Spacing

With clearer pictures of lattice-trapped atoms available, the next task was to measure the spacing of the lattice seen in the image and compare it to our theoretical expectations. We determine the lattice spacing by using MATLAB's 'fft2' routine to perform a two-dimensional fast Fourier transform of the image to convert it into frequency space: this is the preferred method of analysis because it is unaffected by the orientation of the lattice fringes in the focal plane. The frequency space image obtained from an FFT is shown in part b) of figure 7.5, giving a lattice spacing of 17.7(6) microns.

As a cross-check the data was integrated along each of the axes separately and fitted with multiple Gaussian peaks. The lattice spacing estimated from the average distance between the peaks of the fitted Gaussians was 16.7(6) microns, which is consistent with the measurement from the Fourier transform to within the experimental error on the measurements. The Gaussian fits are illustrated in figure 7.6.

Repeating this process with a series of further shots at different lattice spacings gives the results shown in figure 7.7. The most significant point to note from these data is that the vertical and horizontal lattices have distinctly different spacings: additionally, neither the vertical or horizontal spacings we observed are consistent with the theoretical prediction from section 7.1.1.

### 7.1.5 Measuring Beam Separation before the 4-lens Objective

We see from figure 7.7 that the lattice spacings we obtain from direct imaging of the lattice are not consistent with our prediction from section 7.1.1. One possible explanation of this is that the optics which shape the beam separation are slightly

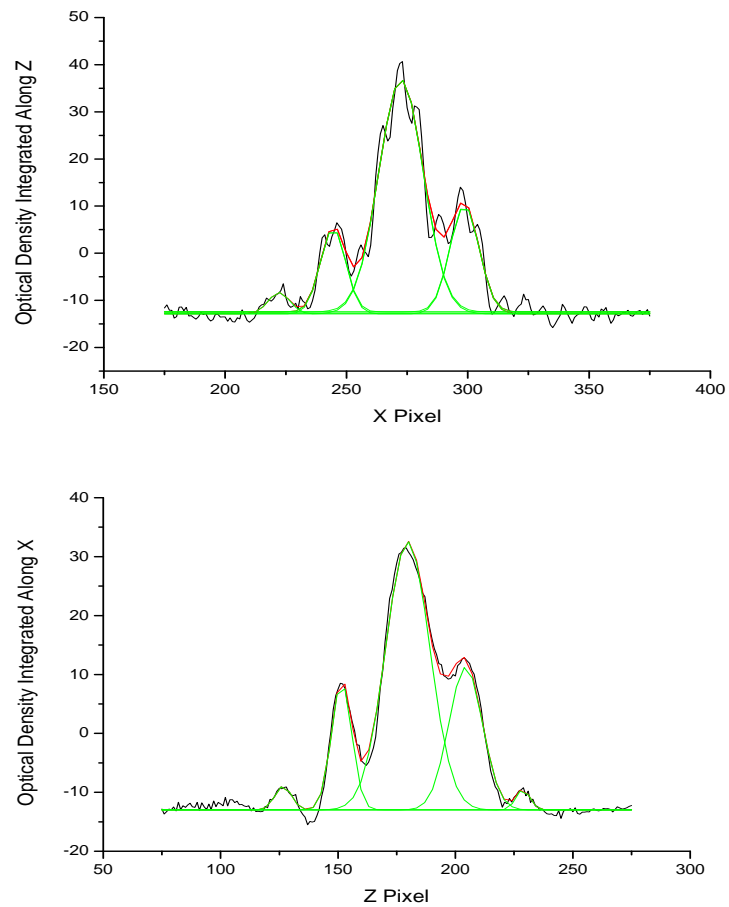


Figure 7.6: For this figure the data illustrated in part a of figure 7.5 was integrated along the x and z axes to give the lower and upper traces respectively; fitting multiple Gaussian peaks to the resulting profile gives a lattice spacing of 16.7(6) microns.

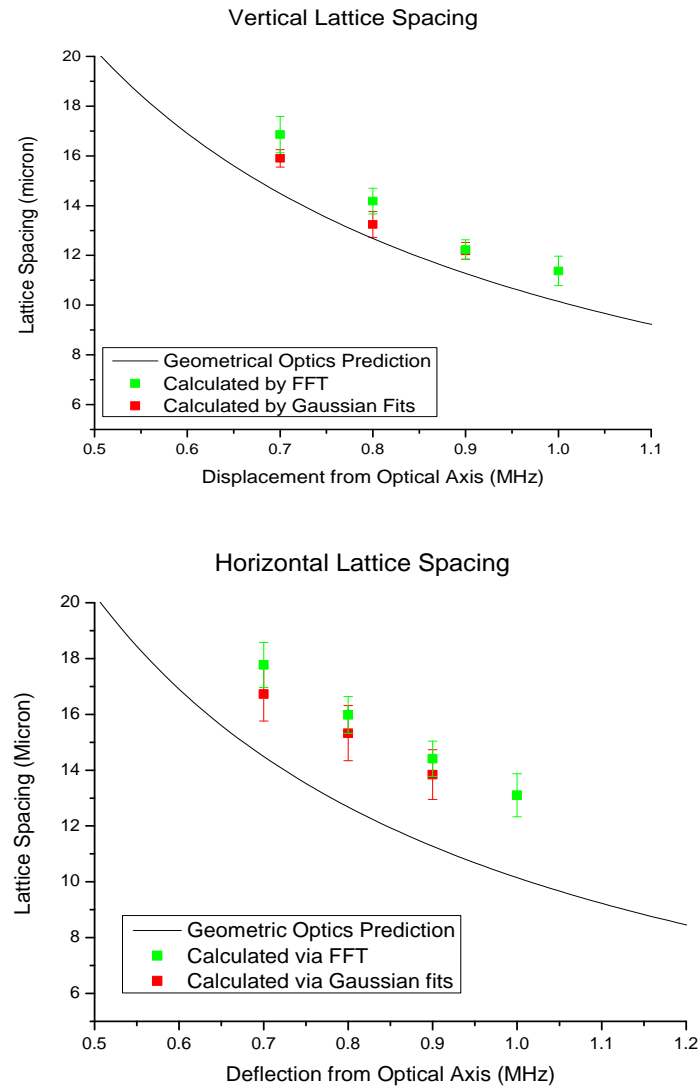


Figure 7.7: This figure shows the experimentally measured lattice spacings for both the FFT method and for fitted Gaussians as a function of the frequency difference applied to the AOD, as discussed in the text. Note that the vertical and horizontal spacings are significantly different, and that neither is consistent with the geometrical optics prediction.

misaligned or misplaced: to test this hypothesis, we need to measure the separation of the beams before they pass through the four-lens objective and compare this to our prediction.

This was done by placing a high-quality mirror just before the 4-lens objective to divert the lattice beams on to a CCD: one of these images thus obtained is shown as part a) of figure 7.8. By fitting Gaussian profiles to this image I found the separation between the beams and thus calculated the expected lattice spacing: this is illustrated in part b) of figure 7.8.

From part a) of figure 7.8 we see that the measured separation of the beams is less than we would have expected from the calculation in section 7.1.1. This suggests that at least one of the telescopes between the AOD and the 4-lens objective is slightly displaced from its ideal position.

We also note that the beam separations are different horizontally and vertically, and also that the variation of separation with frequency depends on whether the initial offset from the optical axis is made in the x-direction or the y-direction. This could result from a slight misalignment of one of the lenses or from the axial displacement of the two acousto-optical deflectors resulting in the telescope setup not being at the same distance for both.

From part b) of figure 7.8, we see that the lattice size expected for the measured beam separations is consistent with the lattice spacings measured by FFT to within the experimental error.

By using a linear fit to part a) of figure 7.8 in combination with the focal length of the four-lens objective we obtain a new calibration of frequency offset to lattice spacing, given approximately as:

$$d = \frac{11.5}{\delta f}$$

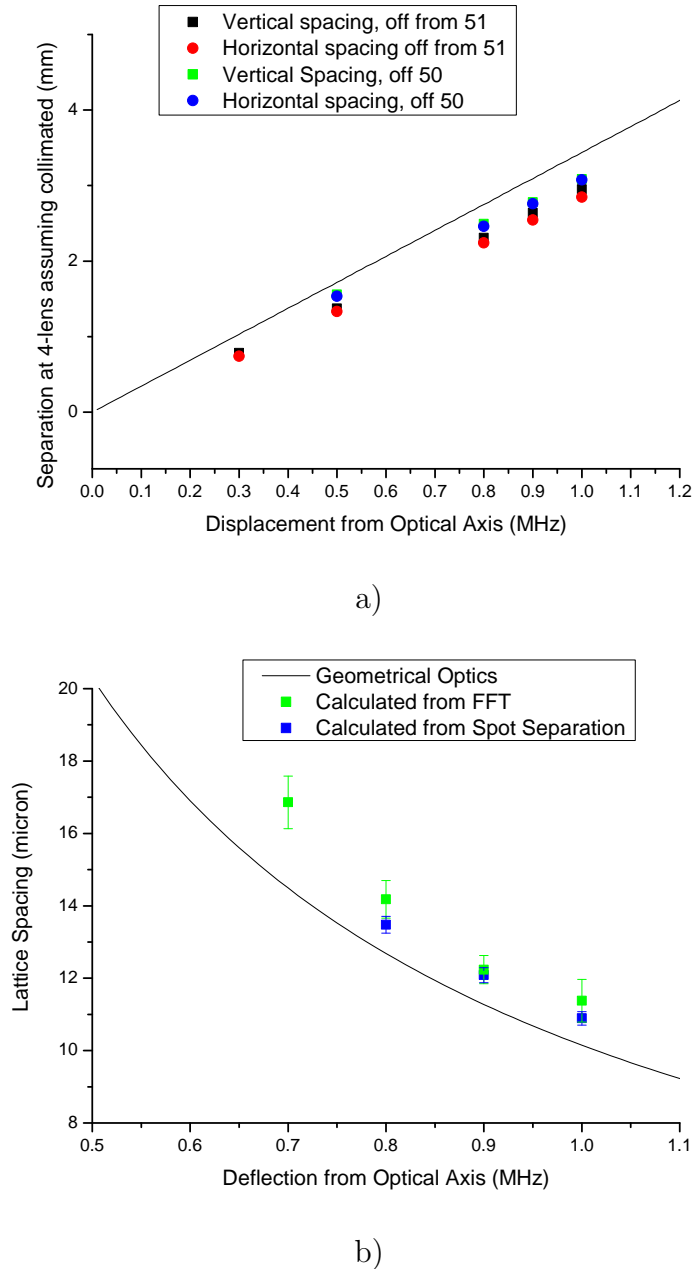


Figure 7.8: a) illustrates the beam separations observed vertically and horizontally immediately before the four lens objective and compares these to the values expected from the ideal system discussed in section 7.1.1. Part b compares the lattice spacing against frequency relations measured via fast Fourier transform, the geometrical optics prediction of section 7.1.1 and data calculated from the measured beam separation before the 4-lens objective.

where  $d$  is in microns and  $\delta f$  is in MHz.

After I left the lab the lattice optics were realigned: this eliminated the difference between the horizontal and the vertical lattice spacings.

## 7.2 Implementing Rotation

Consider the position of the beam in the plane perpendicular to the optical axis as the beam enters the lattice optics as being specified in plane polar coordinates. In the experiments reported thus far we have considered only the periodicity of the lattice formed; this is controlled by the magnitude of the offset of the incoming beam from the optical axis of the lattice optics ( $r$  in plane polar coordinates) and so can be varied by adjusting the deflection frequency applied to the beam by the AOD. While all the experiments reported thus far were carried out with a lattice aligned so that the fringes ran vertically and horizontally, it is also possible to rotate the lattice relative to the vertical by altering the direction of the offset of the incoming beam from the optical axis ( $\phi$ ). This rotation is illustrated in figure 7.9.

The optical lattice setup is arranged such that a deflection of the beam in either the  $x$  or  $y$  directions alone produces a lattice with  $\phi = 0, \frac{\pi}{2}$  (where the difference between  $\phi = 0$  and  $\phi = \frac{\pi}{2}$  is that the polarization of the vertical and horizontal fringes swaps over); other rotations can be achieved by deflecting the incoming beam simultaneously in both the  $x$  and  $y$  directions. Having established the flexibility of our lattice period, we began our initial investigation of the effects of rotating the lattice on the atoms held in the lattice.

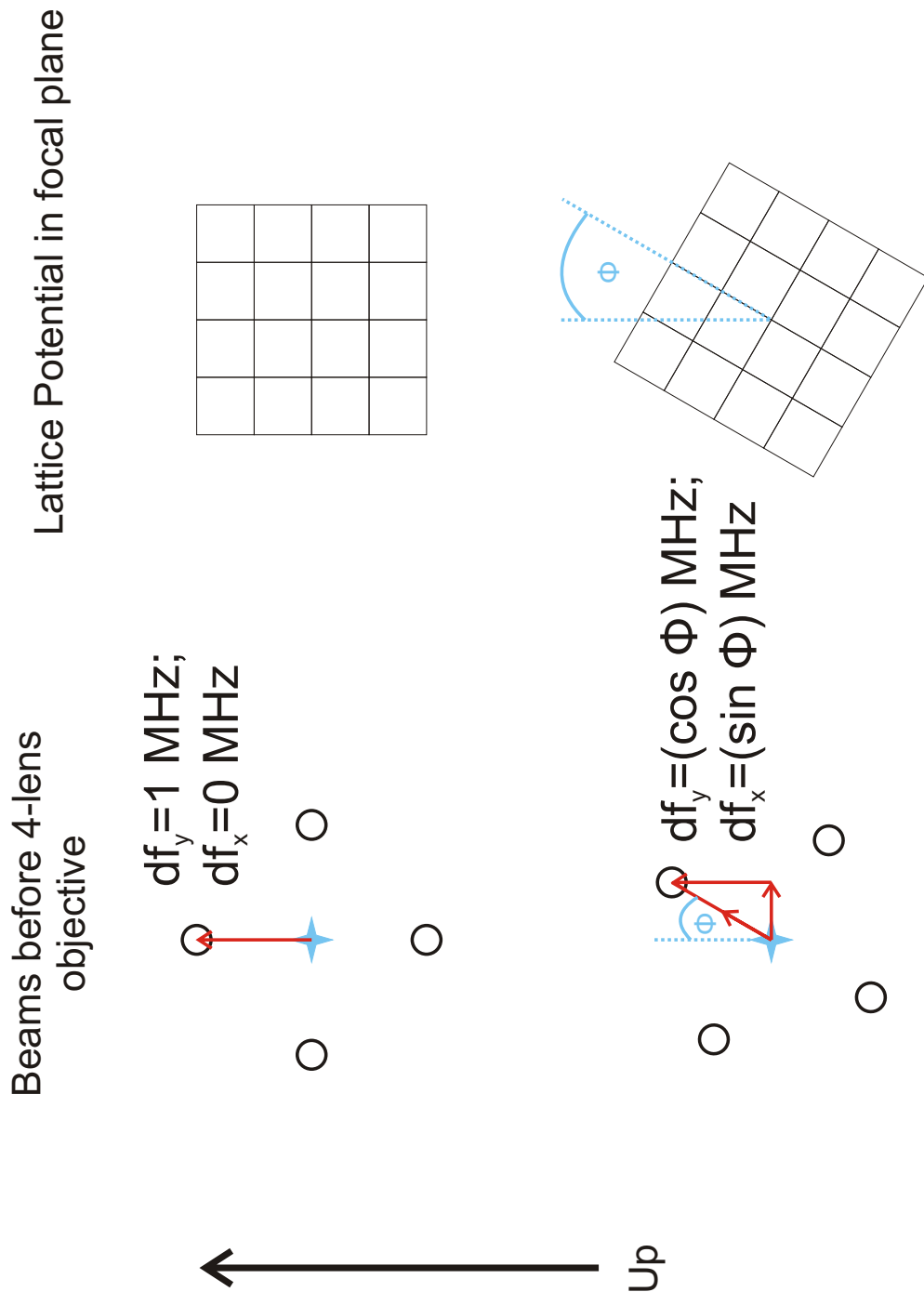


Figure 7.9: The deflection of the initial beam by the AOD determines the angle of rotation of the lattice potential. The left hand side of this figure shows the beams as they would enter the four lens objective while the right hand side shows the lattice potential obtained in the focal plane of the lens. In the top half of this figure we see a beam deflected from the optical axis by 1 MHz in the  $y$ -direction and undeflected in the  $x$ -direction: this forms a lattice with fringes running horizontally and vertically. The lower half of the figure shows a beam which is deflected by  $\sin \phi$  MHz in the  $x$  direction and  $\cos \phi$  MHz in the  $y$  direction: this produces a lattice rotated by  $\phi$  relative to the vertical.

### 7.2.1 Lattices at arbitrary angles

The first step is to make sure that atoms are held in the lattice at whatever angle it is inclined, so as to be sure that they will be held in the potential during rotation. We imaged atoms held in the lattice for angles at  $15^\circ$  intervals from  $0^\circ$  to  $360^\circ$ . Some of the images thus obtained are shown in figure 7.10.

### 7.2.2 Change in aspect ratio with rotation

Having determined that the atoms were held in the lattice for arbitrary angles, we decided to investigate the effect of exposing a cold cloud to a rotating lattice. The procedure we followed was to evaporate to BEC, then to ramp to the weak magnetic trap and allow it to settle. We then ramped on the lattice over 100 ms with the RF signal stable at 2 MHz deflection from the axis in the  $x$ -direction: the lattice is ramped to a final power of approximately 0.6 mW per beam. A TTL trigger was then sent to the DDS system which started both the  $x$  and  $y$  frequencies oscillating sinusoidally so as to result in the lattice rotating around the optical axis. We imaged the cloud after 21 ms time of flight. Figure 7.11 compares an unperturbed BEC to a cloud exposed to a static lattice and to a cloud which has been exposed to a rotating lattice for approximately 125 ms. The lattice is generated with a 2 MHz offset from the optical axis, giving an estimated lattice periodicity of 5.8 microns. The cloud sizes are measured by integrating the images shown in figure 7.11 along the X (axial) and Y (radial) directions separately and fitting a Gaussian to the integrated profile: all sizes quoted are the  $e^{-2}$  half-widths of the Gaussian.

Looking at axial size, we see a steady increase from the BEC (95(2) microns) to the static lattice (98(1) microns) to the cloud exposed to the rotating lattice (102(1) microns). This expansion is consistent with heating due to intensity variation in the lattice beams during rotation.

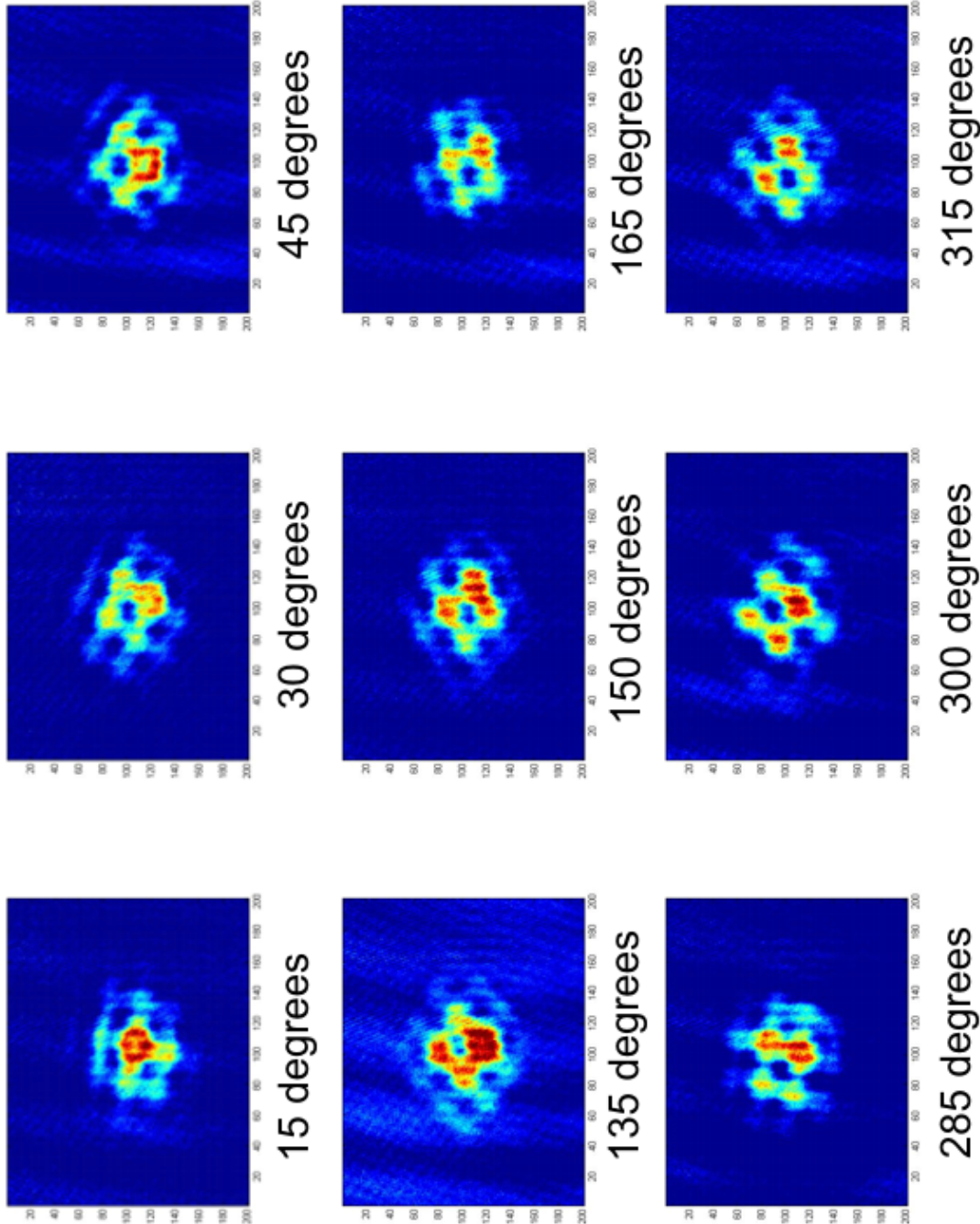


Figure 7.10: This figure illustrates atoms held in an optical lattice inclined at a variety of angles in order to illustrate that trapping in the lattice is maintained throughout rotation. These shots were taken with a total frequency offset of 0.7 MHz from the optical axis; the color scale is the same as used in figure 7.5. The axes are labelled in pixels: as each pixel is  $16 \mu\text{m}$  on a side and the magnification is found to be 24.7 the image shown is approximately  $130 \mu\text{m}$  square.

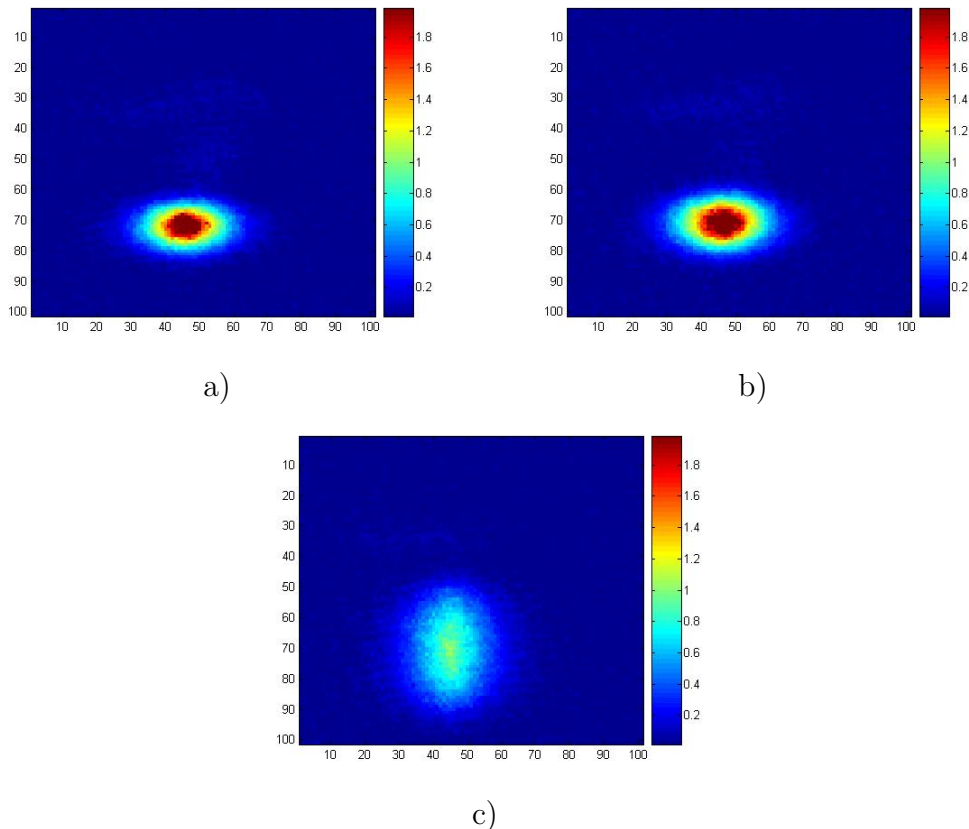


Figure 7.11: Conventional absorption images which illustrate the difference between; (a) a BEC, (b) a cloud exposed to a static optical lattice for 125 ms and (c) a cloud which has been exposed to a rotating lattice for 125 ms. In all three cases the cloud was allowed to expand for 21 ms before the image was taken. The lattice was at 2 MHz deflection from the optical axis (approximately 5 micron lattice spacing) and was rotated at 10 Hz in part c. The numbers on the axes indicate pixels on the CCD: as each pixel is 16 microns square and the magnification for these shots was approximately 2 , each image is 800 microns square.

Now consider radial size. The BEC has a radial size of 54.7(5) microns after 21 ms TOF; when exposed to the static lattice the radial size increases to 63.0(5) microns. This is consistent with a BEC expanding from a harmonic trap made up of a superposition of the magnetic trap and the Gaussian envelope of the lattice beams. After being exposed to the rotating lattice, the cloud expands to 146(2) microns.

Intuitively, one would imagine the sort of expansion we observe in figure 7.11 to be caused by the weakening of the trap potential as it supplies the centripetal force for the rotation. If this is the case, it should vary with rotation frequency. To investigate this, we fixed the rotation time at 125 ms and varied the rotation frequency. The data thus acquired is illustrated in figure 7.12. We see from figure 7.12 that there is a sharp increase in the radial size with the onset of rotation: the axial size is essentially stable, though there is a suggestion of a sinusoidal variation with frequency for low frequencies which we intend to investigate further.

We have tried to model the behavior illustrated in figure 7.12, so far without success. Our initial idea of centripetal force weakening the trapping potential would actually produce the opposite result in time-of-flight: the weaker trap that results from the centripetal acceleration leads to a larger initial size for the cloud but reduces the rate of expansion by reducing the peak density.

We also modelled the cloud as a composite of several clouds, each of which continues moving tangentially to the circular motion when the trap is released. However, we found that the velocity generated by the rotation was not sufficient to generate the radial expansion we have seen: the BEC has a radial size of order 10 microns, which even at a rotation frequency of 10 Hz would only lead to an expansion of about 20 microns rather than the 80 microns we have observed. My coworkers are continuing to investigate this behavior.

Both of the models discussed above are illustrated in figure 7.13.

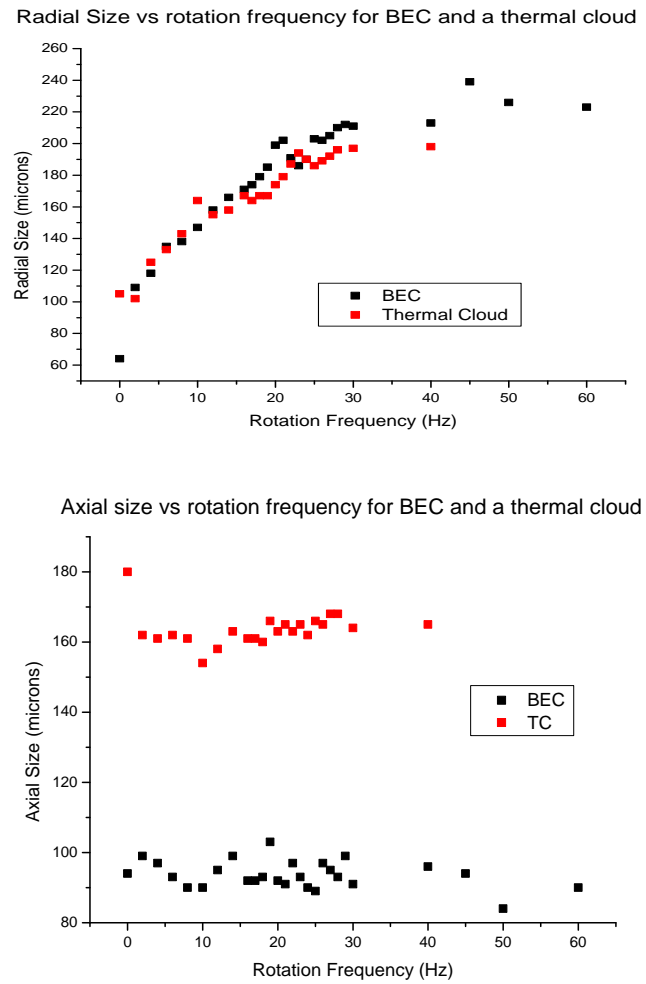


Figure 7.12: These graphs show how the radial and axial sizes of a BEC and a thermal cloud vary with the frequency at which the lattice is rotated. For these data, the lattice was ramped on over 100 ms while stationary; the lattice was then rotated for approximately 125 ms before being turned off simultaneously with the magnetic trap.

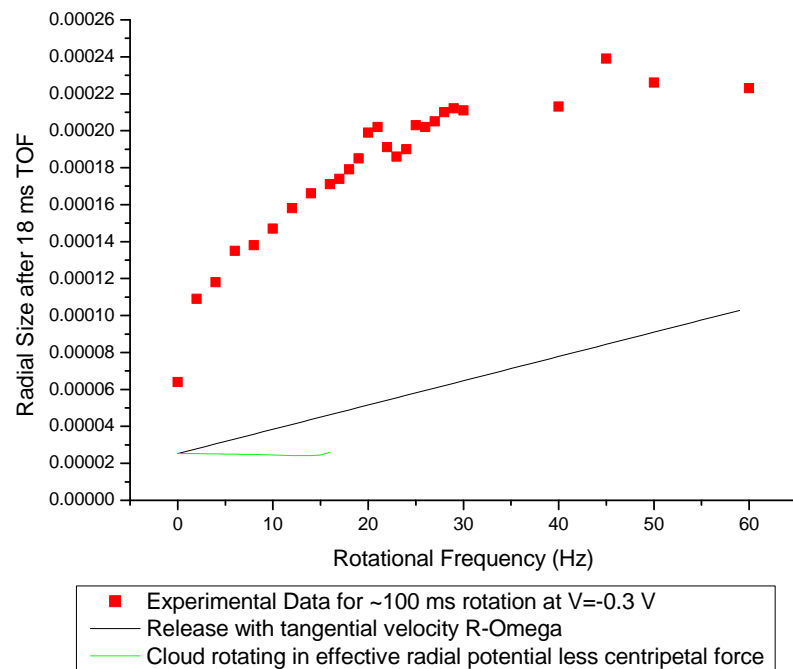


Figure 7.13: Simple theoretical models fail to describe the change in radial size of the cloud when exposed to a rotating lattice. The scatter plot gives the measured radial size when the lattice is ramped up and then rotated for 125 ms at the frequency indicated. The black line shows the expansion which would be expected for a classical model in which atoms continue to move at their tangential velocity when the lattice is released. The green line below it shows the behavior expected for expansion from a trap whose radial frequency is reduced by the centripetal acceleration.

### 7.2.3 Calculating the Heating Rate due to Rotation

Previous experiments involving rotating lattices have encountered significant problems with heating: in the work reported by Tung *et al.* (2006), for example, the depth of the rotating lattice had to be very much smaller than the chemical potential ( $U_0 \leq 0.1\mu$ ) to avoid heating the atoms out of the BEC regime. As the heating in that experiment was primarily due to mechanical instability we expect our acousto-optical system to be less susceptible to heating, but this needs to be verified experimentally. In this section we describe our efforts to measure the heating rate and to compare that measured heating rate to a prediction from theory.

As a worst-case scenario for heating we consider rotating the lattice without applying the amplitude normalization discussed in section 6.2.4. We assume that in this case the fluctuations in intensity due to rotation ( $\approx \pm 8\%$ ) will be the dominant source of heating in the rotating lattice.

In order to measure the heating experimentally we evaporated to BEC, ramped to the weak trap and then applied the lattice with a spacing of approximately 5 microns over 100 ms. We rotated the atoms at a frequency of 10 Hz for times varying between 0 and 800 ms. We used the axial size of the cloud as a proxy for the temperature of the cloud as it should be isolated from any other effects of rotation: these temperature measurements are plotted against time in figure 7.14. From an exponential fit to these data we find that the temperature of the cloud will increase by a factor of  $e$  in a time constant of  $(359 \pm 83)$  ms.

To model this situation theoretically, we use the results developed by Savard *et al.* (1997): they considered a simple harmonic oscillator approximation to the trapping potential and used time-dependent perturbation theory to model the effect of a periodic modulation in trapping frequency such as would be generated by an intensity fluctuation. In their paper, they developed the result that the average

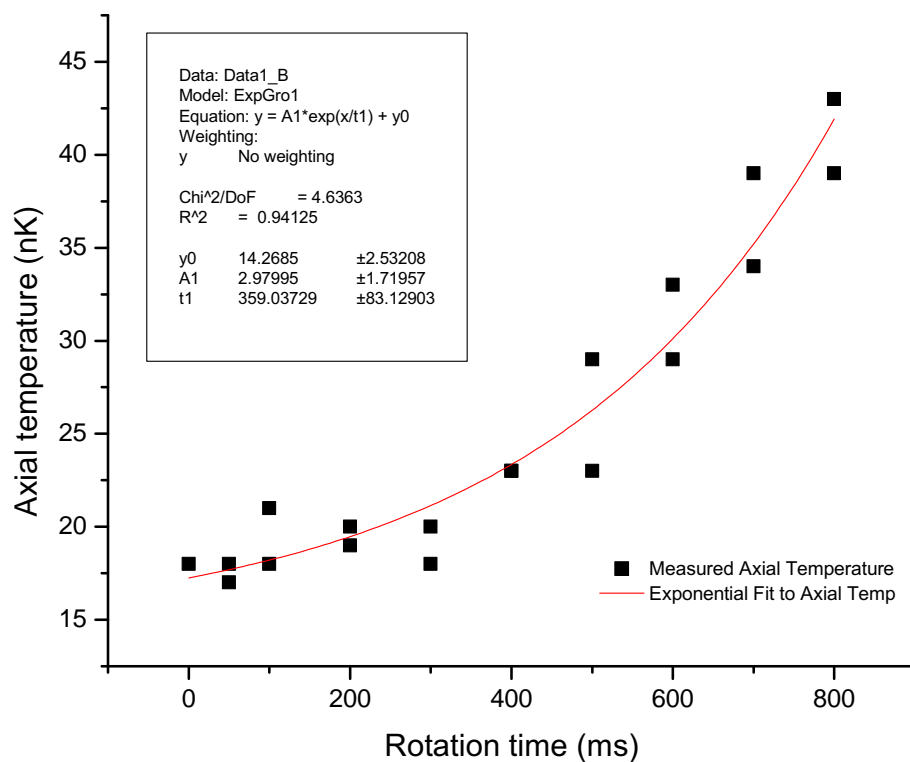


Figure 7.14: Axial temperature plotted against the length of the exposure to the rotating lattice. A first-order exponential fit to the data is also shown, giving a time constant of  $(359 \pm 83)$  ms for the temperature of the cloud to increase by a factor of  $e$ .

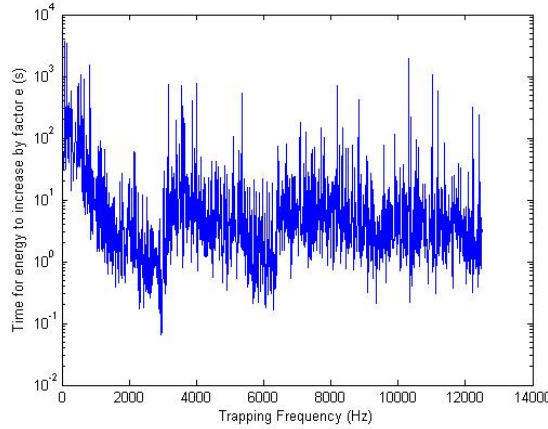


Figure 7.15: A theoretical prediction of the time taken for the average energy of the atoms to increase by a factor of  $e$  derived from the noise spectrum of the rotation is plotted on a logarithmic axis against the harmonic trapping frequency of an individual lattice site.

energy of the atoms  $\langle \dot{E} \rangle$  will increase exponentially with a time constant  $T_I$  given by:

$$T_I = \frac{1}{2\pi^2 \nu_{tr}^2 S_\epsilon(2\nu_{tr})} \quad (7.4)$$

where  $\nu_{tr} = \omega_{tr}/(2\pi)$  is the oscillation frequency of the harmonic potential and  $S_\epsilon(2\nu_{tr})$  is the one-sided power spectrum of the fractional intensity noise  $(I(t) - \bar{I})/\bar{I}$  at the first harmonic of the trapping frequency. In an asymmetrical trap, the average time constant  $T_I$  can be found by averaging the time constant for each trapping frequency provided that the atoms are in thermal equilibrium.

The power spectrum was determined from a discrete Fourier transform of the intensity variation data given in section 6.2.4 and used to calculate the energy folding time  $T_I$  for a range of trapping frequencies. These data are shown in figure 7.15: for our typical experimental conditions trap frequencies are on the order of  $2\pi \times 500$  Hz in the plane of the lattice and  $2\pi \times 5$  Hz axially, so these data suggest that the folding time due to rotation should be on the order of 10 seconds. This is much higher than the figure derived experimentally in figure 7.14.

The data used to derive figure 7.15 was limited in sampling rate by the memory available on the oscilloscope. After I left the lab, my coworkers repeated the experiment with higher sampling rate. The noise spectrum obtained from that data is consistent with the experimentally measured folding time of  $(359 \pm 83)$  ms.

In order to explore experimentally the theoretical ideas on cold-atom analogues to the fractional quantum Hall effect, we need to rotate the atoms at approximately the radial trapping frequency (17.2 Hz): it is not yet clear how many rotations will be necessary to access the regime of interest. Thus this heating rate is experimentally promising as it allows time to adiabatically ramp on the lattice (see section 7.1.2) followed by several complete rotations at a rotation rate approaching the trapping frequency.

## CHAPTER 8

---

# Conclusions

As discussed in chapter 1, rotating and accordion lattices have significant potential for exploring exciting new physics in systems of ultracold atoms. In this chapter I shall briefly summarize the progress described in the preceding chapters towards this goal, then compare the approach we've implemented to similar efforts being undertaken by other research groups. Finally, I shall briefly outline the next steps forward for improving the system.

## 8.1 Progress So Far

Harsono (2006) described the achievement of Bose-Einstein condensation in our apparatus, our first observations of dipole trapping and the observation of atoms trapped in a 2 by 2 array of dipole microtraps. Since then progress has been - if not as swift as I had hoped - at least steady. Minor improvements have included improved reproducibility by reducing the timing uncertainty in our experimental sequence, installation of a laminar flow air system and enclosure for the Titanium-Sapphire laser and a slightly improved alignment for the MOT table.

We also changed the direction of the experiment: from intending to produce an array of individual dipole microtraps to producing a more traditional optical lattice potential. We took a significant step towards this goal with the implementation of a direct digital synthesis based system for highly controllable and dynamic generation of radio frequency signals. With the aid of the software described in section 5.5, we achieve signals with spur suppression greater than 50 dB which can be ramped in amplitude or frequency at update rates up to 1.5 MHz. This update rate could be further extended by upgrading the digital IO card used to send data to the DDS chips.

Our next step was to implement absorption imaging along the axis of the magnetic trap and the lattice beams. This allows us to image atoms held in the lattice and - because it provides a reference for an optical path passing through the BEC - has reduced the time required to align the dipole trapping beam has been reduced from weeks to days.

Using the DDS system and the lattice optics described in chapter 6, we have implemented and trapped atoms in an accordion lattice. We have imaged these lattice trapped atoms resolvably at lattice periodicities from 30 to 10 microns: we have used these images to calibrate the variation of lattice spacing with frequency deflection. The relatively large lower limit for resolvable lattice sites is surprising: it may be a consequence of the lack of a quantization axis in the axial absorption direction. We observe lattice trapping but cannot resolve individual lattice sites for lattice spacings down to approximately 3 microns, though at such large beam separations we begin to lose power to clipping on the edges of the lattice optics.

Finally, we have demonstrated that we can rotate the lattice potential through a full circle without losing confinement and then shown a frequency dependent expansion of the condensate in the radial direction with rotation. We do not yet fully understand the mechanism behind this expansion, but it is promising that

we can retain atoms in the lattice for even relatively long rotation periods and without extreme heating (at least in the axial direction).

## 8.2 Comparison to Other Work

Few experiments seem to have combined the idea of a rotating lattice with that of an accordion lattice in the way that we have: thus I will review comparable work in the fields of accordion lattices and rotating lattices separately. As discussed in section 1.1.2, experimental work involving accordion lattices has been recently reported by Huckans (2006) and Li *et al.* (2008): I'll briefly describe the methods used in each case to illustrate other possibilities.

Huckans implemented a 1D accordion lattice using a galvanometer for angular deflection followed by a beam splitter and symmetric lenses to focus the split beams on to the BEC. This scheme is illustrated in figure 8.1. Using the mechanical motion of a galvanometer in this fashion introduces some noise due to dither, though with a sufficiently expensive galvanometer this can be reduced to below the level of noise introduced by the signal generator driving the galvanometer position. This scheme could be extended to create a two-dimensional accordion lattice, though it would require a substantial amount of space on the optical bench: given the separate lenses used, however, rotation could only be implemented by physically rotating the breadboard containing the accordion lattice optics.

Li *et al.* (2008) have implemented a system very similar to the first stage of ours, illustrated in figure 8.2. Although it has not yet been applied to cold atoms, they demonstrate a continuous change in lattice periodicity from 0.96 microns to 11.2 microns with the center fringe moving by less than 3 microns. Extending this scheme for rotation would result in a scheme almost identical to ours.

The most recent experimental work on rotating lattices was reported by Tung

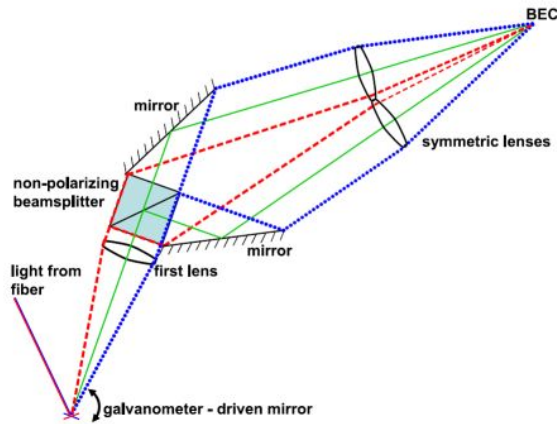


Figure 8.1: This figure illustrates the accordion lattice scheme used by Huckans (2006). The galvanometer scans the beam across the surface of a non-polarizing beam-splitter which sends half of the beam to each of the symmetric lens and mirror setups. Both lenses are arranged so that their focal point lies on the point where the BEC is located; as the galvanometer scans the angle between the intersecting beams will change but their point of intersection should not. This produces a smooth expansion of the accordion lattice. This figure reproduced with permission from Huckans (2006)

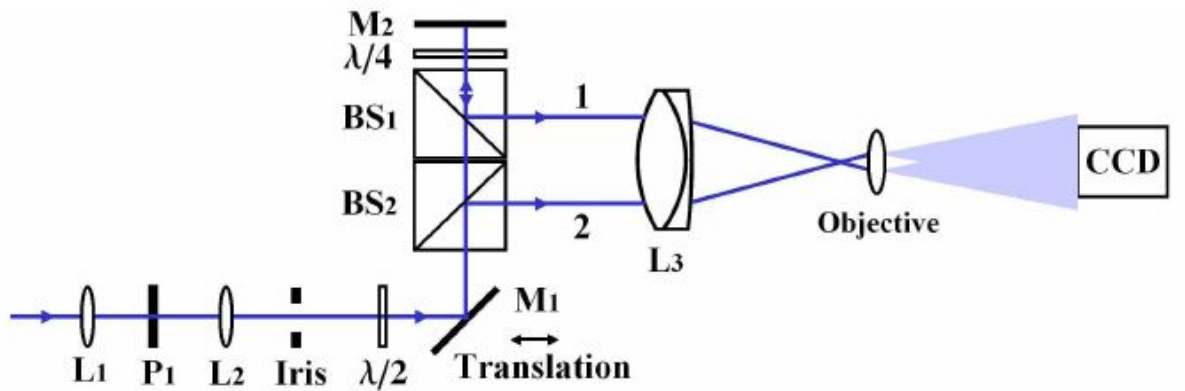


Figure 8.2: This figure illustrates the accordion lattice scheme used by Li *et al.* (2008): the indicated mirror translates across the beam-splitting cube, half of the light is reflected by the first cube while the other half passes through the second cube, is rotated through 90 degrees by two passes through the quarter-wave plate and then is reflected on its return trip through the second lattice. Figure used with permission from Li *et al.* (2008)

*et al.* (2006): they generate a rotating lattice by putting a mechanically rotating mask in the way of a laser beam. The light passing through the mask is then focussed on to the BEC to generate a lattice, which rotates with the mask; the mask is set rotating before the start of the experiment so the optical lattice is never stationary. In this arrangement they report pinning of a vortex lattice on to the potential minima of the optical lattice. A significant advantage of our apparatus is the ability smoothly to ‘spin up’ the lattice from rest during the experiment.

### 8.3 Future Steps

The experiments presented in this thesis are not by any means complete: since I departed the lab to write up the work so far, my coworkers have continued to improve the apparatus. This section briefly outlines the plans for the immediate future of the experiment.

A key property of rotating superfluids is that they are irrotational until a critical velocity is reached, then a vortex is nucleated and circulation begins. The first significant experiment to perform with the apparatus is to apply a rotating lattice to the BEC, allow the BEC to equilibrate with the additional angular momentum and then release it from the magnetic trap. By imaging the falling cloud along the axis of rotation at varying times of flight we hope to be able to observe vortices in the BEC. Given the trap frequencies in our trap, we would expect a vortex to be visible after approximately 15 ms time of flight.

Experimentally, there are two obvious improvements which can be made. The first is provide axial confinement via an optical lattice potential: with a sufficiently confining potential, this would allow the experiment to reach the quasi-2D regime which is important for exploring condensed matter effects like the fractional quantum Hall effect. With that accomplished, the next experimental improvement will

be to use a second acousto-optical deflector to ensure that the orthogonal lattices are completely incoherent: this will incidentally make the optical setup considerably simpler as it will eliminate the requirement for a variety of periscopes!

# Bibliography

- M. Albiez, R. Gati, J. Fölling, S. Hunsmann, M. Cristiani, and M. K. Oberthaler. Direct observation of tunneling and nonlinear self-trapping in a single bosonic Josephson junction. *Physical Review Letters*, 95:010402, 2005.
- W. Alt. An objective lens for efficient fluorescence detection of single atoms. *OPTIK*, 113:142, 2002. URL <http://www.citebase.org/abstract?id=oai:arXiv.org:physics/0108058>.
- Analog Devices. Datasheet: AD9852 CMOS 300 MSPS Complete DDS. Technical report, Analog Devices, 2004. Rev. C.
- M. H. Anderson, J. R. Ensher, M. R. Matthews, C. E. Wieman, and E. A. Cornell. Observation of Bose-Einstein condensation in a dilute atomic vapor. *Science*, 269(5221):198–201, 1995.
- M. R. Andrews, C. G. Townsend, H. J. Miesner, D. S. Durfee, D. M. Kurn, and W. Ketterle. Observation of interference between two Bose condensates. *Science*, 275(5300):637–41, 1997.
- J. J. Arlt, O. Maragó, S. Webster, S. Hopkins, and C. J. Foot. A pyramidal magneto-optical trap as a source of slow atoms. *Optics Communications*, 157: 303–309, 1998.
- P. Baranowski. Towards number correlated states of a Bose Einstein condensed gas. Master’s thesis, University of Oxford and Frei Universität Berlin, March 2005.
- T. Bergeman, G. Erez, and H. J. Metcalf. Magnetostatic trapping fields for neutral atoms. *Phys. Rev. A*, 35(4):1535–1546, Feb 1987. doi: 10.1103/PhysRevA.35.1535.
- J. Billy, V. Josse, Z. Zuo, A. Bernard, B. Hambrecht, P. Lugan, D. Clément, L. Sanchez-Palencia, P. Bouyer, and A. Aspect. Direct observation of Anderson localization of matter waves in a controlled disorder. *Nature*, 453:891, 2008.
- I. Bloch. Ultracold quantum gases in optical lattices. *Nature Physics*, 1:23, 2005.
- V. Boyer, R. M. Godun, G. Smirne, D. Cassettari, C. M. Chandrashekhar, A. B. Deb, Z. J. Laczik, and C. J. Foot. Dynamic manipulation of Bose-Einstein condensates with a spatial light modulator. *Physical Review A*, 73:031402, 2006.

- C. C. Bradley, C. A. Sackett, J. J. Tollett, and R. G. Hulet. Evidence of Bose-Einstein condensation in an atomic gas with attractive interactions. *Physical Review Letters*, 75(9), 1995.
- Y. Castin and R. Dum. Bose-Einstein condensates in time dependent traps. *Physical Review Letters*, 77(27):5315, 1997.
- C.-S. Chu, F. Schreck, T. P. Meyrath, J. L. Hanssen, G. N. Price, and M. G. Raizen. Direct observation of sub-Poissonian number statistics in a degenerate Bose gas. *Physical Review Letters*, 95, 2005.
- D. Clément, A. F. Varón, M. Hugbart, J. A. Retter, P. Bouyer, L. Sanchez-Palencia, D. M. Gangardt, G. V. Shlyapnikov, and A. Aspect. Suppression of transport of an interacting elongated Bose-Einstein condensate in a random potential. *Physical Review Letters*, 95, 2005.
- A. Corney. *Atomic and Laser Spectroscopy*. Oxford University Press, Oxford, 1977.
- Crystal Technology. Datasheet: AOM 3080-125. Technical report, Crystal Technology, Inc., 2002.
- M. B. Dahan, E. Peik, J. Reichel, Y. Castin, and C. Salomon. Bloch oscillations of atoms in an optical potential. *Physical Review Letters*, 76:4508, 1996.
- K. B. Davis, M.-O. Mewes, M. R. Andrews, N. J. van Druten, D. S. Durfee, D. M. Kurn, and W. Ketterle. Bose-Einstein condensation in a gas of Sodium atoms. *Physical Review Letters*, 75(22), 1995.
- D. P. DiVincenzo. Quantum computation. *Science*, 270(5234):255–261, 1995.
- R. Dumke, M. Volk, T. Müther, F. B. J. Buchkremer, G. Birkl, and W. Ertmer. Micro-optical realization of arrays of selectively addressable dipole traps: a scalable configuration for quantum computation with atomic qubits. *Physical Review Letters*, 89(9):097903, 2002.
- R. P. Feynman. Simulating physics with computers. *International Journal of Theoretical Physics*, 21(6/7):467, 1982.
- C. J. Foot. *Atomic Physics*. Oxford Masters' Series in Physics. Oxford University Press, 2005.
- D. G. Fried, T. C. Killian, L. Willmann, D. Landhuis, S. C. Moss, D. Kleppner, and T. J. Greystak. Bose-Einstein condensation of atomic hydrogen. *Physical Review Letters*, 81(18), 1998.
- L.J. Geerligs, M. Peters, L.E.M. de Groot, A. Verbruggen, and J.E. Mooij. Charging effects and quantum coherence in regular Josephson junction arrays. *Physical Review Letters*, 63(3), 1989.

- K. Gentile and R. Cushing. A technical tutorial on Direct Digital Synthesis. Technical report, Analog Devices, 1999.
- M. Glazer and J. Wark. *Statistical Mechanics: A Survival Guide*. Oxford University Press, 2001.
- B. Goldberg. *Digital Frequency Synthesis Demystified*. Demystifying Technology. Butterworth-Heinemann Ltd., 2000.
- E. I. Gordon. A review of acousto-optical deflection and modulation devices. *Proceedings of the IEEE*, 54(10), 1966.
- M. Greiner, O. Mandel, T. Esslinger, T. W Hansch, and I. Bloch. Quantum phase transition from a superfluid to a Mott insulator in a gas of ultracold atoms. *Nature*, 415(6867):39–44, 2002.
- R. Grimm, M. Weidmüller, and Y. Ovchinnikov. Optical dipole traps for neutral atoms. *Adv. At. Mol. Opt. Phys.*, 42:95–165, 2000.
- L.K. Grover. A fast quantum mechanical algorithm for database search. In *Proceedings, 28th Annual ACM Symposium on the Theory of Computing*, page 212, May 1996. URL <http://arxiv.org/abs/quant-ph/9605043>.
- Z. Hadzibabic, P. Krüger, M. Cheneau, B. Battelier, and J. Dalibard. Berezinskii-Kosterlitz-Thouless crossover in a trapped atomic gas. *Nature*, 441:1118, 2006.
- A. Harsono. *Dipole trapping and manipulation of ultra-cold atoms*. PhD thesis, University of Oxford, 2006.
- W. R. Hindmarsh. *Atomic Spectra*. Pergamon Press, Oxford, 1967.
- P. Horowitz and W. Hill. *The Art of Electronics*. Cambridge University Press, 1989.
- J. H. Huckans. *Optical Lattices and Quantum Degenerate  $^{87}\text{Rb}$  in Reduced Dimensions*. PhD thesis, University of Maryland, College Park, 2006.
- D. Jaksch. Optical lattices, ultracold atoms and quantum information processing. *Contemporary Physics*, 45(5):367–381, 2004.
- D. Jaksch, C. Bruder, J. I. Cirac, C. W. Gardiner, and P. Zoller. Cold bosonic atoms in optical lattices. *Physical Review Letters*, 81(15):3108–3111, 1998.
- U. Janicke and M. Wilkens. Atomic motion in a magneto-optical field. *Physical Review A*, 50(4):3265, 1994.
- F. A. Jenkins and H. E. White. *Fundamentals of Physical Optics*. McGraw-Hill, New York, 1937.

- W. Ketterle, D. Durfee, and D. Stamper-Kurn. Making, probing and understanding Bose-Einstein condensates. In M. Inguscio, S. Stringari, and C.E. Wieman, editors, *Bose-Einstein condensation in atomic gases*, Amsterdam, 1999. International School of Physics "Enrico Fermi", Course CXL, IOS Press.
- A. Korpel. Acousto-optics: A review of fundamentals. *Proceedings of the IEEE*, 69(1), 1981.
- A. Korpel, R. Adler, P. Desmares, and W. Watson. A television display using acoustic deflection and modulation of coherent light. *Applied Optics*, 5(10): 1667–1675, 1966.
- T. C. Li, H. Kelkar, D. Medellin, and M. G. Raizen. Real-time control of the periodicity of a standing wave: an optical accordion. *Optics Express*, 16(8): 5465, 2008.
- R. Loudon. *The Quantum Theory of Light*. Oxford University Press, 1983.
- L. N. Magdich and V. Ya. Molchanov. *Acoustooptic devices and their applications*. Gordon and Breach Science Publishers, 1989. Translated from Russian by D. Parsons.
- H. J. Metcalf and P. van der Straten. *Laser Cooling and Trapping*. Graduate Texts in Contemporary Physics. Springer, New York, 2002.
- MIL-STD-150A. Military standard, photographic lenses. Technical report, Department of Defence, Washington, D.C., 1959. Standard is available from: <http://www.ntis.gov/> - most optical catalogues will include a resolution target made to this specification.
- G. Modugno, G. Ferrari, G. Roati, R. J. Brecha, A. Simoni, and M. Inguscio. Bose-Einstein condensation of potassium atoms by sympathetic cooling. *Science*, 294: 1320, 2001.
- D. L. Moehring, P. Maunz, S. Olmschenk, K. C. Younge, D. N. Matsukevich, L.-M. Duan, and C. Monroe. Entanglement of single-atom quantum bits at a distance. *Nature*, 449:68, 2007.
- O. Morsch and M. Oberthaler. Dynamics of Bose-Einstein condensates in optical lattices. *Reviews of Modern Physics*, 79:178, 2006.
- H. Nyquist. Certain topics in telegraph transmission theory. *Transactions of the AIEE*, 47:617–644, 1928. Reprinted as a classic paper in Proc. IEEE Vol. 90 No. 2 (2002).
- R. N. Palmer, A. Klein, and D. Jaksch. Optical lattice quantum Hall effect. *Physical Review A*, 78:013609, 2008.

- S. Peil, J. V. Porto, B. Laburthe-Tolra, J. M. Obrecht, B. E. King, M. Subbotin, S. L. Rolston, and W. D. Phillips. Patterned loading of a Bose-Einstein condensate into an optical lattice. *Physical Review A*, 67(5):051603, 2003.
- C. J. Pethick and H. Smith. *Bose-Einstein condensation in dilute gases*. Cambridge University Press, 2002.
- C. A. Regal, M. Greiner, and D. S. Jin. Observation of resonance condensation of fermionic atom pairs. *Physical Review Letters*, 92(4):040403, 2004.
- G. Reinaudi, T. Lahaye, Z. Wang, and D. Guery-Odelin. Strong saturation absorption imaging of dense clouds of ultracold atoms. *ArXiv e-prints*, 707, July 2007.
- G. Roati, C. D'Errico, L. Fallani, M. Fattori, C. Fort, M. Zaccanti, G. Modugno, M. Modugno, and M. Inguscio. Anderson localization of a non-interacting Bose-Einstein condensate. *Nature*, 453:895, 2008.
- T. A. Savard, K. M. O'Hara, and J. E. Thomas. Laser-noise-induced heating in far-off resonance optical traps. *Physical Review A*, 56(2):R1095, 1997.
- R. Scheunemann, F. S. Cataliotti, Theodor W Hansch, and M. Weitz. Resolving and addressing atoms in individual sites of a CO<sub>2</sub>-laser optical lattice. *Physical Review A*, 62(5):051801, 2000.
- D. Schrader, I. Dotsenko, M. Khudaverdyan, Y. Miroshnychenko, A. Rauschenbeutel, and D. Meschede. Neutral atom quantum register. *Physical Review Letters*, 93(15):150501/1–4, 2004.
- M. O. Scully and M. S. Zubairy. *Quantum Optics*. Cambridge University Press, Cambridge, 1997.
- S. A. Self. Focussing of spherical Gaussian beams. *Applied Optics*, 22(5):658, 1983.
- Y. Shin, M. Saba, T. A. Pasquini, W. Ketterle, D. E. Pritchard, and A. E. Leanhardt. Atom interferometry with Bose-Einstein condensates in a double-well potential. *Physical Review Letters*, 92(5):050405, 2004.
- P. W. Shor. Polynomial-time algorithms for prime factorization and discrete logarithms on a quantum computer. In *Proceedings of the 35th Annual Symposium on Foundations of Computer Science*, page 124134. IEEE Computer Society Press, November 1994. URL <http://www.arxiv.org/abs/quant-ph/9508027>. (Arxiv.org stores a version of this paper revised in 1996).
- D. A. Steck. Rubidium 87 D line data. Technical Report LA-UR-03-8638, Los Alamos National Laboratory, October 2003. URL <http://steck.us/alkalidata/>.
- J. Tierney, C. Rader, and B. Gold. A digital frequency synthesizer. *IEEE Transactions on Audio and Electroacoustics*, 19(1):48–57, 1971.

- S. Tung, V. Schweikhard, and E. A. Cornell. Observation of vortex pinning in Bose-Einstein condensates. *Physical Review Letters*, 97:240402, 2006.
- L. M. K. Vandersypen, M. Steffen, G. Breyta, C. S. Yannoni, M. H. Sherwood, and I. L. Chuang. Experimental realization of Shor's quantum factoring algorithm using nuclear magnetic resonance. *Nature*, 414:883, 2001.
- T. Weber, J. Herbig, M. Mark, H. Nägerl, and R. Grimm. Bose-Einstein condensation of cesium. *Science*, 299(5604), 2003.
- J. Weiner, V. S. Bagnato, S. Zilio, and P. S. Julienne. Experiments and theory in cold and ultracold collisions. *Reviews of Modern Physics*, 71(1):1–85, 1999.
- R. Williams, J. D. Pillet, S. Al Assam, B. Fletcher, and C. J. Foot. Dynamic optical lattices: two-dimensional rotating and accordion lattices for ultracold atoms. *Optics Express*, 16:16977–16983, 2008.
- A. Yariv. *Introduction to Optical Electronics*. Holt, Rinehart and Winston, Inc., 1971. 1971 edition is the edition used most extensively; the section on acoustooptics is substantially unchanged in most recent (1997) edition.
- D. D. Yavuz, P.B. Kulatunga, E. Urban, T. A. Johnson, N. Proite, T. Henage, T. G. Walker, and M. Saffman. Fast ground state manipulation of neutral atoms in microscopic optical traps. *Physical Review Letters*, 96:063001, 2006.